Justus-Liebig-Universität Gießen

I. Physikalisches Institut

Control of Emission Properties of Semiconductors through Functionalization

Dissertation

**zur Erlangung des Doktorgrades
der Naturwissenschaften**

- Dr. rer. nat. -

**dem
Fachbereich 07
Mathematik und Informatik, Physik, Geographie
vorgelegt von**

Florian Dobener

aus Herborn

Gießen, im September 2019

1. Gutachter: Prof. Dr. Sangam Chatterjee
2. Gutachter: Prof. Dr. Wolfram Heimbrodt

Contents

List of Abbreviations

APB	Anti phase boundary
BAC	Band anti-crossing
BEC	Bound exciton complex
CB	Bonduction band
CCD	Charge-coupled-device
CHA	Concentric hemispherical analyzer
CL	Core level
CMOS	Complementary metal-oxid-semiconductor
cw	Continious wave
DAP	Donor-acceptor-pair
DFT	Density functional theory
DOS	Density of states
erf	Error function
ESCA	Electron spectroscopy for chemical analysis
FAT	Fixed analzyer transmission
FRR	Fixed retardation ratio
FWHM	Full-width-half-maximum
GVD	Group velocity dispersion
hh	Heavy-hole
HHG	High harmonic generation
HOMO	Highest occupied molecular orbital
IMFP	Inelastic mean free path
LCAO	Linear combination of atomic orbitals
LED	Light emitting device
lh	Light-hole
LUMO	Lowest unoccupied molecular orbital

MOVPE Metal-organic vapour-phase epitaxy

MQW Multi quantum well

MST Model solid theory

NA Numerical aperture

Nd:YLF Neodymium doped yttrium-lithium-fluorine

PCF Photonic crystal fiber

PES Photoelectron spectroscopy

PL Photoluminescence

PLE Photoluminescence excitation spectroscopy

QW Quantum well

SBE Semiconductor bloch equation

SFG Sum frequency generation

SHG Second harmonic generation

SPM Self phase modulation

TEM Transmission electron microscopy

UHV Ultra high vacuum

UPS UV photoelectron spectroscopy

UV Ultra violet

VB Valence band

VBM Valence band maximum

VCA Virtual crystal approximation

XPS X-ray photoelectron spectroscopy

XRD X-ray diffraction

1 | Introduction

Today's world is governed by information. Life revolves around the accessibility and availability of communication channels and the speed of digital information interchange has reached a prior unimaginable pace. It feels natural to us to communicate with people anywhere in the world in a fraction of seconds, with devices so small, that they fit in our pockets. Hence, wirelessness and seamlessness are the terms of modern society's communication, shaped by big technology companies. The consequence is a gradual expansion of the boundaries of technological progress and possibilities. Recent advances towards an always-reachable pool of information and data, known as the cloud, stresses again the timelessness and importance of information availability at any time in the modern world. Some influential companies even reduce the amount of ports of their devices, stating that the future is solely wireless.

However, these developments required significant technological efforts. The first landmark and technological backbone dates back to 1947 when Shockley, Bardeen and Brattain invented the world's first transistor[1]. The device was introduced with the words "[The transistor] may be employed as an amplifier, oscillator, and for other purposes for which vacuum tubes are ordinarily used"[1], which hardly captures today's importance of the transistor. Eleven years later, Jack Kilby solved the tyranny of numbers[2], which is the ever-growing demand for more wiring and components in complex electronic designs. His simple, yet ingenious idea was to combine transistors on a single piece of semiconductor, creating the first integrated circuit[3]. This device was simple and just generated a plain sine wave[4], but what followed is a success story of semiconductor technology, leading to devices of billions of transistors in handheld devices, super-computers able to simulate our physical world, globe-spanning systems of connections and thus, our modern world in all. Modern transistors consist of silicon and technological advances in silicon growth led to the availability of single crystals with a pureness of 99.9999 %[5], most likely rendering silicon the purest material on earth. It was a prospecting candidate to redefine the unit of weight due to the precise control of the material, too[6]. Current silicon based devices have a transistor size of 14 nm, only a factor 70 bigger than the atomic radius of silicon. This strong miniaturization raises the question: where is the limit? In fact, the past pace of roughly doubling the amount of transistors per area every two years, known as Moore's law, is already stagnating. Therefore, recent research point towards the control of single quantum states (e.g. single atomic levels) as a building block of quantum computers[7], which enable a completely new way of computation and bring consequences for society yet unclear. Most likely, the yet to come technology will call for further technological advances, such as the progression of semiconductor technology fueled the demand for information exchange, culminating in the publication of the hypertext protocol by Tim Berners Lee and Robert Cailiau in 1990[8]. It was the birth of the internet, which further powered the effort, money and research put into semiconductor technology. Certainly, the emerging possibility of inter-device communication called for fast communication capabilities. As light is the fastest possible way of information interchange, its use in this context seems inevitable. Indeed, semiconductor light emitters and detectors cover most of the communication devices

today, arisen from breakthrough inventions, such as the light emitting device (LED) or the laser. Semiconductor light-emitter development took place parallel to the birth of integrated circuits. Theodor Maiman first demonstrated lasing in a ruby crystal in 1960[9]. Within two years, Hall et al.[10] transferred the laser concept to semiconductors by demonstrating laser emission of GaAs heterostructures.

The history of light emission from semiconductors actually outdates electronic diodes - over 100 years ago an electroluminescence device was reported by Round[11]. In the 1920's, Oleg Vladimirovich Losev carefully characterized the electrical and optical properties of LEDs in 16 publications[12], describing it as the reversal of Einstein's photoelectrical effect. After 40 years of little research on the topic, the impact of semiconductor technology and the possibility of lasing in heterostructures took over the development of LEDs, too. Ga(As,P) structures were the first LEDs emitting in the visible part (red) of the spectrum[13], quickly followed by green (GaP, 1970)[14] and blue (GaN, 1980/90)[15] light emitting diodes. Today, except for a small region in the green spectral region, LEDs exist for emission wavelengths throughout the complete visible spectrum, making them cost and energy effective devices for many applications. Therefore, LEDs are the basis for most illumination devices, such as screens or home lightning[16], where it completely replaced the ineffective tungsten light bulb[17].

However, white-light emission from semiconductor devices remains challenging due to the inherent restriction to the band gap of the material. For lasers the situation is even worse, since they require direct-band-gap materials, thus, even less wavelengths are available. This thesis contributes to the study of materials for functionalization of semiconductors, to broaden the spectral regions of wavelengths accessible by light emitting semiconductor devices. Three main topics are covered: the engineering of novel structures for lasers directly integrated on silicon and two investigations related to the transformation of laser light in the scope of non-linear optical processes. The non-linear optical processes are investigated in the framework of second harmonic emission and broadening of the incident laser light to the emission of visible to near-infrared white-light.

The lack of efficient electrically driven lasers in direct connection with silicon transistors circumvents the realization of on-chip photonics. Silicon photonics could solve several bottlenecks in state-of-the-art computer technology. In particular information transfer between building blocks of a modern computing devices like volatile memory access or fast inter-device communication. A direct realization of bulk or quantum well silicon lasers is impossible, since the indirect band structure of the material renders the material incapable in providing an efficient laser action[18]. Albeit, mass-communication links operate on laser driven optical fiber systems[19], their connection to complementary metal-oxid-semiconductor (CMOS) structures is complex and costly. Currently, the employed lasers are (Ga,In)As on InP substrate, which are externally wired to computers for information interchange. The interlink is not only comparably slow, but the complete material system is expensive due to the high costs of In, too. Therefore, laser manufacturers and scientists are searching for a material directly grown on a CMOS structure. A promising material is Ga(N,As,P)[20]. While already the ternary Ga(As,P) allows for nearly lattice matched growth on silicion, the quaternary composition enables for pseudomorphically strained growth on silicon. Moreover, the additional degree of freedom in the composition of Ga(N,As,P) enables tuning of the emission wavelength in dependence of the composition. Common heterostructures for laser applications consist of several layers in addition to the active Ga(N,As,P) layer[21]. Lasing of such multilayer

structure has already been demonstrated at cryogenic temperatures[22]. However, room temperature lasing has not been reported to date. The first part of this thesis aims to investigate the internal band offsets between the several layers, which are crucial in device design and further optimization of Ga(N,As,P) structures. Photoluminescence excitation spectroscopy (PLE) and X-ray photoelectron spectroscopy (XPS) experiments provide the means to determine all of the materials band offsets and to contribute to a general understanding of the structure.

The second part of this work deals with conversion of laser light into other wavelengths. Frequency conversion is a powerful tool for reaching new wavelength regimes, either for scientific purposes or for consumer devices. Frequency doubling is a common mechanism in green light emitting laser pointers. In spectroscopy applications, various devices make use of frequency conversion: frequency doublers or triplers, optical parametric amplifiers and lasing systems. Materials exhibiting non-linear properties are a necessity for these applications. Potassium niobate ($KNbO_3$) is a perovskite showing a strong second order non-linearity and is thus an appropriate material for frequency doubling. Albeit the fact that it is already in use for some devices, it has so far only been characterized at the standard wavelength of 1064 nm and its performance as frequency doubler in conjunction with tunable systems is unclear. The participation of this work centers on the measurement of the absolute second order coefficient over a broad energy range.

The second part is devoted to the characterization of potassium niobate as well as the investigations of another non-linear optical material: recently synthetized amorphous material show very strong non-linear responses leading to the generation of white-light[23]. The molecular structures studied here are tin-sulfide cluster cores in an adamantine-like arrangements. Aromatic ligands are attached at the four tin sites. A prototypical system is the $[(PhSn)_4S_6]$ structure, but many different compounds exist allowing for a investigation of the role of different cluster atoms or ligands. The white-light generation process itself seems to be of a different nature than what is assumed in established white-light emitters such as photonic crystal fibers (PCFs)[24]. The optical nonlinearity is very strong, such that even continious wave (cw) laser irradiation triggers white-light emission, which is not possible for existing non-linear white-light converters. Yet, the underlying mechanisms of the process remains partly unknown. Recent investigations on the material suggests that its π-ligand system and its habitus play a major role in the generation process[25]. The second part of this work tries to progress the understanding of the structure-property relation by investigating a series of compounds, in which a coinage metal complex replaces one of the ligands and the implications of this replacement for white-light generation.

In all this thesis is structured as follows: first, the theoretical framework is discussed, namely a brief introduction to the theory of semiconductors and their interaction with light is given. It is followed by a discussion of non-linear processes and a description of the interaction of electrons with matter interaction. The following two parts describe the methods and discusses results of the hetero-offsets in Ga(N,As,P) multilayer systems and the non-linear properties on potassium niobate as well as of SnS clusters, respectively. Finally, the results are summarized and an outlook on the various topics concludes this dissertation.

2 | Light Matter Interaction

Generally, Maxwell's equations govern all the properties of macroscopic light propagation. The four formulas

$$\nabla \cdot \mathbf{D} = \rho \tag{2.1}$$

$$\nabla \cdot \mathbf{B} = 0 \tag{2.2}$$

$$\nabla \times \mathbf{E} = -\frac{\partial}{\partial t}\mathbf{B} \tag{2.3}$$

$$\nabla \times \mathbf{H} = \mathbf{j} + \frac{\partial}{\partial t}\mathbf{D} \tag{2.4}$$

with the electric displacement $\mathbf{D} = \varepsilon_0 \mathbf{E} + \mathbf{P}$ ($\mathbf{P}$ is the polarization density) and magnetic induction $\mathbf{B} = \mu_0 \mathbf{H} + \mathbf{M}$ ($\mathbf{M}$ is the magnetization density), constitute the propagation in vacuum (with $\mathbf{M} = 0$ and $\mathbf{P} = 0$) as well as in any material ($\mathbf{M} \neq 0$ and $\mathbf{P} \neq 0$). $\mathbf{E}$ and $\mathbf{H}$ denote the electric and magnetic field strength, respectively. $\mathbf{j}$ is the electrical current density. For non magnetizable materials and vanishing currents, inserting Eq. 2.4 into Eq. 2.3 yields the wave equation

$$\left(\nabla^2 - \frac{n^2}{c^2}\frac{\partial^2}{\partial t^2}\right)\mathbf{E} = \mu_0 \frac{\partial^2}{\partial t^2}\mathbf{P}. \tag{2.5}$$

The interaction with a material is split into two parts: into a resonant part represented by the polarizability $\mathbf{P}$ and a general and constant material response represented by the dielectric function ε. In the fully coherent regime, the dielectric function can be assumed to be constant; for weak incoherent carrier occupations it is safe to assume macroscopic constancy of this value as well.

In vacuum, the wave equation becomes homogeneous and the dielectric constant $\varepsilon = 1$, yielding an analytical solvable equation. One of the most used and most convenient solutions to this problems are monochromatic plane waves given by

$$\mathbf{E}(\mathbf{r}, t) = \mathbf{E}_0 \exp\left[i\left(\mathbf{k} \cdot \mathbf{r} - \omega t\right)\right] \tag{2.6}$$

Basically, any spectroscopic problem can be broken down to the propagation of such plane waves and, therefore, they are a most versatile tool in the description of wave propagation optics. It becomes obvious from the source term in Eq. 2.5 that the interaction with a material is solely due to the polarization of the atomic orbitals. Actually, to anticipate quantum-mechanical dynamics described later in more detail, the light creates a quantum mechanical state as superposition between excited and ground states in matter, at least in a simple two-level scheme. This superpositional state dephases if the driving wave vanishes leading to the possible creation of carriers in the excited state. With the creation of carriers the system enters the incoherent regime, i.e., the excitation lost its phase relative to the driving wave. In semiconductors, it is necessary to have sufficient energy to surpass the energy gap of the material to create a significant carrier population. In this regime, the quantum mechanical nature of the incident light becomes important, leading to absorption of the incident photons through the photoelectric effect.

However, in a more detailed view the states of the incident photon and the materials excitation mix as well forming new quasi-particles called polaritons. Polaritons generally

describe photon-excitaton mixing waves inside materials, therefore, several types of them exist, such as exciton-polaritons, plasmon-polaritons, phonon-polaritons and many more. The regime in which such signatures arise in spectroscopic experiments is commonly termed the strong-coupling regime[26]. Polaritonic effects are more and more exploited for technological uses, such as the polariton laser[27,28], polariton cooler[29] and many more[30,31]. Albeit, its use in common functionalized materials for mass-market applications is rather limited. Already the roughness of interfaces or the surface of a sample can destroy the narrow spectral features arising from polaritonic resonances. Not surprisingly, such resonances do mostly not show in heterostructure devices, since they often exhibit internal interface roughness, strain or alloy fluctuations to a certain degree.

If the photon finally is absorbed in the material, an electron hole pair is created in the material. This pair, a so-called exciton, is attracted by the Coulomb force lowering the fundamental band gap energy by the exciton binding energy. Therefore, the first exciton resonance is below the actual band gap energy of the material, which is visible in both, emission and absorption of a material. Generally, the binding energy of excitons scale with the size of the band gap and its resonances are similar to the orbital state resonances of a hydrogen atom altered by the dielectric environment. This similarity makes it possible to measure Rydberg series of excitons in reflection or absorption measurements[32,33]. However, for III-V semiconductors with band gap energies in the near infrared regime, the exciton binding energy is often below the inhomogeneous broadening and therefore not visible in most experiments, e.g., GaAs has a exciton binding energy of 4.2 meV[34]. Nevertheless, it is important to note that all emission and absorption resonances are mostly arising from the 1s state of the exciton even if there is no excitonic population inside the sample. This behaviour and a further discussion of influences of dimensionality, defects or interfaces will be given in Sec. 2.1 of this chapter.

If the incident photon energies are too low to excite carriers according to the photoelectric effect the wave simply propagates along the material interacting with the induced polarization. In certain, non-centrosymmetric materials this polarization is non-centrosymmetric as well, creating frequency mixing phenomena according to an anharmonic oscillator model. This phenomenon is often described by the term non-linear optics, since the electrical susceptibility of the material has to be expanded by a Taylor series of the electric field to accurately describe the physics around this effect. Accordingly, these effects depend on the incident electric field strength. Since such effects are rather weak, they became of importance with the invention of the laser in 1960 by Maiman[9], providing sufficiently strong fields to significantly exploit such effects. Nowadays, non-linear effects are a standard tool in each spectroscopic laboratory, e.g., for reaching unreachable wavelengths through frequency mixing or second harmonic generation (SHG) as well as high harmonic generation (HHG). A detailed theoretical description of such effects will take place in Sec. 2.2 of this chapter.

2.1 Absorptive Optics in Semiconductors

Crystalline semiconductors exhibit periodic crystal lattices with certain symmetric properties. The complex interplay of the mixing of the outer shell single atomic orbitals of the constituents determine their material properties. The challenging part of the light interaction in crystals is: the transition from the interaction of light with the orbitals of a single atom to the interaction of simultaneous interaction with 10^{23} atoms and

their corresponding orbitals. Accordingly, each light-induced change in the material has to be treated not only in the scheme of this single interaction event but also in the response of the surrounding system, leading to a vast correlation of interactions. Light-matter interaction is mostly governed by the change of electronic motion and occupation or lattice vibrations, therefore, Coulomb interaction between electrons and atomic binding strengths between the atoms become important. It is convenient to deal with such transitions in reciprocal space when the dispersion relation, i.e., the wave vector (k) dependence of the energy is known. This dependence is termed the band structure of a material and first treatments of it started in the 1920s[35,36] and lead to rigorous calculations in the 1950's.

2.1.1 Band Structure and Density of States

Theoretically, the transition from single atoms to a crystal lattice can be treated in two ways: as the free dispersion of an electron perturbed by the surrounding atoms and as mixing of the discrete lines of the crystals atoms. Electron perturbations are the method of choice for conduction-band calculations. Contrary, the valence band can be accurately described by the mixing of atomic levels. This mixing smears the single atomic energies to broadened bands with many electronic levels giving rise to the band structure. The transition from the free electron energy given by $E(k) \propto k^2$ to a reduced band structure scheme is given in Fig. 2.1.

The periodic potential of the atoms and electrons is the foundation of a band structure treatment, i.e., the electronic potential is assumed to fulfill

$$V(\mathbf{r} + \mathbf{R}) = V(\mathbf{r}), \tag{2.7}$$

where $\mathbf{r}$ is the space coordinate and $\mathbf{R}$ is the periodicity of the potential. With this periodicity there exists a solution of the Schrödinger equation of the form

$$\psi_{\mathbf{k},i}(\mathbf{r}) = e^{i\mathbf{kr}} u_{\mathbf{k},i}(\mathbf{r}) \tag{2.8}$$

with $u_{\mathbf{k},i}(\mathbf{r}) = u_{\mathbf{k},i}(\mathbf{r} + \mathbf{R})$. k represents the wave vector and i is the index of the band. This is known as Bloch's theorem, established by its eponym Felix Bloch in 1929[35]. Similarly the eigenenergies are periodic in k-space:

$$E_i(\mathbf{k}) = E_i(\mathbf{k} + \mathbf{G}). \tag{2.9}$$

Accordingly, Bloch's theorem exists in k-space, too:

$$\psi_{\mathbf{k}+\mathbf{G},i}(\mathbf{r}) = \psi_{\mathbf{k},i}(\mathbf{r}). \tag{2.10}$$

This relation enables to reduction of the band structure zone schemes to the first Brillouin zone, which is bound by $k = \pm\pi/a$. A basic approach of deducing the zone scheme is to introduce the Bloch wave function (2.8) into the Schrödinger equation and to cancel the exponential functions out, yielding

$$\left[\frac{\hbar^2}{2m}\left(-i\nabla + \mathbf{k}\right)^2\right) + V(\mathbf{r})\Bigg] u_{\mathbf{k},i}(\mathbf{r}) = E_{\mathbf{k},i} u_{\mathbf{k},i}(\mathbf{r}). \tag{2.11}$$

The simplest solution can be found in the empty lattice approximation[37], where $V(\mathbf{r}) = 0$, i.e., the electrons see no potential and are in free space. A solution is the constancy

of the Bloch function ($u_{\mathbf{k}} = \text{const.}$), thus the gradient vanishes leading directly to the dispersion relation

$$E(\mathbf{k}) = \frac{\hbar^2}{2m}\mathbf{k}^2. \tag{2.12}$$

This is as expected for a vanishing surrounding potential the dispersion relation for an electron in vacuum. Since it contains the free electron mass m, it can be used to generalize the concept of the particles mass to the effective mass, present in the vicinity of a potential. Accordingly, $E(\mathbf{k})$ is derived two times to strip the wave vector from the equation, yielding after a rearrangement of Eq. 2.12

$$(m^*)^{-1} = \frac{1}{\hbar^2}\frac{\partial^2 E}{\partial k^2}. \tag{2.13}$$

The term m^* is then called the effective mass and is only dependent on the dispersion relation of a particle, i.e., yielding the free electron mass m in a potential free environment. With it is possible to describe the carrier mobility inside a material and, therefore, it is an important parameter for optical and electrical interaction. However, the aim is to describes electrons inside a material rather than in vacuum. Accordingly, a non-vanishing potential is present inside of Eq. 2.11, which is generally given by periodic lattice potential of the crystal under study. For a simple theoretical treatment the Kronig-Penney-model is often used[38], which employs a periodic rectangular potential, i.e., a superlattice or periodic quantum well structure. With this simplification Eq. 2.11 is solved analytically, leading to an equation of wave vector and energy $k(E) \propto \arccos L(E)$. The right-hand side $L(E)$ is part of the solution and is not restricted between 0 and 1 (for a full form of the function see Seeger[39]). Therefore, for some values of E the relation may not have a solution: a band gap exists, i.e., no states exist at these energies. This is due to the mixing of inter-potential wave functions, where standing waves are created to fulfil the boundary conditions in the periodic lattice. The outcome can be interpreted as crude approximation to an atomic lattice, where the atomic orbitals are assumed to be rectangular. Whilst changing the parameters of the model, i.e., the relation between potential thickness and distance, the mixing behaviour of the wave functions can be studied.

In the extreme case, where the potential thickness is zero the model resembles the empty lattice approximation, yielding the free electron dispersion (grey in Fig. 2.1). As the potential thickness is increased the free electron dispersion slowly is shifted away (thus creating a gap) at the boundaries of the reduced zone scheme (black in Fig. 2.1), which are tied to π/a due to the periodicity of the arccos function. For some bands the curvature becomes negative ($k = 0$ in the middle band in Fig. 2.1), therefore the effective mass is negative as well. Since such a negative mass is not physically meaningful, this behaviour is attributed to hole quasi-particles, i.e., an electron vacancy in the corresponding band. This explanation scheme is very convenient for the treatment in semiconductors, since the most of the behaviour can be modeled much easier (e.g., recombination is the interaction of an electron with a hole).

However, the Kronig-Penney model is of course over-simplified to explain the band structure of a real atomic lattice. The structure of such lattices are not only inherently three dimensional, but also exhibit more symmetric properties and the atoms have many energy levels they provide for wave function mixing. Therefore, the deduction of a band structure of a common semiconductor is less easy and often computationally expensive, i.e., the problem can only be solved numerically. Two very common approaches of band

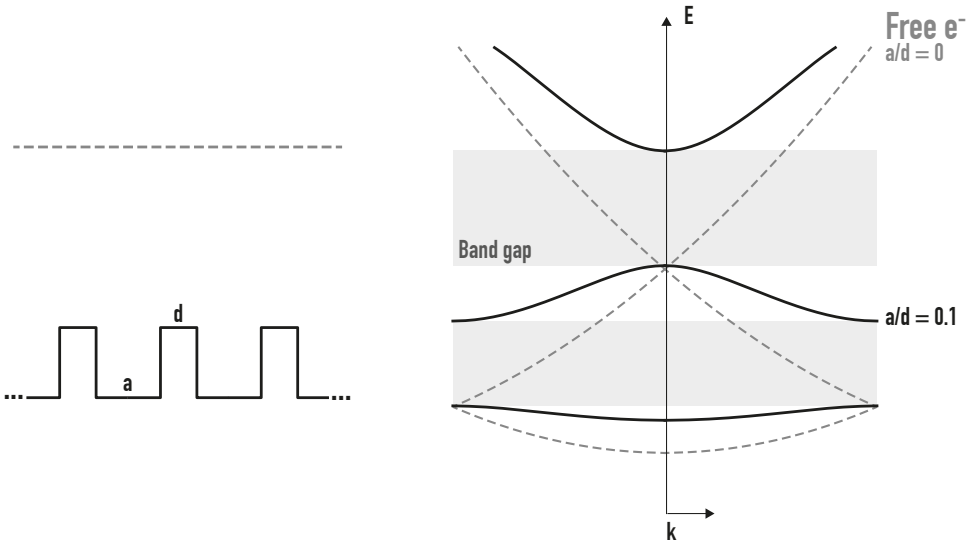

Figure 2.1: Band structure of the empty lattice approximation (dashed grey lines) and of the Kronig-Penney model (solid black line). The left side depicts the potential and the right side their electronic dispersions.

structure calculations are the $k \cdot p$-method or the Korringa–Kohn–Rostoker-method. Nevertheless, they both still need many material parameters, which have to be deduced experimentally and therefore there exists the attempt to use ab-initio methods, such as density functional theory (DFT). DFT mostly is used in the calculation of molecular orbit theory to deduce the orbitals of a single molecule or simple complexes. Unfortunately, the method is weak in the deduction of excited states as well as absolute energy scales, therefore the derivation of band gap energies is very faulty. Nowadays, various approaches overcoming these shortcomings exist, e.g., by using better functionals[40] or combining DFT and $k \cdot p$ calculations[41].

For a typical direct-gap zinc-blende structure III/V semiconductor (such as GaAs) the valence band is mainly created from s and p orbitals of the constituting atoms. This process is called sp^3 hybridization. A simplified band structure of a such a material shows mainly a parabolic conduction band (band above the energy gap in Fig. 2.2) and three valence bands. In unstrained materials, the two upper valence bands are degenerate and exhibit two different slopes (two black bands below the energy gap in Fig. 2.2). According to the effective-mass formula (Eq. 2.13) they can be attributed to heavy-holes and light-holes, respectively. The lower valence band (grey in Fig. 2.2) is the split-off band due to the spin-orbit interaction of the electrons. Under equilibrium conditions, the bands are fully filled up to the Fermi energy E_F, which lies in the energy gap for semiconductors, and as electrons are Fermions they fulfil the Fermi-Dirac-Distribution

$$f(E) = \frac{1}{\exp\{(E - E_F)/k_b T\} + 1}, \tag{2.14}$$

yielding the occupation probability $f(E)$ of a state with energy E. k_b is the Boltzman constant and T is the temperature of the material. The distribution is shown on the right side in Fig. 2.2. Folded with the density of states (DOS) (left side in Fig. 2.2) it yields the total occupation at temperature T. The DOS itself describes the number of energy

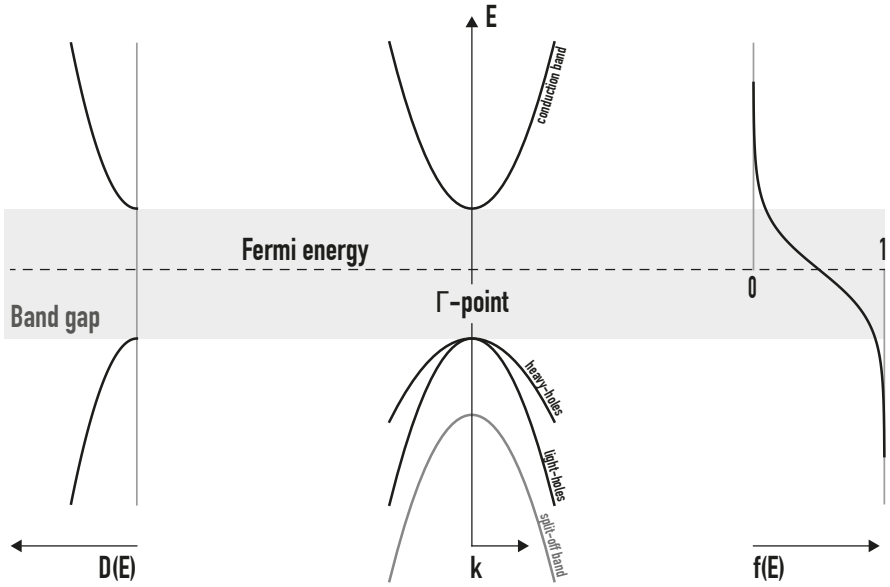

Figure 2.2: Typical band structure scheme of a III/V semiconductor (middle) with the conduction band (upper parabola) and the three valence bands (lower three parabolas). The left and right sides show the materials density of states and its Fermi-Dirac statistic, respectively.

levels in an infinitesimal energy interval $E + dE$. It can be derived for a d dimensional Fermi gas (where $k \propto \sqrt{E}$ according to Eq. 2.12) very easily. The number of states can be found by the integral

$$D(E)dE \propto \int d^d\mathbf{k}\delta\left(E - E(k)\right). \tag{2.15}$$

The k-space infinitesimal element can be converted to the wavenumber according to $d^d\mathbf{k} \propto k^{d-1}dk$, carrying out the integral leads to $D(k)dk \propto k^{d-1}$. Substituting k for E in this relation yields

$$D(E)dE = D[k(E)]\frac{dk}{dE}dE. \tag{2.16}$$

Together with free electron dispersion (Eq. 2.12) we get the energy dependent DOS:

$$D(E)dE \propto E^{d/2-1}. \tag{2.17}$$

Accordingly, the three dimensional DOS has a root shape (as in Fig. 2.2), the two dimensional one is constant (i.e., a step function when higher states are present) and the one dimensional case shows an inverse root behaviour. Therefore, the one dimensional case shows a singularity at the edge and decays to zero the higher the energy.

For the full understanding and completeness the lattice temperature, i.e., the atomic distance variation with temperature, has to be taken into account. The semi-phenomenological Varshni formula[42]

$$E_g(T) = E_0 - \alpha\frac{T^2}{T+\beta} \tag{2.18}$$

with the material parameters α, β and the zero temperature gap E_0, describes this shift of the electronic band gap with temperature. This leads to an increase of the

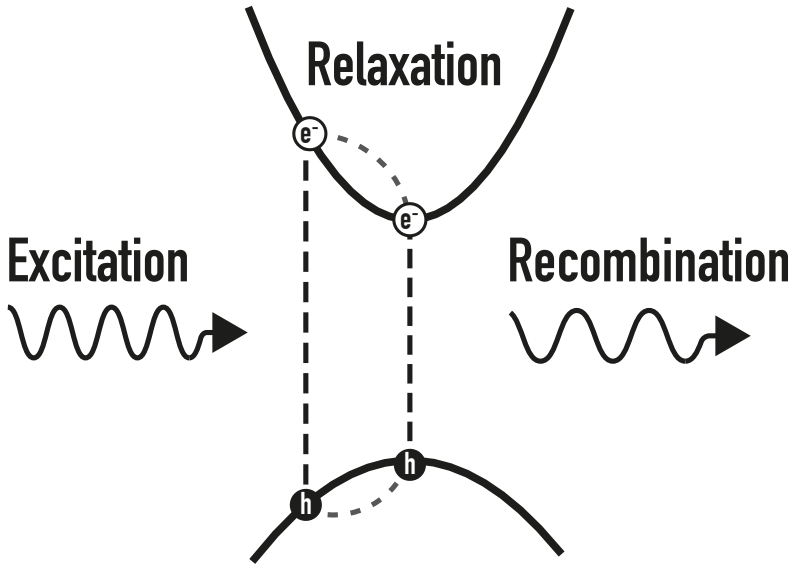

Figure 2.3: Simplified schematic of the photoluminescence process. A photon (wavy arrow on the left) excites an electron, creating an hole and an electron. The (quasi-)particles relax to the band minimum, where they recombine and emit a photon with a higher wavelength (wavy arrow to the right).

band-gap energy with decreasing temperature, altering the total occupations under equilibrium conditions. Regarding emission of light, the energy gap shift leads to a shift of the emission to higher energies with decreasing temperature. Nevertheless, there exist various approaches connecting the band gap change of temperature to intrinsic parameters of the semiconductor and is mentioned here for completeness. A generally accepted simple formula is

$$\Delta E_g(T) = \frac{\alpha \Theta_p}{2} \left[\sqrt[p]{1 + \frac{2T}{\Theta_p}} - 1 \right]. \tag{2.19}$$

Here, Θ_p is the average phonon temperature, α is related to the maximum (high temperature) entropy of the system and p is a material parameter related to the degree of phonon dispersion[43]. Accordingly, the formula enables to deduce microscopic quantities (e.g., phonon temperature) for a measured temperature dependence, yielding a more descriptive approach of the physics behind this shift. All considerations so far are for equilibrium conditions. If light interacts with the system the material the first approach is that the light is absorbed and the energy is transferred to an electron, lifting it from the valence band to the conduction band (Fig. 2.3). This action can take place whenever the energy of a photon itself is greater than the band gap energy. In this case, the electron populates the conduction band for a certain time T_2, which is in the order of 0.1 to 1 ps for common semiconductors (e.g., Si or GaAs) at room temperature. This radiative lifetime broadens the linewidth of the spontaneous emission which takes place after the decay time T_2 through the energy time uncertainty

$$\Delta E \cdot \Delta t \geq \hbar/2. \tag{2.20}$$

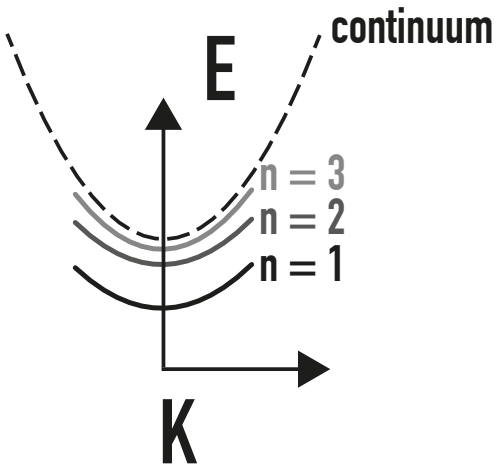

Figure 2.4: Excitonic levels ($n = 1 - 3$) below the conduction band. K is the center-of-mass momentum of the exciton.

However, the simple picture of photons lifting electrons in the band structure quickly fails. Since the band structure is a single particle picture in a periodic potential it does not take Coulomb interaction of the electron and its hole it leaves behind into account. The attraction between those two (quasi-)particles lead to a lowering of the fundamental gap energy, which is accurately described by the Wannier equation[44]:

$$\frac{\hbar^2\mathbf{k}^2}{2\mu}\phi_n(\mathbf{k}) - \sum_{\mathbf{k}'} V_{\mathbf{k}-\mathbf{k}'}\phi_n(\mathbf{k}') = E_n\phi_n(\mathbf{k}). \tag{2.21}$$

This equation is very similar to the Schrödinger equation of the hydrogen atom with the eigenfunctions and -energies ϕ_n and E_n. The system is simply altered by the dielectric environment through the dielectric constant ε contained in the Coulomb potential $V_{\mathbf{k}-\mathbf{k}'}$ and the reduced effective mass μ of electron and hole. This combined electron hole system bound by the Coulomb force is called an exciton and is per definition a quasi-particle, as it only exists in the vicinity of a dielectric environment. For parabolic bands and a direct gap semiconductor, the system can be transformed in the center-of-mass system, yielding the dispersion relation of excitons:

$$E(n, \mathbf{K}) = E_g - Ry^*\frac{1}{n^2} + \frac{\hbar^2\mathbf{K}^2}{2M} \tag{2.22}$$

with the scaled Rydberg energy $Ry^* = 13.6\text{eV}\mu/m_0\varepsilon^2$, translational mass M and exciton wave vector **K**. The radius of the exciton is scaled relative to the one of the hydrogen atom by $\varepsilon^2 m_0/\mu$. In inorganic semiconductors, excitons typically have a rather large radius (low binding energy), more specifically they are then called Mott-Wannier excitons[44]. For GaAs, the binding energy of the 1s exciton state is roughly 5 meV below the conduction band edge[34] and the exciton Bohr radius is around 10 nm. Contrary, in organic semiconductors the exciton is typically confined to a single molecule with a

comparable small binding radius (large binding energy), these are called Frenkel excitons[45]. Another species of excitons are charge-transfer or type-II excitons. They exist at the interface between two materials, i.e., electron and hole exist in another material. Generally, the exciton binding energy increases with increasing band gap. In second quantization, the excitons can be described by creation and annihilation operators, such as

$$X_{\mathbf{K}} = \sum_{\mathbf{k}} \phi_\lambda(\mathbf{k}) a^\dagger_{v,\mathbf{k}-\mathbf{K}_h} a_{c,\mathbf{k}+\mathbf{K}_e} \tag{2.23}$$

as an example for the exciton annihilation operator. $a^{(\dagger)}_{v/k}$ are the creation and annihilation operators for electrons in the conduction and holes in the valence band. $\phi_\lambda(\mathbf{k})$ is the wavelength dependent exciton wave function With the similar constructed annihilation operator $B_{\mathbf{K}}$ the excitons fulfil the permutation relation

$$\left\langle \left[X_{\mathbf{K}}, X^\dagger_{\mathbf{K}} \right]^- \right\rangle = 1 - \frac{4}{3}\pi \cdot n a_B^3, \tag{2.24}$$

i.e., for low densities n excitons behave bosonic, becoming more and more fermionic for higher densities until they end up in an uncorrelated electron-hole plasma which can only be described by Fermi-Dirac-statistics. a_B^3 describes the exciton volume in a bulk crystal, which can be easily transferred to lower dimensional systems, where the term is simply $\propto a_B^d$ with dimension d.

2.1.2 Absorption

The optical interaction presented in this work is mainly governed by exciton resonances and contributions from the electron hole plasma. To accurately determine optical absorption or emission properties of an ideal semiconductor, the system has to be treated fully quantum mechanically or at least semi-classical (for absorption). Neglecting vibrational effects, the system Hamiltonian in the semi-classical case is of the form

$$H = H_e + H_{e-e} + H_{e-EM}. \tag{2.25}$$

The first part, H_e, describes the occupation and dispersion of the electrons in the material, H_{e-e} is the electron-electron Coulomb scattering term and H_{e-EM} describes the interaction of electrons with the electric field. The electron occupation is determined by using the counting operator constructed from the ladder operators $a^{(\dagger)}_{\lambda,\mathbf{k}}$ for the conduction ($\lambda = c$) and valence band ($\lambda = v$), respectively. This yields

$$H_e = \sum_{\mathbf{k}} E^c_{\mathbf{k}} a^\dagger_{c,\mathbf{k}} a_{c,\mathbf{k}} + \sum_{\mathbf{k}} E^v_{\mathbf{k}} a^\dagger_{v,\mathbf{k}} a_{v,\mathbf{k}} \tag{2.26}$$

for the free electron Hamiltonian, including the conduction band and valence band energies $E^\lambda_{\mathbf{k}}$.

The scattering contribution reads

$$\begin{aligned} H_{e-e} = \sum_{\mathbf{k},\mathbf{k}',\mathbf{q}\neq 0} \Bigg(& \frac{1}{2} V_{\mathbf{q}} a^\dagger_{c,\mathbf{k}+\mathbf{q}} a^\dagger_{c,\mathbf{k}'-\mathbf{q}} a_{c,\mathbf{k}'} a_{c,\mathbf{k}} \\ & + \frac{1}{2} V_{\mathbf{q}} a^\dagger_{v,\mathbf{k}+\mathbf{q}} a^\dagger_{v,\mathbf{k}'+\mathbf{q}} a_{v,\mathbf{k}'} a_{v,\mathbf{k}} \\ & - V_{\mathbf{q}} a^\dagger_{c,\mathbf{k}+\mathbf{q}} a_{v,\mathbf{k}'} a^\dagger_{v,\mathbf{k}'-\mathbf{q}} a_{c,\mathbf{k}} \Bigg). \end{aligned} \tag{2.27}$$

In this scattering Hamiltonian, the first two terms on the right-hand side of the equation represent the electron-electron (1^{st} line) and hole-hole (2^{nd} line) scattering, i.e., two particles with wave vectors $\mathbf{k}$ and $\mathbf{k}'$ get annihilated and create two particles with new wave vectors $\mathbf{k}+\mathbf{q}$ and $\mathbf{k}'-\mathbf{q}$. The last term includes interband effects between the electrons and holes, i.e., electron hole scattering.

The last part of the systems Hamiltonian is also the most important for light matter interaction, the coupling to the electromagnetic field:

$$H_{e-EM} = -E(t)\sum_{\mathbf{k}}\left(d^*_{cv}a^\dagger_{v,\mathbf{k}}a_{c,\mathbf{k}} + d_{cv}a^\dagger_{c,\mathbf{k}}a_{v,\mathbf{k}}\right). \tag{2.28}$$

Here, $E(t)$ is the classical electromagnetic field strength, the d's represent the transition dipole moments for the creation of an electron from an hole ($a^\dagger_{c,\mathbf{k}}a_{v,\mathbf{k}}$) or vice versa ($a^\dagger_{v,\mathbf{k}}a_{c,\mathbf{k}}$). The transition dipole moment is represented by expansion of the macroscopic polarization P into the Bloch basis

$$P = \sum_{\mathbf{k}} d_{cv}P_{\mathbf{k}} + c.c. \tag{2.29}$$

With the Heisenberg equation

$$i\hbar\frac{\partial}{\partial t}\langle O\rangle = \langle[O,H]\rangle \tag{2.30}$$

and the full Hamiltonian (Eq. 2.25) the dynamics of the polarization $P_{\mathbf{k}}(t)$ can be calculated. To reach this goal, the commutators of the Heisenberg equation have to be carried out. Unfortunately, one not only gets a single particle density matrix through the free electron/hole Hamiltonian and the interaction term, but four operator terms from the Coulomb interaction, too. Accordingly, the equation expands further and further and has to be truncated at some point. A method to do this in a self-consistent fashion is the cluster expansion approach, which is presented in Kira and Koch[46]. In this approach, the expectancy value of N interacting particles are expressed as N particle interaction with an additional full correlation term containing the $N+1$ interaction alone. Therefore, the interaction is said to be clustered into singlet, doublet etc. interactions (up to N). The additional $N+1$ correlation term is truncated, stopping the expansion of the equation and closing it to a N particle problem for an expectancy value for N particles, thus making the equation analytically solvable. With this approach, the equation is reduced to a closed form: the two band semiconductor bloch equations (SBEs): They read as

$$\begin{aligned}\left[i\hbar\frac{\partial}{\partial t} - E'^{\,e}_{\mathbf{k}}(t) - E'^{\,h}_{\mathbf{k}}(t)\right]\mathbf{P}_{\mathbf{k}}(t) \\ = -\left[1 - f^e_{\mathbf{k}}(t) - f^h_{\mathbf{k}}(t)\right]\Omega_{\mathbf{k}}(t) + \frac{\partial}{\partial t}P_{\mathbf{k}}(t)\end{aligned} \tag{2.31}$$

$$\frac{\partial}{\partial t}f^\lambda_{\mathbf{k}}(t) = -\frac{2}{\hbar}Im\left[\Omega_{\mathbf{k}}(t)P^*_{\mathbf{k}}(t)\right] + \frac{\partial}{\partial t}f^\lambda_{\mathbf{k}}(t). \tag{2.32}$$

The $f^\lambda_{\mathbf{k}}$ represent the occupation probabilities for electrons ($\lambda = e$) and holes ($\lambda = h$), respectively.

$$\Omega_{\mathbf{k}} = d_{cv}E(t) + \sum_{\mathbf{k}\neq\mathbf{k}} V_{|\mathbf{k}-k'|}P_{\mathbf{k}}(t) \tag{2.33}$$

is the Rabi energy which is renormalized due to Coulomb screening. The energies

$$E'^{\lambda}_{\mathbf{k}}(t) = E^{\lambda}_{\mathbf{k}} - \sum_{\mathbf{k}' \neq \mathbf{k}} V_{|\mathbf{k}-\mathbf{k}'|} f^{\lambda}_{\mathbf{k}'}(t) \tag{2.34}$$

are renormalized as well. A description of polarization dephasing, screening of the interaction potential or relaxation of carrier distribution is beyond the scope of the generic SBEs, since such effects are not included. To include such effects, time dependent correction factors for the polarization and occupation probabilities are introduced at the end of Eq. 2.31 and Eq. 2.32. Since they are not of major interest for the absorptive behaviour studied here, their full form is only given in the Appendix or in Koch and Kira[47] or Haug and Koch[48]. However, in the case of weak electric field strengths acting upon the system the generic SBEs are still able to accurately describe the effects taking place. If static conditions and vanishing (or at least low) carrier occupations are assumed, i.e., the system is in equilibrium and not under illumination, Eq. 2.31 is homogeneous and breaks down to the Wannier equation (2.21). Since the wave functions of the Wannier equation are well known due to the hydrogen problem, they can be used to deduce a solution for the inhomogeneous part of the SBE (the system is illuminated: $E(t) \neq 0$), yielding

$$\chi(\omega) = 2|d_{cv}|^2 \sum_{\lambda} \frac{|\phi_\lambda|^2}{E_\lambda - \hbar\omega - i\gamma}, \tag{2.35}$$

with a phenomenological dephasing factor γ. This is the Elliot formula[49] for the linear semiconductor susceptibility, thus describing the absorptive behaviour of a semiconductor. Taking the imaginary part of Eq. 2.35 yields the absorption $\alpha(\omega)$ for a material.

Viewing the resulting absorption spectrum reveals that the absorption is strongly governed by the Lorentzian shaped 1s exciton resonance, followed by less pronounced peaks for the 2s, 3s etc. resonances (Fig. 2.5 shows the behaviour for GaAs). Obviously, no p-type or higher orbital contributions are visible since their transition dipole moment is zero and excitons from this bindings are dark. Around the band-gap energy (E_g) the absorption coefficient becomes quasi-constant (zero in Fig. 2.5) and is enhanced due to Coulomb renormalization compared to the exciton free absorption edge. For higher photon energies the difference between the absorption with excitons and the exciton-free absorption vanishes due to the less importance of the Coulomb force in the electron-hole plasma.

Generally, the Coulomb interaction strength is given by the excitonic Rydberg constant (Ry^*), therefore the smaller Ry^* the more the Coulomb free absorption is resembled (Fig. 2.6a). Furthermore, the strength of the 1s peak gets weaker with decreasing Ry^* and higher resonances vanish in the absorption edge, i.e., the edge is red shifted due to the higher states and Coulomb enhancement. This is important that even for inorganic semiconductors with small band gap, where exciton resonances may not be visible, the effects still play a major role as a shift of absorption. For example the GaAs absorption edge gets shifted by about 25 meV, even if the broadening is so strong that no clear 1s resonance is visible. Generally, increasing broadening (introduced as phenomenological γ in Eq. 2.35) shifts the 1s peak maximum only weakly to higher energies (Fig. 2.6b). This mainly bleaches the resonance and broadens its Lorentzian line shape, yielding a strong red shift and less steep rise of the absorption edge. Figure 2.6b shows the change of the absorption for ten broadenings in between $\gamma\hbar = 10\,\text{meV} \ldots 50\,\text{meV}$.

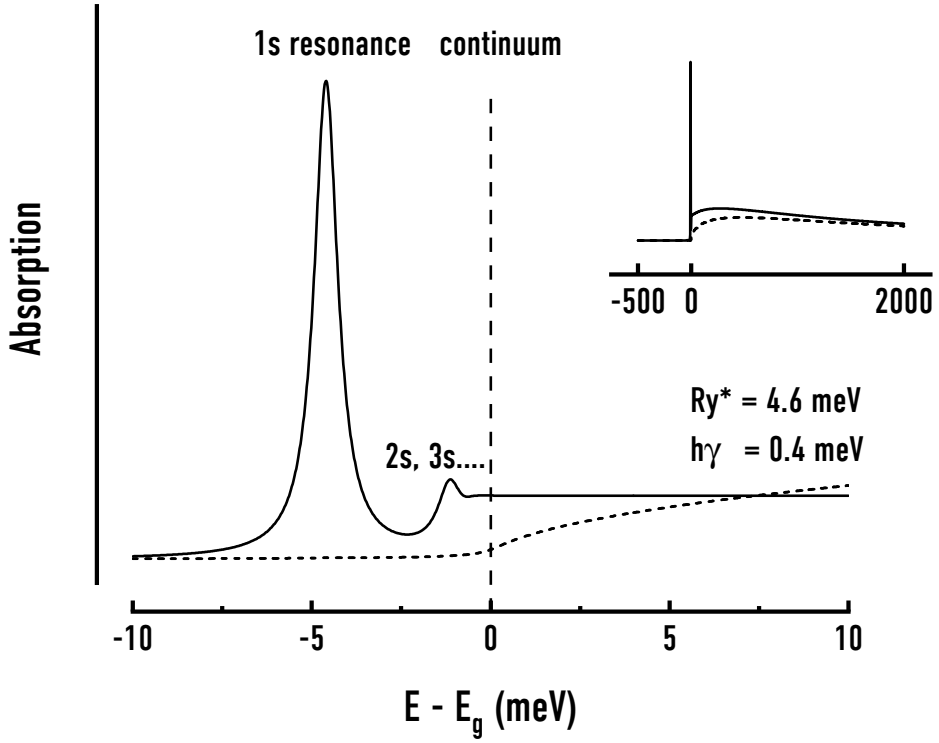

Figure 2.5: Absorption of GaAs (solid line) with a low broadening ($h\Gamma = 0.4\,\text{meV}$). The excitonic 1s and higher states are visible at the Rydberg energy and right before the continuum edge (dashed vertical line). For comparison the dashed line (scaled for visibility) depicts the absorption without excitonic effects. The inset shows a broader range of the absorption, visualizing the Coulomb enhancement in the continuum. The x-axis in both graphs depict the detuning, i.e. the difference to the band gap energy.

2.1.3 Photoluminescence

The derivation of photoluminescence can be done in the same framework as for the SBEs. However, spontaneous emission is an intrinsically quantum-mechanical effect, therefore, the problem has to be treated fully microscopic. Accordingly, the light field has to be quantized as well, changing the light field interaction Hamiltonian of Eq. 2.25 to

$$H_{e-EM} = \sum_{\mathbf{k},\mathbf{q}} \left(i\mathcal{F}_{\mathbf{q}} b_{\mathbf{q}} a^{\dagger}_{c,\mathbf{k}+\mathbf{q}} a_{v,\mathbf{k}} + i\mathcal{F}_{\mathbf{q}} b_{\mathbf{q}} a^{\dagger}_{v,\mathbf{k}+\mathbf{q}} a_{c,\mathbf{k}} \right) + h.c. \tag{2.36}$$

and replacing the electric field strength with its expectancy value

$$\langle E \rangle = \sum_{\mathbf{q}} \mathcal{E}_{\mathbf{q}} u_{\mathbf{q}} \langle b_{\mathbf{q}} \rangle + c.c.. \tag{2.37}$$

Thereby, $\mathcal{F}_{\mathbf{k}} = d_{cv}\mathcal{E}_{\mathbf{q}} u_{\mathbf{q}}$ denotes the interaction strength, with the vacuum field amplitude $\mathcal{E}_{\mathbf{q}}$ and the mode strength $u_{\mathbf{q}}$, i.e., it represents the wavefunction overlap between electron and hole states. $b^{(\dagger)}_{\mathbf{q}}$ denotes the creation and annihilation operators for photons with momentum $\mathbf{q}$, which is very small compared to the quasi-momentum of the carriers $\mathbf{k}$. The intensity of light is given by $\langle EE \rangle$, which contains the single particle photon

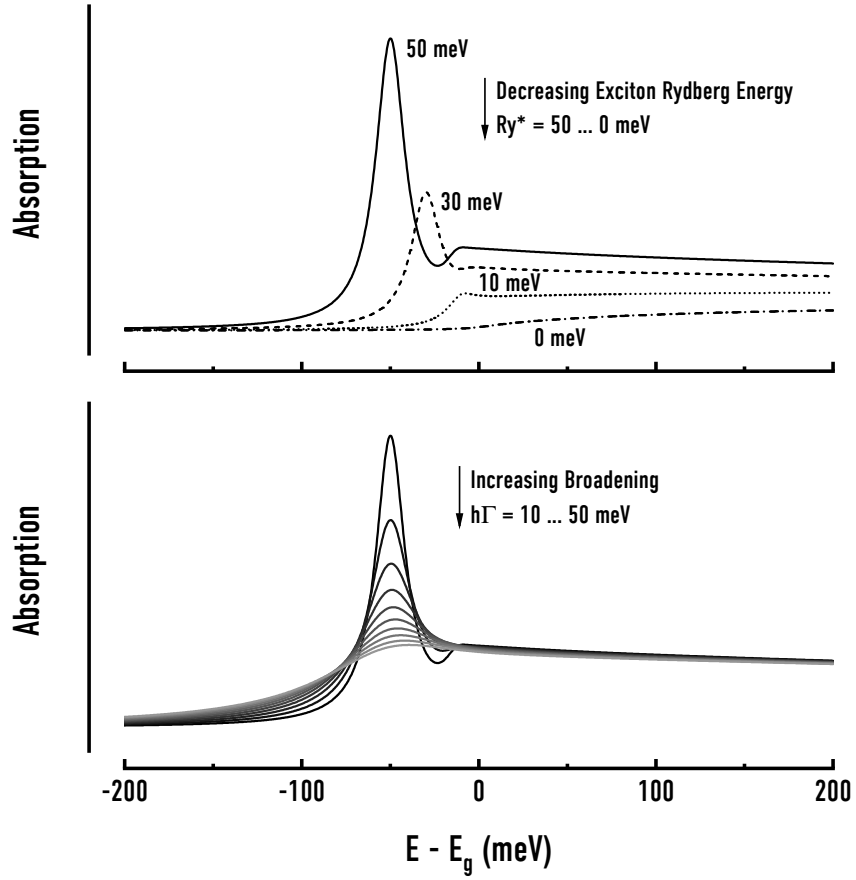

Figure 2.6: Influence of the Rydberg energy (upper graph) and the broadening (lower graph) on the absorption strength. The x-axis shows the difference to the band gap energy of the material.

expectancy values $\left\langle b^\dagger b \right\rangle$ and the change of photon quanta $\Delta \left\langle b^\dagger b \right\rangle = \left\langle b^\dagger b \right\rangle - \left\langle b^\dagger \right\rangle \left\langle b \right\rangle$. If pulsed excitation is assumed, the light field and polarization is decayed and the remaining radiative contribution stems solely from the quantum-optical intensity correlation $\Delta \left\langle b^\dagger b \right\rangle$. Using the Heisenberg equation-of-motion with the cluster expansion scheme again, yields for the temporal change of this intensity correlation

$$\begin{aligned} i\hbar \frac{\partial}{\partial t} \Delta \left\langle b^\dagger_{q_z} b_{q'_z} \right\rangle &= \hbar \left(\omega_{q'_z} - \omega_{q_z} \right) \Delta \left\langle b^\dagger_{q_z} b_{q'_z} \right\rangle \\ &\quad + i \sum_{\mathbf{k}_{||}} \left(\mathcal{F}_{q_z} \Delta \left\langle b_{q'_z} a^\dagger_{c,\mathbf{k}_{||}} a_{v,\mathbf{k}_{||}} \right\rangle + \mathcal{F}^*_{q'_z} \Delta \left\langle b^\dagger_{q_z} a^\dagger_{v,\mathbf{k}_{||}} a_{c,\mathbf{k}_{||}} \right\rangle \right). \end{aligned} \tag{2.38}$$

Thus, the equation describes the emission of light from a carrier distribution in the material. For a more convenient treatment, the material is assumed to be confined with the wave vector of the incident light parallel to the z-axis. The wave vector is therefore split in components in the area normal to it and one part parallel to it ($\mathbf{k} = (\mathbf{k}_{||}, k_z)$). The three parts of Eq. 2.38 resemble the existing photonic field, the absorption process, where a photon and a hole are destroyed and a conduction-band electron is created.

The last part contains the photon induced polarization term $\Delta \left\langle b^\dagger_{q_z} a^\dagger_{v,\mathbf{k}_{||}} a_{c,\mathbf{k}_{||}} \right\rangle$ which describes the creation of a photon by the annihilation of an electron and a hole. Thus, it contains the most part of the materials emission and is given by

$$\begin{aligned} i\hbar \frac{\partial}{\partial t} \Delta \left\langle b^\dagger_{q_z} a^\dagger_{v,\mathbf{k}_{||}} a_{c,\mathbf{k}_{||}} \right\rangle = & \left(E'^{\,c}_k - E'^{\,h}_k - \hbar\omega_{q_z} \right) \Delta \left\langle b^\dagger_{q_z} a^\dagger_{v,\mathbf{k}_{||}} a_{c,\mathbf{k}_{||}} \right\rangle \\ & - \left(1 - f^e_k - f^h_k \right) \Omega^{ST}_{\mathbf{k}_{||},q_z} \\ & + i\mathcal{F}_{q_z} \left(f^e_k f^h_k + \sum_{k'} \Delta \left\langle a^\dagger_{c,\mathbf{k}'_{||}} a^\dagger_{v,\mathbf{k}_{||}} a_{c,\mathbf{k}_{||}} a_{v,\mathbf{k}'_{||}} \right\rangle \right) \\ & + i\hbar \frac{\partial}{\partial t} \Delta \left\langle b^\dagger_{q_z} a^\dagger_{v,\mathbf{k}_{||}} a_{c,\mathbf{k}_{||}} \right\rangle \Big|_{scattering} . \end{aligned} \tag{2.39}$$

The first two terms of the equation represent the behaviour known from the SBEs in the fully quantum mechanical picture with the generalized Rabi energy

$$\Omega^{ST}_{\mathbf{k}_{||},q_z} = \sum_{q'_z} i\mathcal{F}_{q'_z} \Delta \left\langle b^\dagger_{q_z} B_{q'_z} \right\rangle + \sum_{\mathbf{k}'_{||}} V_{\mathbf{k}_{||}-\mathbf{k}'_{||}} \Delta \left\langle b^\dagger_{q_z} a^\dagger_{v,\mathbf{k}'_{||}} a_{c,\mathbf{k}'_{||}} \right\rangle . \tag{2.40}$$

The last line represents scattering terms introduced from third order correlation terms, i.e. it includes triplet contributions from the cluster expansion approach. Furthermore, the third term describes the source for light emission, coming either from an electron hole overlap ($f^e_k f^h_k$) or the exciton occupation sum. If slow varying densities are assumed the carrier populations f^λ and $\Delta \left\langle a^\dagger_{c,\mathbf{k}'_{||}} a^\dagger_{v,\mathbf{k}_{||}} a_{c,\mathbf{k}_{||}} a_{v,\mathbf{k}'_{||}} \right\rangle$ can be taken as constant. Further, neglecting higher-order scattering terms the equation can be solved analytically[48], yielding for the steady-state photon flux

$$I_{PL}(\omega_q) = \frac{\partial}{\partial t} \Delta \left\langle b^\dagger_q b_q \right\rangle = \frac{2|\mathcal{F}_q|^2}{\hbar} Im \left[\sum_\lambda \frac{|\phi_\lambda|^2 N_\lambda}{E_\lambda - \hbar\omega_q - i\gamma} \right] . \tag{2.41}$$

This is the photoluminescence Elliot formula, strongly resembling Eq. 2.35, but with an additional source term

$$N_\lambda = \sum_k |\phi_{\lambda,k}|^2 f^e_k f^h_k + \sum \phi^*_{\lambda,\mathbf{k}} \phi_{\lambda,\mathbf{k}} \Delta \left\langle a_{c,\mathbf{k}^\dagger_{||}} a_{v,\mathbf{k}'_{||}} a_{c,\mathbf{k}'} a_{v,\mathbf{k}} \right\rangle . \tag{2.42}$$

This term yields the actual carrier population in the material, either from the electron-hole-plasma (first sum) or excitonic occupation (second sum). A simple approach to this formula is to solve the density dependent Wannier equation (2.21), where the effective Coulomb potential $V_{k,eff} = (1 - f^e - f^h) \cdot V_k$ is used, numerically, yielding the exciton wave functions ϕ_λ. The photoluminescence intensity can then by calculated from these wave functions directly.

From the obvious similarities of the Elliot formulas for absorption (Eq. 2.35) and photoluminescence (Eq. 2.41) it is clear that the emission of a semiconductor is centered around the 1s exciton peak as well. In fact, even if no exciton population is present in the system the strongest emission stems from this resonance. Therefore, the character of the population cannot be determined by photoluminescence spectroscopy alone. Figure 2.7 shows a comparison of photoluminescence for no and for weak exciton populations in an ideal semiconductor. The electron-hole plasma is only visible as a weak side peak in the

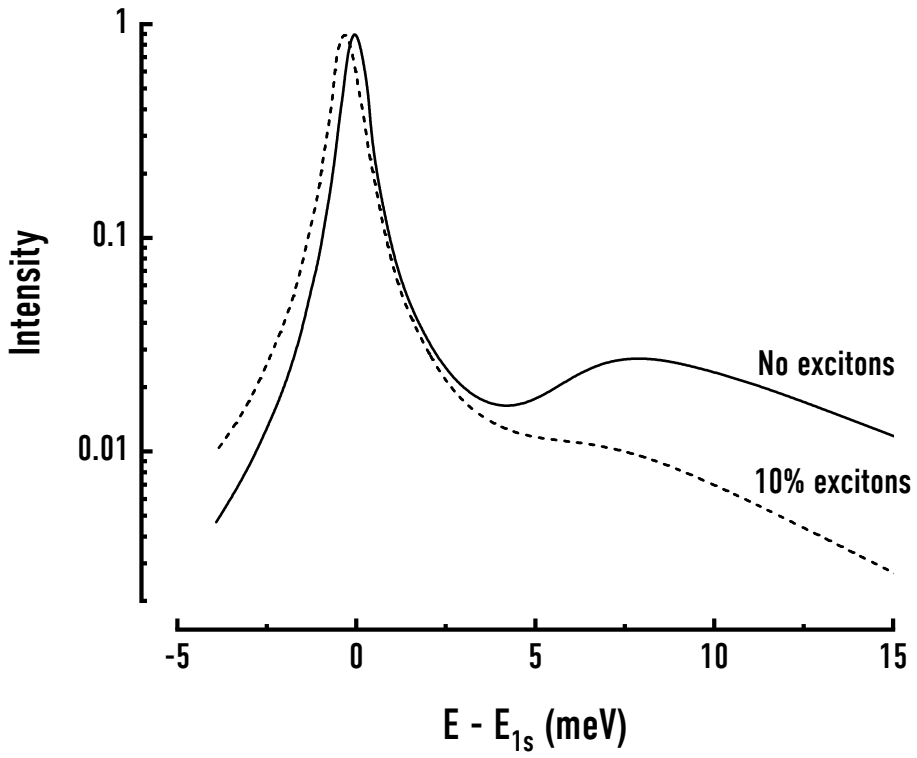

Figure 2.7: Theoretical photoluminescence for no (solid line) and 10 % (dashed line) of relative excitonic population. The energy axis is scaled with respect to the exciton 1s energy.

photoluminescence signal, barely visible in a non-logarithmic plot. Moreover, for small Ry^* or typical broadening this sideband vanishes completely, but it is still important to know that the emission is governed by the 1s peak and shifted accordingly, even for completely uncorrelated electron-hole pairs.

2.1.4 Influence of Strain and Localized States

There are various extrinsic and intrinsic parameters influencing the band gap of a semiconductor. The main dependencies are temperature, strain, composition, and localized states, which will be explained for nitrogen states in a semiconductor.

The influence of composition, i.e., band gap change in binary, ternary or quaternary alloys is treated in the virtual crystal approximation (VCA). Imagine a III/V ternary material of the atomic species A, B and C, where A and B have the same amount of valence electrons (i.e., are in the same periodic element table group) and C is their covalent counterpart. Therefore, the A, B to C ratio has to be 50 % and the ratio of A and B can be controlled during growth, yielding the compositional formula $A_xB_{1-x}C$, with the alloy fraction x. This yields for the energy gap of the material

$$E_g(A_xB_{1-x}C) = E_g(BC) + x\,[E_g(AC) - E_g(BC)] - bx(1-x), \tag{2.43}$$

where b is the phenomenological bowing parameter. This has to be introduced since the behaviour is often found to be non-linear and is therefore corrected to this slight changes

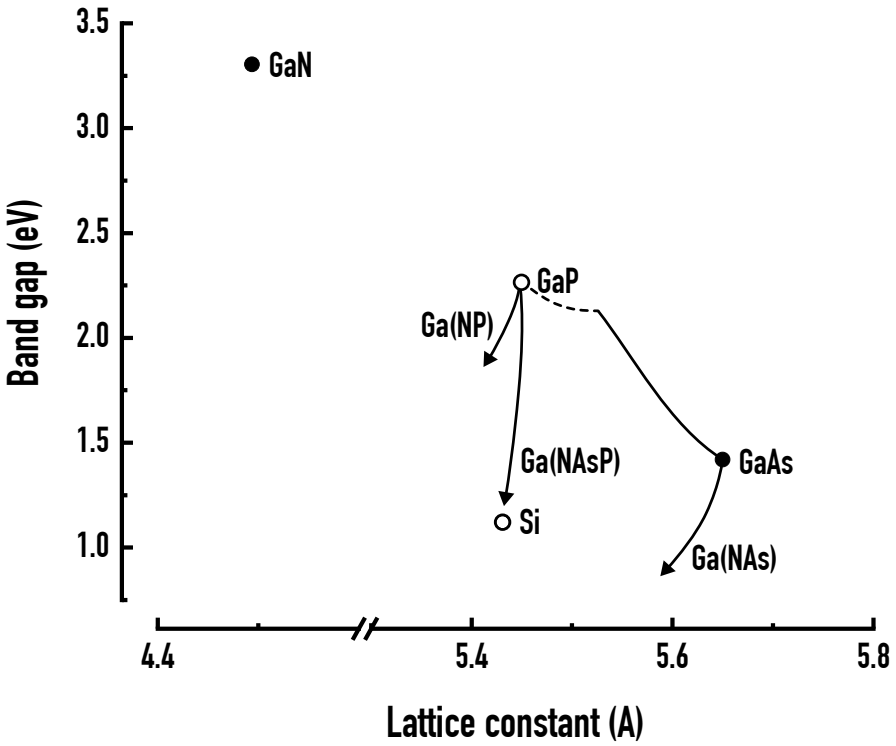

Figure 2.8: Gallium based materials band gap and lattice constant shift with respect to their composition. The arrows indicate the strong bowing introduced by the incorporation of nitrogen. Filled circles (solid lines) depict direct materials and hollow circles (dashed lines) indirect ones.

of the linearity. The VCA model can be easily expanded to quaternary materials, with a second alloy fraction y. Figure 2.8 depicts the change of band-gap energies and lattice constants depending on the composition for gallium-based systems.

Albeit most of the changes can be determined accurately, the change with nitrogen incorporation shows a rather strong bowing. Contrary to the excepted behaviour, a monotonic increase of the band gap from GaAs to GaP a huge bowing is observed, even lowering the band gap when small amounts of nitrogen are introduced into GaAs. This behaviour cannot be understood in terms of the VCA, which is due to the fact that nitrogen is partly diluted in the lattice of the material. Therefore, nitrogen acts as an isovalent local impurity level, leading to a dispersion less band in the structure of the material. For small doping levels of nitrogen in GaP, the local impurities lie energetically inside the band gap, giving rise to defect related photoluminescence (PL) and it further does not affect the band structure[50]. Contrary, in the case of GaAs the local impurity band lies within the conduction band of the material, leading to quantum mechanical anti-crossing effects. Generally, bands never cross each other in a band structure scheme, because a crossing always leads to a wave function mixing, which in turn creates new state bands. This behaviour may be described by the band anti-crossing (BAC) model.

In a simple two level description, the band gap splitting reduces to determinant equation

$$\begin{vmatrix} E - E_c & V \\ V & E - E_N \end{vmatrix} = 0, \tag{2.44}$$

where E_c is the conduction-band-edge energy (relative to the vacuum level), E_N is the impurity level energy and V is an empirical coupling constant. Solving of the determinant leads to the two new energy levels

$$2E_{\pm} = E_c + E_N \pm \sqrt{(E_c - E_N)^2 + 4V^2}. \tag{2.45}$$

This behaviour was studied in great detail for Ga(N,As)[51,52], (Ga,In)(N,As)[53] or other (qua)ternary materials[54]. With this model it is possible to accurately predict the band gap bowing in diluted nitrogen alloys.

Another effect on the band edges is due to strain inherent in the material. The strain tensor

$$2\epsilon_{ij} = \frac{\partial u_j}{\partial dx_i} + \frac{\partial u_i}{\partial x_j} \tag{2.46}$$

describes the infinitesimal length change of the material due to extrinsic strain. **u** is the displacement vector, pointing from the strain free position to the strained one. Thus, in one dimension the stress can be imagined to reflect an infinitesimal length change over the total length $\epsilon = \delta d/d$. It is convenient to split the strain into hydrostatic strain and shear strain. The hydrostatic strain is simply given by the trace of the tensor: $\epsilon_h = \mathrm{Tr}\,\epsilon = \epsilon_{xx} + \epsilon_{yy} + \epsilon_{zz}$. For a direct zincblende material the shift of conduction (ΔE_c) and valence band (ΔE_v) is only affected by the hydrostatic strain and given by

$$\Delta E_{c/v} = \Xi_{c/v}\,\mathrm{Tr}\,\epsilon, \tag{2.47}$$

with the hydrostatic deformation potential for either the conduction ($\Xi_c < 0$) or the valence band ($\Xi_v > 0$). These are material specific properties, relating the energy change of a material to its length change:

$$\Xi = a\frac{dE}{dx}, \tag{2.48}$$

where a is the lattice constant of the material. These potentials are mostly experimentally known and the deformation potentials for binary, ternary or quaternary systems can be calculated by VCA as well. With the strain induced changes for the bands (Eq. 2.47) the total energy gap change is calculated to

$$\Delta E_g = \Xi\,\mathrm{Tr}\,\epsilon, \tag{2.49}$$

with $\Xi = \Xi_c - \Xi_v$. Contrary, shear strain does not affect the edge energies but leads to a degeneracy lifting of the heavy-hole (hh) and light-hole (lh) valence bands

$$\Delta E_{v,hh-lh} = E_v^0 \pm E_{\epsilon\epsilon} \tag{2.50}$$

with the shear strain energy shift

$$\begin{aligned} E_{\epsilon\epsilon}^2 = {} & \frac{\Xi_b^2}{2}\left[(\epsilon_{xx} - \epsilon_{yy})^2 + (\epsilon_{yy} - \epsilon_{zz})^2 + (\epsilon_{xx} - \epsilon_{zz})^2\right] \\ & + \Xi_d^2\left[\epsilon_{xy}^2 + \epsilon_{yz}^2 + \epsilon_{xz}^2\right]. \end{aligned} \tag{2.51}$$

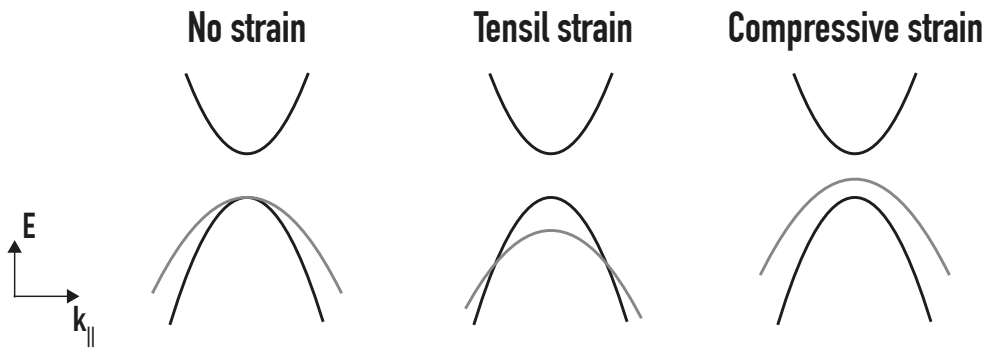

Figure 2.9: Shift of the hh and lh bands under tensile (middle) and compressive (right) strain. The shift of the band gap energy is not shown for clarity.

Here, $\Xi_{b/d}$ are the shear strain deformation potentials. Accordingly, there are two forms of strain possible: compressive or tensile strain. They lead to a different behaviour, for compressive strain the hh is lifted above the lh and for tensile strain it is the other way round (Fig. 2.9). For tensile strain, this leads to a complex behaviour due to the crossing and therefore mixing of the valence bands (right hand side in Fig. 2.9).

The influence of hydrostatic and shear strain acts on valence band and the effective masses of electrons and holes, as well. The behaviour is described with formulas very similar to Eq. 2.47 and a complete listing is found in Aspnes and Cardona[55].

2.1.5 Nonradiative Recombination

Various competitive processes to radiative recombination exist in ideal semiconductors. For instance, a third entity may be involved in the process and the energy difference may be dissipated thereby. This process is called Auger recombination after Pierre Victor Auger who described this process in 1923[56], although the effect was first discovered by Lise Meitner in 1922[57]. The basic scheme for Auger recombination is that the transition through the band gap is possible by intra-band lifting of either an electron in the conduction band or an hole in one of the valence bands (Fig. 2.10). Accordingly, the processes are termed eeh (two electrons) or hhe (two holes) Auger recombination, respectively. The probability for each scales with the carrier density, i.e., $\propto n^2p$ for eeh and $\propto np^2$ for hhe processes. A three-particle process it is statistically less favourable in most cases, however, it becomes more prominent for elevated carrier densities, e.g., for high excitation densities, high doping or temperatures, or for small band gaps (which in some terms also enriches the carrier density in the conduction band through Fermi-Dirac statistics).

The process may also occur phonon-assisted[58]. In that case, a k translation is possible during the process, enabling more carriers to participate in the process. Thus, the statistical probability is further enhanced.

The Auger effect can be used as tool for material analysis, i.e., here, the lifted electron is emitted to the vacuum level where it is detected. The energy of the emitted electron sheds light on the internal structure of the material. However, as spectroscopic tool the Auger effect is mostly restricted to lower material orbitals and thus not suitable to investigate the behaviour around the band gap. The counterpart of the Auger effect is

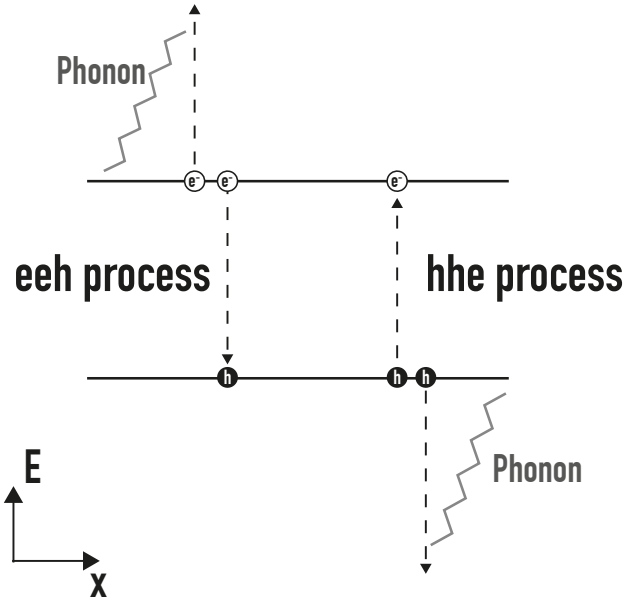

Figure 2.10: Auger recombination in the energy over space picture. The process can either happen with two electrons (left) or two holes (right). The recombination energy is transferred to the up(down)-lifting of an electron (hole). The graph shows the process in a phonon-assisted form, but up-lifting in higher bands is possible, too.

the impact ionization, which can result in an avalanche breakdown in the material. This breakdown is the basis of avalanche photodiodes, which are able to detect very low light intensities through this effect.

2.1.6 Influence of Defects and Disorder

Despite ideal semiconductors presented in the theoretical treatments in this chapter, several defects and disorder effects commonly determine semiconductor's response. Both are inevitable in the growth of such materials for thermodynamic reasons[26]. There are several defects, such as dislocations, stacking faults, grain boundaries or voids only to name a few. Nevertheless, the most influential defect regarding optical interaction is the point defect, i.e., an additional atom or atomic replacement in the crystal lattice. Such defects are present in a concentration around $10^{13} - 10^{17} cm^{-3}$ in typical materials. Commonly, point defects are characterized by their position in the band gap. They can either act as an electron donor, typically these are defects energetically near the conduction band edge, or as an electron acceptor, which are near the valence band edge (Fig. 2.11). Both defect types can be separated into neutral and ionized traps, i.e., for donors the exchange is through adding or removing an electron:

$$D^0 \leftrightarrow D^+ + e^-. \tag{2.52}$$

Similarly, an acceptor can be described by adding or removing an hole:

$$A^0 \leftrightarrow A^- + h. \tag{2.53}$$

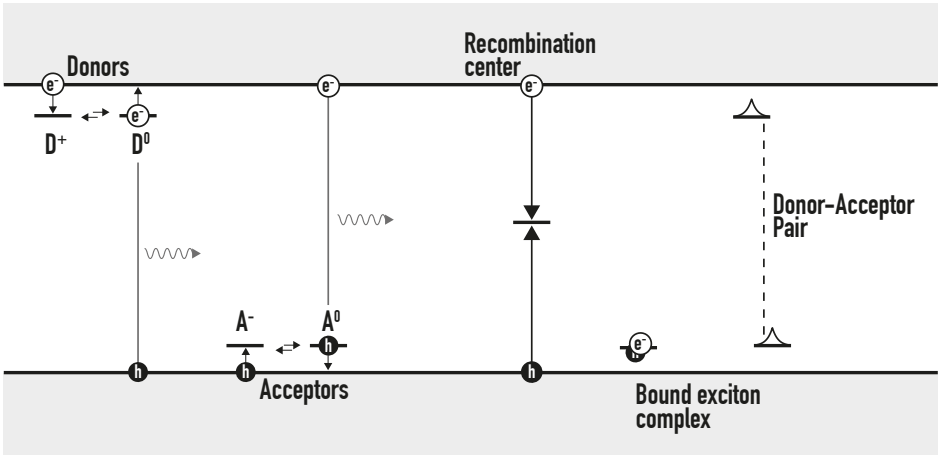

Figure 2.11: Energy vs. space diagram for possible point defects in a semiconductor. Shallow donors (acceptors) interchange from charged and neutral by emitting or collecting a particle. Recombination with the localized particles is possible (vertical lines), resulting in an emission of lower energy photons. A recombination center (middle) gives rise to an even lower emission wavelength. Each shallow donor or acceptor can bind an exciton, forming a bound exciton complex. If the wave functions of donor and acceptor overlap they form a donor-acceptor-pair (right).

Typically, these defects are two fold spin degenerate, but due to the spatial confinement one of the electrons is strongly blue shifted due to Coulomb repulsion[59]. These types of defects are generally called shallow traps. Whenever shallow traps are spatially near to each other and their wave functions overlap, they may form a donor acceptor pair, enabling an optical recombination channel with lowered transition energy compared to the band transition. Contrary, so-called deep traps occupy energies in the vicinity of the band gap. These are termed recombination centers if they are able to capture an electron or a hole. Such recombination centers show distinct optical features at energies considerably lower than the actual band gap energy (for examples see Klingshirn[26]).

In the band structure defects appear as dispersion less energy bands. Therefore, shallow traps represent a positively (negatively) charged center to which an electron (hole) can be bound. Accordingly, a localized exciton forms in the vicinity of an ionized shallow trap. Thus, the point defect is able to recombine, giving rise to emission bands below the energy gap transition of a material.

Moreover, trap levels can attract excitons themselves, a bound exciton complex (BEC) forms. This is typically denoted by an addition of a X to the defect symbol, e.g., D^0X for an exciton bound to a neutral donor. Generally, excitons can bind to any type of shallow trap, except for A^+X. In the ionized acceptor the binding to the free electron is energetically more favourable in most materials and therefore the exciton is less likely to bind to it. The binding energy of such BECs following in ascending order D^+X, D^0X and A^0X. Since the bound complex offers no translational freedom, the peaks in absorption or emission or usually very narrow in bulk structures. The visibility of these narrow lines depend on the concentration of the point defects. Otherwise, the peaks broaden due to BEC-BEC interaction, e.g., their statistical spatial distance is to small too regard them as real point defects. However, the peaks generally merge with the

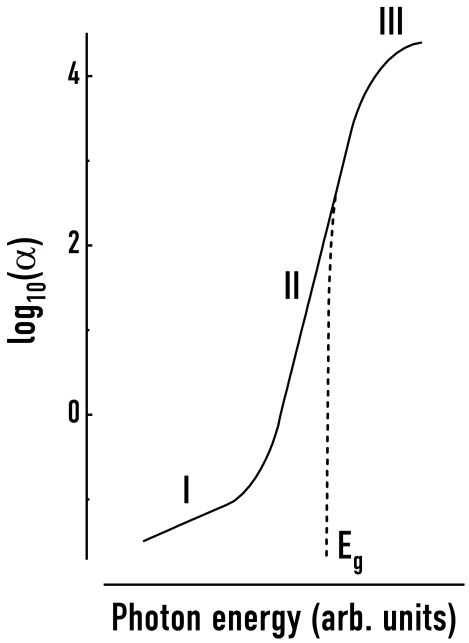

Figure 2.12: Various absorption regimes of the absorption coefficient in disordered semiconductors. Reproduced from Wood and Tauc[60].

free luminescence of the material for lower dimensional structures, such as quantum wells (QWs), and are therefore only visible as tailing structure. Three regimes (I, II and III in Fig. 2.12) are visible at the band edge of an absorption spectrum. The first one (I) is due to general alloy impurity or amourphousness in the material. The second (II) is the Urbach tail[26] which accounts for an exponential tail of the DOS due to localized excitons. This tail is often approximated with the formula

$$N(E) = \frac{N_0}{\epsilon_{loc}} \exp\left(-\frac{E}{\epsilon_{loc}}\right), \tag{2.54}$$

for E below E_g. ϵ_{loc} describes the density of localized states below the gap. For a thermal energy greater than the localization energy ($k_bT > \epsilon_{loc}$), the thermal reexcitation into extended states is possible. This is often observed in temperature-dependent PL experiments, where the change of emission energy deviates from the expected Varshni-like behaviour (Eq. 2.18) around a certain temperature (Fig. 2.13). This deviation is known as S-shape and is mainly divided in three regimes: at very low temperatures the carriers are frozen not able to move and hence not able to reach the traps. At slightly higher temperatures the carriers are able to diffuse and find the most favourable trap, therefore, the emission energy drops. Further increase of the temperature leads to thermal reexcitation, returning to the expected Varshni behaviour of temperature shift. This effect can be used to characterize the energetic position and amount (at least to a certain degree) in a material[61,62].

Drawing back to the absorption spectrum and the third regime (III): this is the so called Tauc regime and the behaviour in this regime can be approximated by the formula

$$(\alpha\hbar\omega)^n = A\left(\hbar\omega - E_g\right), \tag{2.55}$$

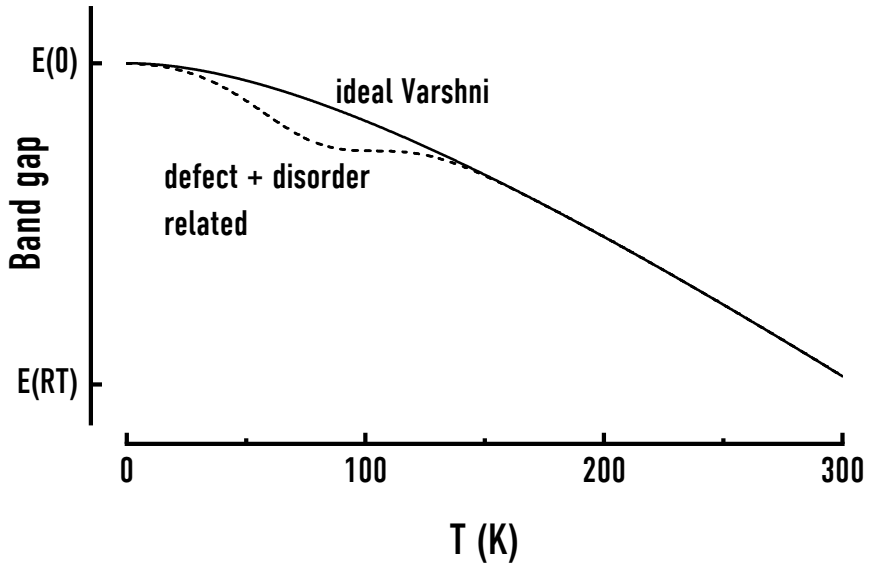

Figure 2.13: Example of the Varshni shift of band gap energy in dependence of temeparature (solid line). The dashed line shows a defect and disorder related curve with a change in a certain temperature range due to freezing into localized states.

where A is a fitting factor and n is an exponent to scale for the type of transition. It constitutes the following values:

- direct allowed: $n = 2$
- direct forbidden: $n = 2/3$
- indirect allowed: $n = 1/2$
- indirect forbidden: $n = 1/3$.

In comparison to the direct allowed transition described by the Elliot formula (Eq. 2.35) it is obvious that no excitonic effects are taken into account. Accordingly, the formula is a rather crude approximation as it only takes the root shaped DOS edge (for direct allowed) into account. Nevertheless, it is a valuable tool to investigate the underlying type of transition and to get a first estimate of the band gap energy for materials with low exciton binding energies and moderate broadening. Additionally, in most cases the exciton binding energy can be estimated at least to correct the Tauc fitted band gap energy.

Commonly, disorder has an effect on the optical properties as well. Mostly it arises from alloy fluctuations or geometrical defects. This is why such effects become important for lower dimensional structures, because the interface fluctuations are much more relevant in the materials response. To estimate the effects of disorder, two variations of the previous presented Kronig-Penney model exists: diagonal and off-diagonal disorder. The first describes a variation of the well depths in a certain interval, whereas the latter accounts for well-width fluctuations. Generally, a combination of both effects will occur in reality. Regarding diagonal disorder, the case is rather simple: the depth is smeared out around a mean well depth, leading to Gaussian decaying number of states for higher or lower energies around this mean value. Accordingly, the DOS is extended by a tail

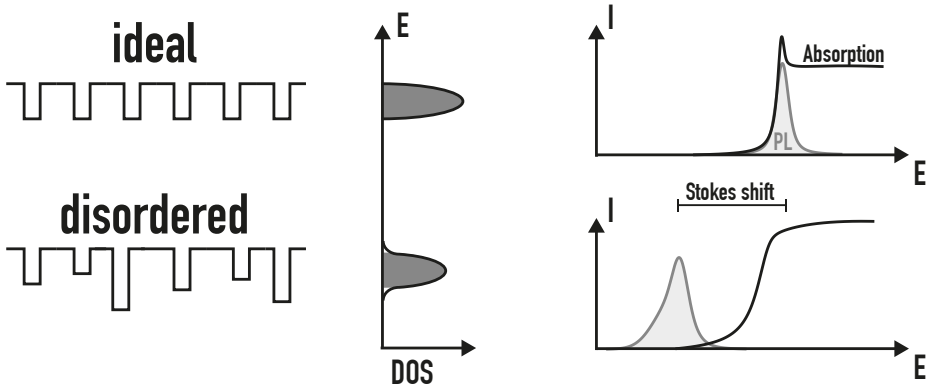

Figure 2.14: Influence of disorder in the Kronig-Penney model on the DOS (middle), PL and Absorption (right).

for these energies around the non-disordered genuine DOS (Fig. 2.14). Contrary, the off-diagonal disorder rather influences the form of the DOS, since the boundary conditions of the standing waves of the electronic wave functions change. All in all, the influence is mainly the existence of a tail at the onset of the DOS.

Due to the smearing the absorption of a material is generally broadened (as shown for different broadening scales in Fig. 2.6). This leads to a bleaching of the exciton 1s peak and general broadening of the edge. Another indicator of disorder is the shift between PL and absorption. This is due to the continuous nature of disorder, i.e., the carriers are able to diffuse to a lower energy and recombine afterwards. Accordingly, besides inhomogeneous broadening and the formation of a lower energy tail the PL shifts red, too. Since the absorption is assumed to not excite any carriers and is created solely from the induced polarization the spectrum reflects a statistical averaging across the disorder scale. As a consequence, there is a shift between absorption and emission of disordered samples, known as the Stokes shift[63]. This shift can be used to estimate the general disorder strength of a material.

2.2 Nonlinear Optics

The previous section treated the effects attributed to the absorption of photons in solids, mainly semiconductors. Absorption in this sense means that an electron transitions from one energy level to another. This transition is always enabled through the previous buildup of a polarization. This section describes the interaction of light with non-centrosymmetric solids in the polarization regime, i.e., the photon energy is typically lower than the band gap energy. Through the symmetry breaking in a material, the conversion of light into another energy becomes possible. This is due to the interaction of the induced electron motion (i.e. polarization) and the incident field, which happens at sufficient strong electric fields. Typical processes include the generation of optical harmonics, sum- or difference frequency generation if two beams are incident on sample. A prominent example is SHG, which is widely used in everyday devices (i.e., in green laser pointers) or in scientific research to reach other wavelength regimes. Franken et al. first described the effect of SHG, only one year after the invention of the laser byMaiman. Since then, the field of

Table 2.1: Transformation into the contracted notation of the non-linear coefficient d.

jk	11	22	33	23,32	31,13	12,21
l	1	2	3	4	5	6

non-linear optics emerged rapidly and nowadays there is a huge range of devices from parametric amplifiers to high-harmonic generation to reach deep ultra violet (UV) light. Time domain spectroscopy became possible over a wide energy range as ultra-short laser systems became available. These sources supply much larger field strengths than continuous wave lasers which further enhance the non-linear processes.

The description of non-linear interaction is mainly through the relation of polarization and electric field, which typically reads

$$P(t) = \epsilon_0 \chi E(t). \tag{2.56}$$

However, this treatment is not sufficient when E(t) becomes strong, since the polarization itself emits light due to acceleration and deceleration of electrons. The solution to this problem is to expand the polarization in the electric field, yielding

$$P(t) = \epsilon_0 \left(\chi^{(1)} E(t) + \chi^{(2)} E^2(t) + \chi^{(3)} E^3(t) + \dots \right) \tag{2.57}$$

Therefore, the polarization generation becomes field dependent with proportionality constants of different order. Typically, the second and third order expansions are treated for most materials. Their strength is generally relatively weak, i.e., $\chi^{(2)} \approx 1pm/V$ and $\chi^{(3)} \approx 1pm^2/V^2$.

The non-linear polarizations are generally due to spatial asymmetry; hence a non-centrosymmetric material is necessary to create a bulk non-linear response. Accordingly, Eq. 2.57 is a tensor equation in reality. For the second order term, this reads as

$$P_i(\omega_3) = 2\epsilon_0 \sum_{jk} \chi^{(2)}_{ijk}(\omega_3, \omega_1, \omega_2) E_j(\omega_1) E_k(\omega_2). \tag{2.58}$$

Thus, the interaction of field elements E_j and E_k give rise to a polarization P_i in the i axis. For the third order term, the χ tensor has order four and so forth for higher orders. Hence, the interaction in higher orders become a complex interaction of many fields.

It is often convenient to stick to a contracted notation where

$$d_{ijk} = \frac{1}{2} \chi^{(2)}_{ijk}. \tag{2.59}$$

Further, symmetry properties of the materials play a role if the material is lossless (which is always assumed in this theoretical treatment) and the dispersion of the susceptibility is weak. This is often the case in red or near-infrared wavelength regimes, since the resonant part of the spectrum lies around the band gap of the material in the blue or ultraviolet regions. The so-called Kleinman symmetry[65] states, in this case, that the enumeration variables j and k are interchangable, hence the χ tensor is symmetric in this quantities. Accordingly, the quantity from Eq. 2.59 is further contracted to d_{il} with the substitutions given in Tab. 2.1. If the factor is measured such that multiple matrix elements contribute to the emission an effective coefficient (d_{eff}) is given.

2.2.1 Anharmonic Oscillator Model

A simple treatment of the second-order non-linearity is by a simple anharmonic oscillator model, which attributes for the symmetry breaking in a material. The one dimensional anharmonic oscillator differential equation reads as

$$\frac{\partial^2 x}{\partial t^2} + 2\gamma\frac{\partial x}{\partial t} + \omega_0^2 x + ax^2 = -e\lambda E(t)/m. \tag{2.60}$$

Here, ω_0 is the resonance frequency, γ is the damping and a is a scaling factor for the anharmonic potential. The right hand side describes the driving by the electric field and x is the space coordinate. λ is a strength scaling factor and acts as a perturbative term in the equation. The potential of the restoring force equates to

$$V(x) = \frac{1}{2}m\omega_0^2 x^2 - max^2. \tag{2.61}$$

A modification of this potential allows for the treatment of centrosymmetric material, i.e.,

$$V(x) = \frac{1}{2}m\omega_0^2 x^2 - \frac{1}{4}mbx^4. \tag{2.62}$$

This yields a symmetric potential with interaction anharmonic bending b.

To solve Eq. 2.60 x is expanded in λ: $x = \lambda x^{(1)} + \lambda^2 x^{(2)} + \lambda^3 x^{(3)} + \ldots$. This leads to the equation system

$$\frac{\partial^2 x^{(1)}}{\partial t^2} + 2\gamma\frac{\partial x^{(1)}}{\partial t} + \omega_0^2 x^{(1)} = -eE(t)/m \tag{2.63}$$

$$\frac{\partial^2 x^{(2)}}{\partial t^2} + 2\gamma\frac{\partial x^{(2)}}{\partial t} + \omega_0^2 x^{(2)} + a\left(x^{(1)}\right)^2 = 0 \tag{2.64}$$

and so forth for higher orders in x. Therefore, the higher orders depend solely on the lower order contributions in the anharmonic potential. For the symmetric potential (Eq. 2.62) the equations odd and even in x become decoupled. The consequence of the decoupling will be analysed later.

The first-order solution of Eq. 2.63 yields

$$x^{(1)}(\omega_j) = -\frac{e}{m}\frac{E_j}{\omega_0^2 - \omega_j^2 - 2i\omega_j\gamma} \equiv -\frac{e}{m}\frac{E_j}{D(\omega_j)}. \tag{2.65}$$

Introducing this equation into Eq. 2.64 yields a possible second-order solution

$$x^{(2)}(\omega_1 + \omega_2) = \frac{-a(e/m)^2 E_1^2}{D(\omega_1 + \omega_2)D^2(\omega_1)}. \tag{2.66}$$

Here, not only the case $\omega_1 + \omega_2$ is possible but also the difference frequency or equal incident frequencies. For simplicity, only the SHG case will be studied here. However, the solutions of the electronic motion in a potential has to be transferred to an expression for the susceptibility. If one assumes that the anharmonic potential represents the potential of an atomic species in the material the polarization can be expressed as N times this contribution, hence

$$P^{(1)}(\omega_j) = \epsilon_0\chi^{(1)}(\omega_j)E(\omega_j) = -Nex^{(1)}(\omega_j), \tag{2.67}$$

which yields analogously for higher orders the susceptibilities

$$\chi^{(1)}(\omega_j) = \frac{Ne^2/m}{\epsilon_0 D(\omega_j)} \tag{2.68}$$

$$\chi^{(2)}(\omega_1+\omega_2,\omega_1,\omega_2) = \frac{N(e^3/m^2)a}{\epsilon_0 D(\omega_1+\omega_2)D(\omega_1)D(\omega_2)}. \tag{2.69}$$

Thus, it is obvious that an anharmonic potential gives rise to a second order non-linear response. Contrary, for the symmetric case of Eq. 2.62 the decoupling even and odd expansions of the equation system leads to a non-interaction between first and second order terms. Hence, for symmetric potentials there is no possibility to create an even non-linear response, i.e., SHG or fourth harmonic generation (or higher) are not possible in centrosymmetric materials as volume response. Although, virtually any material emits surface SHG, due to the inherent symmetry breaking of an interface (see Sec. 2.2.5).

Reviewing Eq. 2.68 and Eq. 2.69 shows that the second order susceptibility can be expressed in terms of the first order. Thus,

$$\chi^{(2)}(\omega_1+\omega_2,\omega_1,\omega_2) = \frac{\epsilon_0^2 ma}{N^2 e^3}\chi^{(1)}(\omega_1\omega_2)\chi^{(1)}(\omega_1)\chi^{(1)}(\omega_2). \tag{2.70}$$

If the prefactor is constant this leads to the Millers rule[66], which reads

$$\delta = \frac{\chi^{(2)}(\omega_1+\omega_2,\omega_1,\omega_2)}{\chi^{(1)}(\omega_1+\omega_2)\chi^{(1)}(\omega_1)\chi^{(1)}(\omega_2)}. \tag{2.71}$$

The constant δ is called the Millers delta and is measured for many materials. Accordingly, it is possible to predict the SHG or other second-order interactions by the linear dispersion of the material. However, it is stressed here that the Millers rule is a crude approximation from a simple anharmonic potential and often fails for real materials[67]. It should therefore be treated with caution if used in any experiment.

2.2.2 Sum-Frequency Generation

In this section, the derivation of sum-frequency generation, which is a second order contribution, will be treated. The general approach is by using the polarization driven wave equation (Eq. 2.5), where the electric field represents the field generated from the polarization. Accordingly, the polarization represents the interaction of the incident electric field. To account for linear and non-linear parts of the polarization the driving factor is split, such that $P = P^{(1)} + P^{\mathrm{NL}}$ represents the linear and non-linear parts, respectively. Further, monochromatic plane waves along the z direction and a lossless medium is assumed. Hence, the generated electric field and polarization read as (exemplary for the third vector component)

$$E_3(z,t) = A_3 \exp\left[i\left(k_3 z - \omega_3 t\right)\right] + c.c. \tag{2.72}$$

$$\begin{aligned} P_3(z,t) &= 4\epsilon_3 d_{\mathrm{eff}} A_1 A_2 \exp\left[i(k_1+k_2)z\right]\exp\left[-i\omega_3 t\right] + c.c. \\ &= P_3 \exp\left[-i\omega_3 t\right] + c.c. \end{aligned} \tag{2.73}$$

The complex conjugates can be omitted without changing the underlying physics. Introduction in the wave equation (Eq. 2.5) and rearranging leads to

$$\frac{\partial^2 A_3}{\partial z^2} + 2ik_3 A_3 z = -\frac{4d_{\mathrm{eff}}\omega_3^2}{c^2} A_1 A_2 \exp\left[i(k_1+k_2-k_3)z\right], \tag{2.74}$$

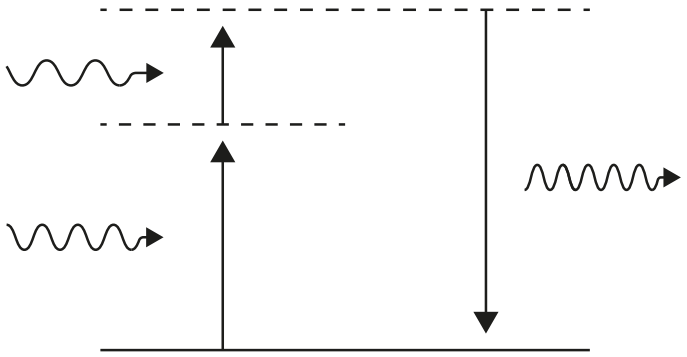

Figure 2.15: Schematic of sum-frequency generation. Dashed lines depict virtual levels and solid lines are electronic levels.

with the wave vector mismatch $\Delta k = k_1 + k_2 - k_3$. Typically, the second derivative of A_3 is much smaller than $k_3 \frac{\partial A_3}{\partial z}$, hence it can be dropped. This is known as the slowly varying amplitude approximation. This simplifies the equation to

$$\frac{\partial A_3}{\partial z} = \frac{i\omega_3}{2\epsilon_0 n_3 c} P_3 \exp\left[i\Delta k z\right] = \beta \exp\left[i\Delta k z\right]. \tag{2.75}$$

In the assumption of undepleted pump, i.e., P_3 is constant, the equation can be readily integrated for an interaction length L:

$$A_3(L) = \beta \int_0^L \exp\left(i\Delta k z\right) dz = \beta \frac{\exp\left(i\Delta k z\right) - 1}{i\Delta k} \tag{2.76}$$

With this result, the emitted intensity given by $I_i = 2n_i\epsilon_0 c|A_i|^2$ equates to

$$I_3 = 2n_3\epsilon_0 c\beta^2 L^2 \mathrm{sinc}^2\left(\Delta k L/2\right). \tag{2.77}$$

2.2.3 Phase Matching

It is apparent in Eq. 2.77 that the emitted intensity is crucially dependent on the wave vector mismatch Δk. Figure 2.16 shows the change of intensity related to the wave vector mismatch for a constant L. A perfect matching, thus maximum output intensity is achieved by the phase matching condition $\Delta k = 0$. In this case, the total intensity scales with L^2, since the generated and incident wave stay in phase leading to constructively enhancing of the signal. Contrary, the generated wave gets out of phase with the driving field if there is a mismatch in the wave vectors of the generated waves ($\Delta k \neq 0$). This leads to back conversion from the non-linear field to the fundamental wave, thus the light intensity changes periodically throughout the interaction region (Fig. 2.17). Since the prefactor $\Delta k/2$ in the sinc function of Eq. 2.77 determines the periodicity of the oscillation it is convenient to define it as the coherent length of non-linear interaction:

$$L_{\mathrm{coh}} = \frac{2}{\Delta k}. \tag{2.78}$$

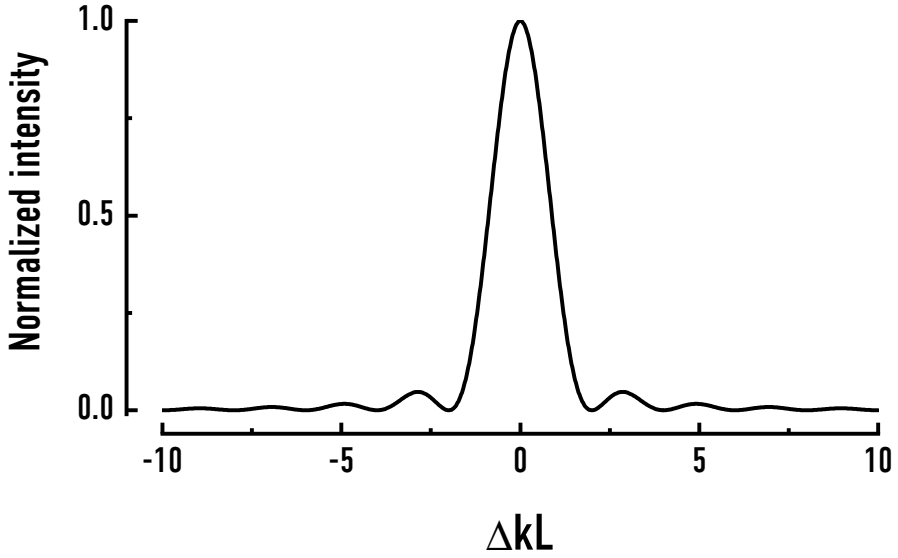

Figure 2.16: SHG intensity in dependence of the wave vector mismatch Δk.

However, phase matching is not possible for many materials. To illustrate why this is the case it is convenient to rewrite the phase matching condition in terms of the refractive indices, yielding

$$n_1\omega_1 + n_2\omega_2 = n_3\omega_3. \tag{2.79}$$

For SHG ($\omega_1 = \omega_2 = \omega_3/2$) the equation breaks down to $n(\omega) = n(2\omega)$. Typically, the dispersion of a material is a monotonically increasing function to higher refractive for higher energies. This is often described by the Sellmeier formula[68], but it is only an approximation far away from the resonance taking place in the blue spectral region. For even higher energies the dispersion of the material will lower rapidly, theoretically allowing for phase matching conditions in this region. The resonance is due to the band gap of the material, thus if the condition is chosen such that the SHG energy is above this resonance, it will be absorbed in the material. Hence, phase matching is not achievable under these circumstances.

Yet, it is still possible to generate optical harmonics with high efficiency. In essence, this can be done in two ways: critical and non-critical phase matching. Both of the methods require a birefringent material, i.e., the material shows different refractive indices depending on the light polarization. Luckily, this is the case for many materials exhibiting non-linear properties due to their asymmetric nature, which often gives rise to birefringence, too. The refractive indices of fundamental and SHG are then able to match if the material is rotated and tilted to match the criteria. This angle-tuning matching procedure is often termed critical phase matching. It is critical in the sense that the angles have to be oriented with great precision. Additionally, temperature plays a major role, since it affects the refractive indices of the material. Thus, for critical matching conditions, the environmental influence has to be very controlled. The angle-based condition for phase matching[69] is

$$\frac{1}{n_e(\Theta)^2} = \frac{\sin^2(\Theta)}{n_e^2} + \frac{\cos^2(\Theta)}{n_o^2}, \tag{2.80}$$

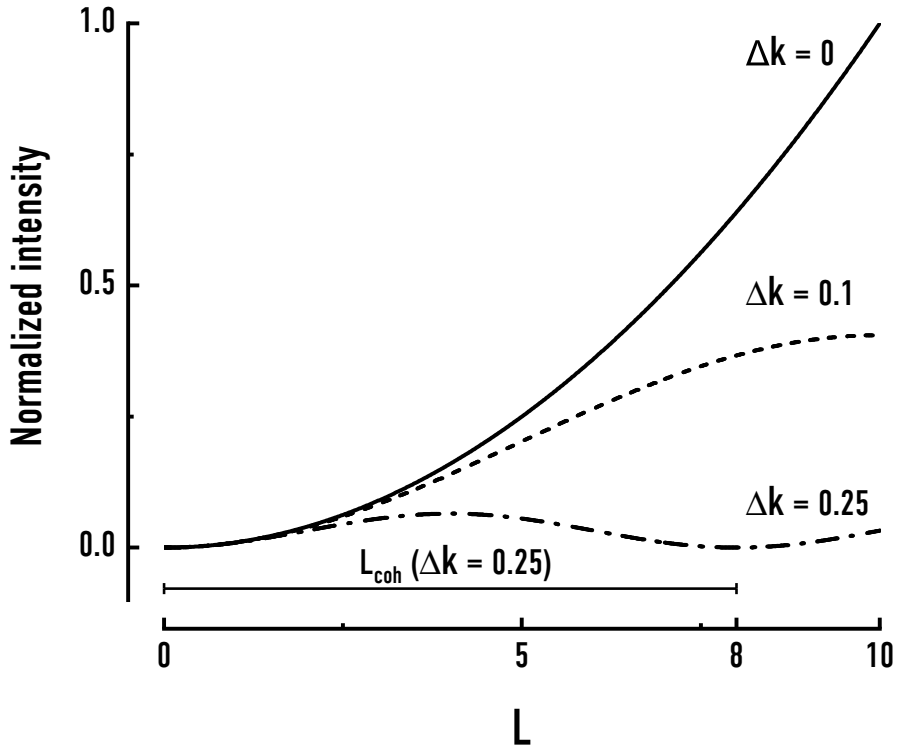

Figure 2.17: SHG intensity along an interaction thickness L for different phase matching factors (Δk). The line below depicts the coherence length for a phase mismatch of $\Delta k = 0.25$.

with the angle of incidence Θ and ordinary n_o and extraordinary n_e refractive indices, respectively. Moreover, this leads the non-normal angle of incident to a spatial walk-off due to a mismatch between the Poynting vector and the wave vector of the wave[70]. This is only the case for extraordinary rays, leading to a mismatch between the fundamental and harmonic generation, thus limiting the interaction region of the two waves. Additionally, for ultra-short pulses also temporal walk-off has to be accounted for which is a generally independent phenomenon in harmonic generation. As a consequence of the energy time uncertainty (Eq. 2.20), the bandwidth of a pulse is broader than its cw counterpart. Each of the frequencies contained in the pulse see a different refractive index in the material, thus they travel at a different speed through the material. This leads to pulse broadening in general, which is quantized by the group velocity dispersion (GVD) around the pulses central frequency ω_0:

$$\mathrm{GVD}(\omega_0) = \frac{\partial}{\partial \omega}\left(\frac{1}{v_g(\omega)}\right)_{\omega=\omega_0}. \tag{2.81}$$

$v_g(\omega)$ is the group velocity of the material. Certain materials exhibit negative GVD, hence pulse compression occurs. In the regime of harmonic generation, this effect appears as well: the harmonic travels at another speed than the fundamental. This leads to a walk-off between the two waves, while the induced polarization still produces harmonic waves. Accordingly, the generated pulse broadens strongly, while the peak shifts away from the driving wave. The phenomenon is quantized by the group velocity mismatch, i.e., $\mathrm{GVM} = v_{g1}^{-1} - v_{g2}^{-1}$. Rarely, the group velocity mismatch is negligible for ultra-short

pulses below the ps regime. Thus, thin crystals in combination with strong focusing is used for the generation of ultra-short harmonic pulses.

In contrast to angle tuning, the non-critical approach is to use temperature tuning to change the refractive indices of a material. It is only possible for materials with a strong influence of temperature[71,72] and is limited by the temperature intervals applicable. Technically, temperature gradients in and around the crystal can lead to disturbances of the harmonic generation. This technique is often employed in commercial systems using non-linear effects due to its better reproducibility and resilience to disturbances.

Furthermore, the type of the phase matching is further divided into two cases, depending on the polarizations of the incident beams relative to each other[73,74]. Collinear polarization is called type-I phase matching and type-II for orthogonal polarizations of the incident waves. The emitted harmonic polarization depends on the crystal properties, e.g., if its positive ($n_e > n_0$) or negative ($n_e < n_0$) uniaxial (two optical axes) or biaxial (three optical axis). Generally, the conditions can be derived from the tensor components of χ_{ijk}. An example for the elements of such tensors for the mm2 (orthorombic) and 32 (trigonal) crystal class will be given in Ch. 8.

Notably, even for circumstances where the above criteria are not able to achieve phase matching, it is possible to efficiently convert light. The basic idea is to alternate the properties throughout the interaction length. Armstrong et al.[75] proposed to rotate thin slices of crystals by 180° to achieve the condition for the so called quasi-phase matching[75]. However, the slices have to be too thin to be of practical use to achieve good efficiencies, but Yamada et al. showed the possibility of the process by an alternating static electric field to switch ferroelectric domains. The intensity increase in the interaction region is then a modulated parabola, leading to a slightly lower total intensity than for perfect phase matching. Nevertheless, good efficiencies are possible with different approaches to this idea[77].

The angle dependence is employed in a measurement technique for SHG. By rotating a sample one obtains an angle dependent oscillatory intensity function. These are Maker fringes first observed by Maker et al.[78]. In the wave picture, the oscillatory and envelope parts are known, allowing for measurements with less statistical error. The relevant equations are outlined in Sec. 9.1 as correction terms for the measurement.

2.2.4 Second-Harmonic Generation

In addition to the derivation of sum-frequency generation outlined in Sec. 2.2.2, which contains the SHG in the case $\omega_1 = \omega_2$, an outline of a solution with depleted pump intensity will be given here. This is necessary, since for short pulses and good experimental conditions the efficiency of SHG can reach several tens of percent of the fundamental intensity.

Notably, the total intensity of the three interacting waves $I = I_1 + I_2 + I_3$ is still conserved. Furthermore, the spatial photons per unit area and time obey the Manley-Rowe relations[79,80]:

$$\frac{\partial}{\partial z}\left(\frac{I_1}{\omega_1}\right) = \frac{\partial}{\partial z}\left(\frac{I_2}{\omega_2}\right) = -\frac{\partial}{\partial z}\left(\frac{I_3}{\omega_3}\right). \tag{2.82}$$

This means that the spatial change of intensity in the driving waves leads to the same intensity change of the generated wave.

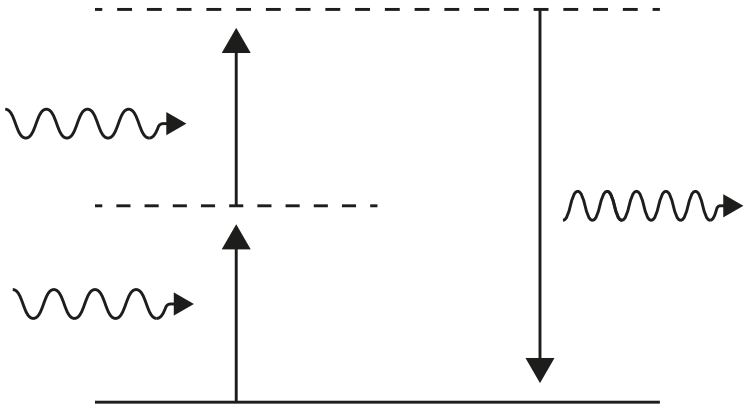

Figure 2.18: Schematic of second harmonic generation. Dashed (solid) lines depict virtual (real) levels.

With these relations it is possible to solve for the SHG intensity with a depleted pump as will be shown here schematically, only. For a full treatment, the reader is referred to Armstrong et al.[75] or Boyd[69]. In the following, the index one and two will refer to the fundamental and second harmonic wave, respectively. First, the amplitudes of the waves are divided into their complex amplitude and phase:

$$A_i = \sqrt{\frac{I}{2n_i\epsilon_0 c}} u_i \exp\left(i\phi_1\right). \tag{2.83}$$

According to the Manley-Rowe relations, it follows that $u_1^2(z) + u_2^2(z) = 1$. Introducing each of the monochromatic plane waves with amplitudes from Eq. 2.83 into the wave equation (Eq. 2.5) leads to three coupled differential equations:

$$\frac{\partial u_1}{\partial z_n} = u_1 u_2 \sin\Theta \tag{2.84}$$

$$\frac{\partial u_2}{\partial z_n} = -u_1^2 \sin\Theta \tag{2.85}$$

$$\frac{\partial \Theta}{\partial z_n} = \Delta s + \frac{\cos\Theta}{\sin\Theta}\frac{\partial}{\partial z_n} \ln\left(u_1^2 u_2\right) \tag{2.86}$$

with the reduced space coordinate

$$z_n = \sqrt{\frac{\epsilon_0 c I}{2n_1^2 n_2}}\frac{2\omega_1 d_{\text{eff}}}{c} z \equiv z/l \tag{2.87}$$

and phase relation $\Theta = 2\phi_1 - \phi_2 + \Delta k z$. $\Delta s = \Delta k$ is the wave vector mismatch. For perfect matching conditions ($\Delta s = 0$) Eq. 2.85 can be integrated and it can be shown that the quantity $\Gamma = u_1^2 u_2 \cos\Theta$ is conserved[75]. It follows that $\Gamma = 0$, when assuming that the incident second-harmonic field is zero at the boundary of the interaction region ($u_2 =$

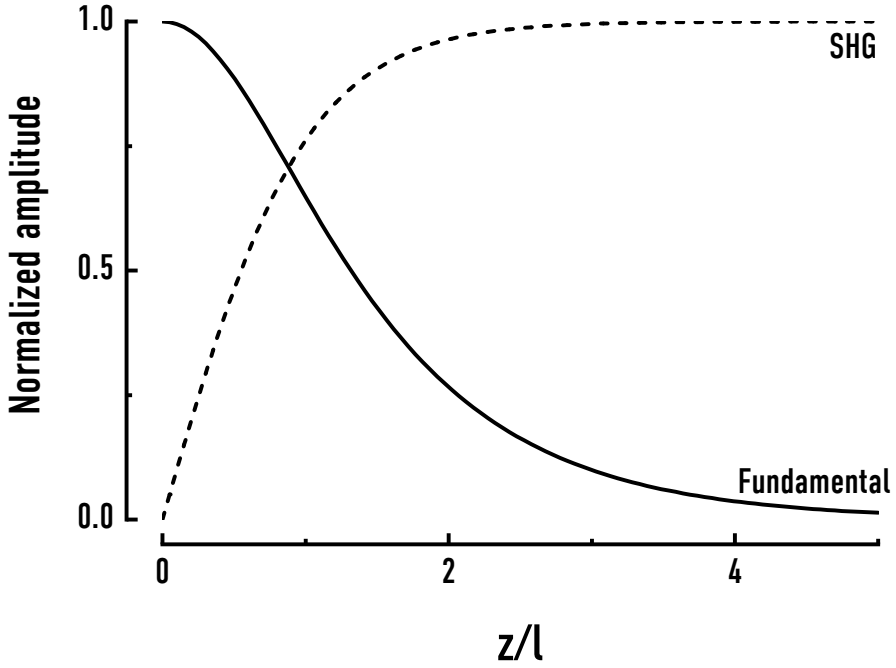

Figure 2.19: Normalized SHG (dashed) and fundamental (solid) amplitude in dependence of the normalized interaction length z/l.

0). Accordingly, cos Θ has to be zero throughout the crystal to keep the conservation law. If we arbitrarily choose sin $\Theta = -1$ Eq. 2.84 and Eq. 2.85 can be solved directly, yielding

$$u_1(z_n) = \text{sech}(z_n) \tag{2.88}$$

$$u_2(z_n) = \tanh(z_n), \tag{2.89}$$

for the intensity increase along the interaction region. Figure 2.19 shows that the increase of SHG is now limited by the availability of pump intensity. Further, it is obvious that the complete incident power can be possibly converted into SHG power under perfect circumstances. In reality, mainly spatial and temporal walk-off effects and decoherence will lead to a lower output efficiency. Notably, modulation between fundamental and harmonic wave shows up if the SHG intensity ($u_2 \neq 0$) is not zero at the input or the two waves are out of phase[75]. Moreover, for $\Delta s \neq 0$ Eq. 2.84 to Eq. 2.86 can be solved, too. This leads to the oscillatory behaviour already known from Sec. 2.2.2. The major difference is that envelope of the oscillations now follow the tanh function from Eq. 2.89 (Fig. 2.20).

However, for focused Gaussian beams there a still some peculiarities: the π phase jump during the focus transition[81] rises complex interaction patterns for not perfectly matched waves. Even in the phase-matched case, the generated harmonic shows a phase jump equal to the order of the non-linearity times π. Therefore, the waves dephase across the focus. Since the field strengths in the focus region are the biggest, this effect is very pronounced. Accordingly, the wave vector mismatch has to be slightly detuned to a higher value to account for the phase jump in the focus to restore the full output efficiency[82]. Further, the harmonic beam shows a non-symmetric pattern and fringe structure for birefringent materials[83]. The most important consequence for

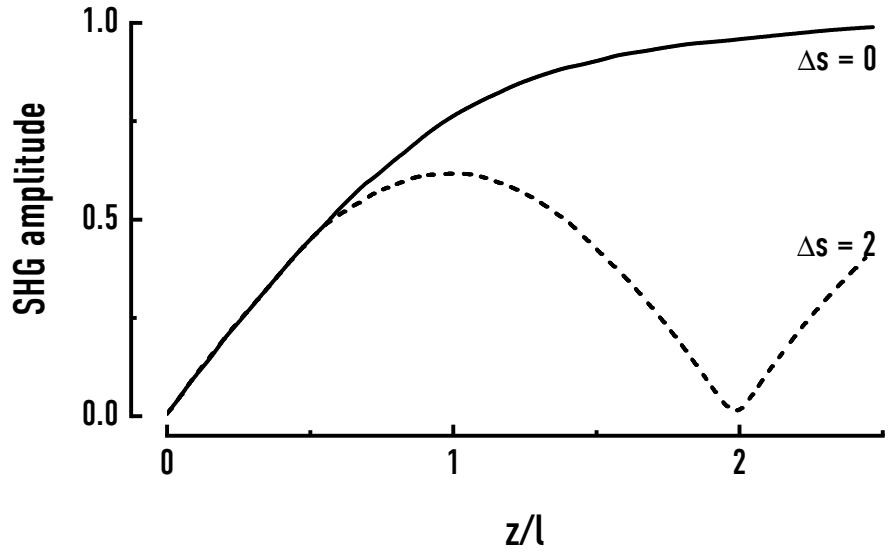

Figure 2.20: Normalized SHG amplitude for two different wave vector mismatches in dependence of the normalized interaction length (z/l).

measurements of SHG is the replacement of the effective interaction region, which is dependent on the Rayleigh length of the Gaussian beam[83]. For non-focused beams the interaction region was simply given by the length of the crystal. This has major impact on the generation of light in the non-matched case, since the oscillations inside the Rayleigh length are more pronounced in the output intensity than anywhere else in the crystal.

2.2.5 Interfaces

As already stated previously, even-order non-linear effects are created mainly from asymmetries along the polarization of the electric field. Despite the fact that this creates harmonics or mixing of the incident light for non-centrosymmetric bulk materials, it implies that an interface emits photons of a different energy, too. This implication simply follows from the symmetry breaking inherent to an interface. Since the coefficients for higher orders are relatively weak for most materials, only SHG will be treated here. In essence, surface SHG follows from the continuity of the tangential component of the electric and magnetic fields at the interface. In conjunction with the wave equation (Eq. 2.5) the surface SHG intensity can be calculated[84]. Similarly to simple reflection and transmission, the surface harmonic generation is dependent on the polarization relative to the plane of incidence. The harmonic light is generated in a thin slab of thickness $l = \lambda/4\pi$, for a material exhibiting bulk non-linearity's. Further, the intensity vanishes for phase matching conditions in the surface slab. If the slab is thin compared to the wavelength, the transverse electric field emitted from the surface equates to

$$E^T = E^R = \frac{i4\pi P^{NL} d}{n_T cos\Theta_T + n_R \cos\Theta_R}, \tag{2.90}$$

for transmission (T) and reflection (R), respectively. Any other case of incidence and different slab thickness can be treated as well. Since the formulas are rather lengthy the

reader is referred to Bloembergen and Pershan[84] for a full treatment of the conditions. A more detailed derivation of surface emission for a particular polarization will be given in Sec. 9.1 in the correction terms for the measurement. The wave amplitudes in this cases can be approximated as

$$A^R \approx \frac{P^{NL}}{4\epsilon_0 c^2 \epsilon_r} \tag{2.91}$$

$$A^T \approx \pi A^R \left(1 - 2ik_T(\omega_s)z\right). \tag{2.92}$$

Contrary, in a centrosymmetric material the emitted light depends critically on the surface properties and molecular orientations of the material. Thus, a rigorous theoretical treatment is complicated, but typically the emitted light amplitude is three orders of magnitude weaker compared to a non-linear material.

2.2.6 Supercontinuum

In contrast to harmonic generation and mixing processes there exists the possibility of white-light generation of a material through non-linear interactions. The process cannot be understood in terms of a simple picture, since many processes are involved in the generation of the light and the underlying contributions are not often clear. Therefore, numerical simulations are used to model such behaviours[24]. This mechanism is employed in PCFs[85], where certain asymmetries are introduced and simulated to broaden the fundamental pulse to an extent of two or three octaves in the visible and near-infrared spectrum. Here, some basic principles and the foundation of these processes will be given. Typically, supercontinuum generation takes only place for light pulses, since they deliver the necessary spectral width for the processes involved. The simplest effect the incident pulse undergoes is its modification through the Kerr effect[86] or intensity dependent refractive index, which reads

$$n = n_0 + n_2 I(t), \tag{2.93}$$

where the non-linear refractive index is related to the third order susceptibility $n_2 = (2\pi/n_0)^2\chi^3$. The effect has two major consequences: a focusing of intense light and self phase modulation (SPM) of a short laser pulse. The first process is known from ultra-short laser systems, such as the Ti:sapphire laser[87], where the focusing of the pulsed light is used to favor it over the cw light, thus enabling continues pulsing of the Ti:sapphire laser[88]. According to Eq. 2.93 the non-linear phase change is given as[89,90]

$$\phi(t) = \omega_0/c n_2 I(T) L, \tag{2.94}$$

for a material of thickness L and pulse central frequency ω_0. Since the phase change induces a temporal change of the incident pulse this leads to a symmetric broadening of the pulse and a frequency deviation to a maximum value of

$$\Delta\omega = \omega_0/c n_2 L I_0/\tau, \tag{2.95}$$

where I_0 and τ are the intensity and width of the pulse. Moreover, the pulse is affected by a second mechanism leading to a broadening of the pulse, the GVD, i.e., the change of dispersion in the group velocity. However, Kerr lensing and GVD effects are not significant enough to generate white-light of multiple octaves bandwidth. For a further

broadening mainly Raman, self-steepening, and four-wave mixing effects take place. Raman scattering typically leads to a broadening of the pulse around the center frequency, as the bandwidth further increases the scattering has more cross-sections, thus the effect gets stronger, the broader the pulse. Self-steepening occurs due to temporal intensity changes of the pulse, hence, the pulse sees different refractive indices if the Kerr effect is strong enough. This leads to a slower propagation of the peak pulse and thus gets shifted to the temporal tail of the pulse, introducing spectral asymmetry. Four-wave mixing is a non-linear third-order process converting two (or three) waves into two (one) waves of different frequency. Hence, for a pulse with a great bandwidth four-wave mixing can lead to strong transformation of the light by mixing of its inherent frequencies. In essence, a working white-light emitter counter-balances each of these non-linear effects and the dispersion of the material, leading to a form-stable wave: a soliton[91]. A soliton itself can undergo fission which further broadens the pulse.

In summary, white-light generation is a complex process involving multiple optical non-linearity's, which counterbalance themselves to generate a stable travelling pulse with a very high bandwidth.

2.2.7 Molecular Materials

In this section, the physical properties of molecular materials and the role of molecular materials in non-linear optics will be discussed. In contrast to the inorganic materials presented in the previous sections the building blocks in organic system are often larger molecules incorporating many atoms. The typical inorganic semiconductor crystals discussed above feature only one to four elements arranged in a periodic fashion. Therefore, the unit cells remain small and the reciprocal space and the band structure is the framework in which the structures are described. For molecules, commonly descriptions in real space are used and the bonding of the atomic orbitals are investigated. This is possible due to the amount of around a tens of atoms in each molecule and longer-range coupling effects are commonly neglected. Therefore, a theoretical description of such a molecule as a whole system becomes possible in real space. Notably, such description would not be possible in an inorganic crystal due to the sheer amount of atomic bindings of the 10^{22} atoms present in a typical crystal.

Taking into account the overall crystalline structures of molecules leads to a very low dispersion in the band structure, as the molecules are van-der-Waals bound to each other, i.e. the intermolecular binding is weak. This means that the single molecular response is commonly dominating in the light interaction with such molecules. In the next approximation, coupling of two molecules in a unit cell may be taken into account, leading to, e.g., the Davydov-splitting of excitons[92]. In the following, the different bond types of molecules will be highlighted and their optical response will be deduced from this binding properties.

The embedding framework is the molecular orbit theory, which explains the arrangement of orbital hybridization in energy. The starting point is the linear combination of atomic orbitals (LCAO), which in essence states that the atomic orbitals can be linearly combined. A simple example of such a linear combination is the bonding of two hydrogen atoms forming a H_2^+ molecule. Regarding the 1s orbitals, they can combine in two different schemes (Fig. 2.21): in an antibonding and in a bonding fashion. The antibonding case describes the bonding of the wave functions having a different sign.

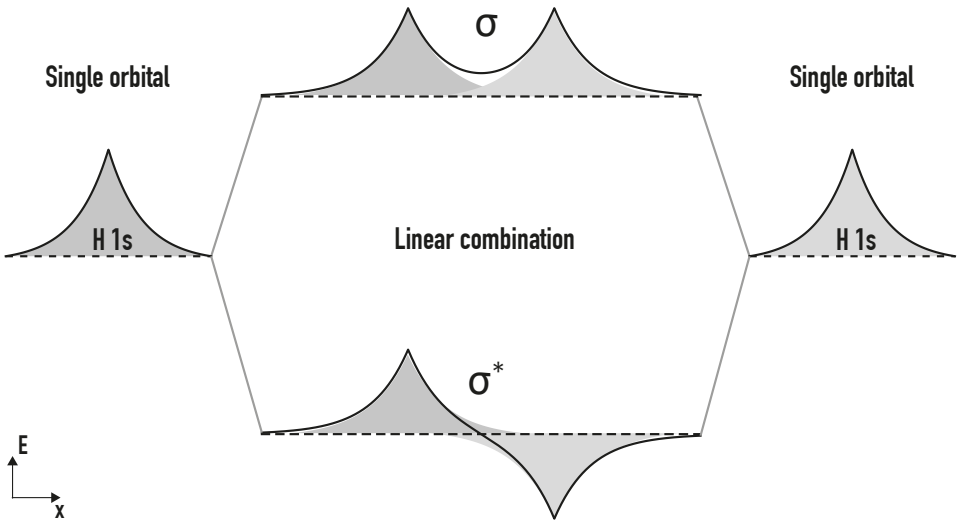

Figure 2.21: Linear combination of H 1s states forming new bonding and antibonding states. Left and right sides show the single atomic orbital and the levels in the middle are the linearly combined states with their respective energy shifts.

Hence, the probability density right between the nuclei is zero. This bonding type is also known as a σ^*-bond. The bonding case termed σ-bond refers to an orbital overlap where both wave functions have identical signs. Thus, yielding a non-vanishing probability density between the nuclei. Since the energy is related to the electronic overlap the bonding levels shift with respect to the original atomic levels. The greater overlap of electron density in the σ-bond leads to a lowering in energy, whereas the antibonding leads to an energy rise. This is often denoted in a graphical fashion, where the genuine atomic levels are drawn on the left and ride sides of the picture and the bonding orbitals in the middle. To highlight the contributing mixing orbitals the levels are connected by lines, hence the shift is directly visible. Figure 2.21 depicts the respective energy shift due to orbital mixing in the H_2^+ molecule. Additionally, it shows the linear combination of the wave functions, which is typically left out for clarity, in such molecular orbit diagrams.

Generally, the atoms constituting in the formation of orbitals do not only have s-orbitals contributing to the orbital overlapping. Therefore, p-orbital mixing plays a major role in the formation of molecular bonds. Similar to the s-state mixing forming σ-bonds the p-states mix as well in bonding and antibonding types. Here, bonding and antibonding again refers to constructive or destructive overlap of the wave functions. In accordance with the * notation, they are then referred to as π and π^* bond, respectively. Moreover, the s and p-orbitals can also linearly combined, leading to a hybrid orbital between s and p properties. This can occur in three different stages: sp, sp^2 and sp^3 hybridization. The notation simply denotes the amount of p orbitals with one s orbital, i.e., sp^i describes the mixing of a s orbital with i p orbitals. This gives rise to $i+1$ hybridized levels and $3-i$ remaining pure p levels. The hybridization generally lowers the energy with respect to the remaining p orbitals, thus intermediate energy levels between the s and the p orbitals will be created from the process. The sp^2 and sp^3 hybridization alters the angle of the orbitals, i.e., the sp^2 bonding has a planar $120\,^\circ$ angle between the p parts of the

mixed orbitals. The sp^3 has a tetrahedral symmetry with an angle of $109.5\,^\circ$ between the p parts. Therefore, sp^3 hybridization gives rise to the zinc-blende structures common in many inorganic crystals. In molecular structures it is often termed σ bond as well, as it includes contributions from s orbitals.

Carbon-carbon bonds are very good examples to review the influence of sp mixing carbon. Carbon is available in each of the different configurations, i.e., acetylen (C_2H_2), ethylene (C_2H) and ethane (C_2H_6) show sp, sp^2 and sp^3 configurations, respectively. Besides, for carbon in a solid state form the differences are very interesting: due to the planar structure of sp^2 mixing, the carbon forms hexagonal rings (known as *honeycomb* structure) and is arranged as a sheet structure in graphite, or, in case of a single monolayer, graphene. In the case of solids, sp^3 hybridization carbon forms a diamond structure, which is similar to the zinc-blende structure. Graphene, graphite, and diamond show very different and unique material properties, albeit they all consist of carbon atoms. This shows the major importance of the sp mixing for macroscopic properties of solids and molecules. Notably, the hexagonal structure of carbon exhibits a further difference from simple π, σ or sp^2-bonding: the remaining p orbitals of the carbons are normal to the plane of the sp^2 bonding of the carbons and therefore do π bonding as well. Yet, π bonding of two neighbouring p orbitals would yield an alternating of bonding and no bonding between the orbitals, which are equidistant. This does, of course, not happen in reality, because all of the wave functions have to be taken into account performing LCAO. Therefore, all of the six p orbitals mix all together, forming an aromatic ring, i.e., a planar delocalized donut shaped wave function across the complete hexagonal ring. In graphene this leads to the unique electrical properties, since the aromatic rings are connected throughout the material creating a two dimensional wave function across the whole sheet. Generally, for any cyclic ring system an aromatic ring forms if $4n + 2\,\pi$ electrons are present, which is known as the *Hückel rule*[93].

The typical energy differences between π and σ bonds is crucial for interactions of light with molecules. In most cases, the gap between σ-σ^* bonds is greater than $6\,eV$. The π-bonds are more strongly polarizable because their electron density is, on average, farther away from the nuclei and their electron wave function is zero at the nuclei. Thus, their general binding is weaker. As a consequence, the π-π^* gap is much smaller, usually in the regime of $1 - 4\,eV$. Generally, a similarity to the band gap of a semiconductors exits for any mixing of atomic orbitals. The specific orbital up to which all states are fully filled in a neutral molecule is termed highest occupied molecular orbital (HOMO). The first orbital with the lowest energy and no electronic population is the lowest unoccupied molecular orbital (LUMO). The energy difference between these two orbitals (the HOMO-LUMO gap) determines the optical response of a molecule. In a molecular solid, excitonic effects exists similar to the effects at the band gap of a semiconductor.

Further, the molecular orbitals give rise to absorption and emission peaks corresponding to the respective energy. Similar to inorganic crystalline structures, the energy of the level is lowered by the Coulomb force between electrons and holes, thus excitonic features are observable in molecular solids. As a consequence of the confinement to virtually a single molecule the exciton Bohr radius is rather small in comparison, resulting in a bigger exciton binding energy. In Alq_3, which is the material for blue emitting organic LEDs, the binding energy of the excitons is $1.4\,eV$[94], which is huge compared to the $5\,meV$ binding energy in GaAs. The excitons in molecular bindings are called Frenkel excitons[45] to theoretically divide them from the Mott-Wannier excitons in inorganic semi-

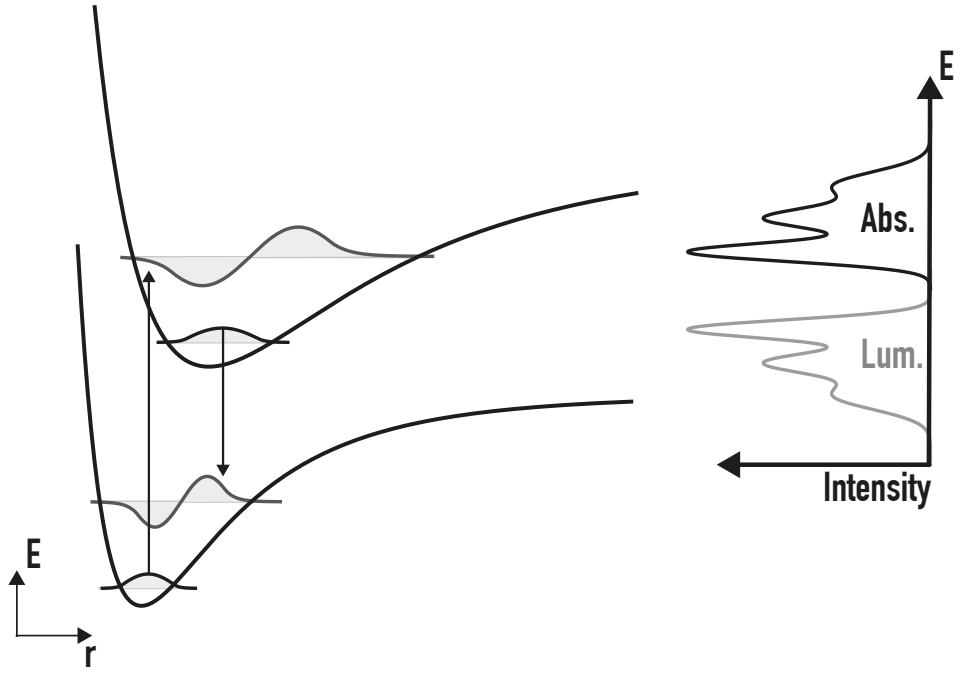

Figure 2.22: Schematic of the Franck-Condon princple for two electronic states (black curves). The wave functions inside the potentials are the vibronic levels in the respective electronic state. The arrows indicate the optical transition between these states. The inset on the right side depicts the luminescence (grey) and absorption (intensity) arising from the wave function overlap.

conductors. However, additional features are observed in experiments due to vibrational modes of the molecular coupling to the electronic excitations. The transition probability defined by the wave function overlap from the electronic ground state into a higher vibrational state in the first excited electronic state may be higher, as the nuclear motion is much slower than the electronic motion. This model is known as the Franck-Condon principle[95,96] and is similar to the Born-Oppenheimer approximation, where the different time scales of electron and nucleus motion are utilized. Figure 2.22 shows a sketch of the vibrational levels of two electronic states. Vertical transitions show the absorption or emission of photons into the corresponding vibrational levels, followed by relaxation into the vibrational ground state (i.e., motion of the nuclei). Since the wave-function overlap from the ground state to states with higher vibrational levels is higher, the transition dipole moment is larger, thus the absorption is stronger for higher vibronic energies. This leads to the typical features observed in the absorption and emission of molecules (inset in Fig. 2.22) and to a Stokes shift between absorption and emission maxima.

Molecules often exhibit non-linear optical properties as a consequence of the asymmetric shape of hybridized orbitals. This can be easily understood in terms of the bond-charge model[97]. In this model, the electron is approximated as a point charge in an electronic orbital. For example, it could be right in between two nuclei. This electron is driven by an applied external electric field, leading to a emission from its acceleration and deceleration. If the field is polarized perpendicular to the main axis of a p-orbital the electron is driven in an anharmonic potential, thus leading to non-linear emission (see Sec. 2.2.1 for a discussion of non-linear emission from an anharmonic oscillator).

Furthermore, higher harmonics are generated for light parallel to its major axis if the potential has an asymmetric shape (e.g., sp-hybridized orbitals). The conversion efficiencies depend on the polarizability of the orbitals, which can be calculated from the electron probability density. Yet, each molecule features more than one orbital and spectroscopy is commonly performed on ensembles of many molecules in crystalline or amorphous form. Therefore, the contributions of each of the orbitals have to be summed up to calculate a non-linear coefficient. This enables an exact calculation of many non-linear compounds and crystals, such as KDP or $LiNbO_3$[98]. Further interaction of the harmonic light can create complex emission spectra, i.e., through four-wave mixing processes or scattering which would lead to further creation of sideband harmonics. As a consequence, such calculations are usually numerically expensive, but the model still provides a vivid picture of the underlying process.

3 | Heterostructures

The term heterostructure generally describes a sample with at least two different materials. Each of the constituents can either be an elemental or a compound semiconductor. In most cases, heterostructures are aimed to have a rather abrupt interface between the different layers. Although, some devices are especially made with a continuous or enhanced interface between them to reach certain properties. Generally, the physical behaviour of heterostructures are strongly altered compared to bulk materials. This mostly affects the recombination rates, carrier mobility or gives rise to new behaviour, such as the quantum Hall effect. Moreover, certain devices are only possible through the possibility of heterostructural growth. This includes several types of transistors, pn-junctions, LEDs or solid state lasers. Therefore, the technological advance of growing these structures is of vast importance to today's technological culture. To enhance recombination rates, one aims to enrich electrons and holes in a spatially narrow structure and, therefore, enhance their wave function overlap and thus the transition dipole moment. Straight-forwardly, one can think of a simple quantum well structure, i.e., a rectangular potential drop; this has been studied in great detail in theory. The theoretical derivation (known as particle-in-a-box model) is found in any textbook on the basics on quantum mechanics[26,37,39,99]. Nevertheless, it is briefly outlined here as it is the basis for most discussions in this work.

The formula

$$V(x) = V_0 \left[\Theta(x-d) - \Theta(x)\right] \tag{3.1}$$

describes a simple one dimensional quantum well potential with the Heavyside function Θ and potential depth V_0 and width d. Introducing the potential into the Schrödinger equation yields the energy levels and the wave functions inside the well. For an infinite well depth $V_0 \to \infty$, the problem is analytically solvable. This leads to

$$E_n = \frac{\hbar^2 \pi^2}{2m^* d^2} n^2, \tag{3.2}$$

the energy levels of the well. The wave functions are simple sinusoidal standing waves with the closed boundary conditions. For a finite barrier height, the solution of the Schrödinger equation leads to a transcendental equation which can be solved numerically or graphically. It leads to sinusoidal wave functions, which impinge into the barrier with an exponential decay (Fig. 3.1). The lower the well potential, the bigger the impingent region. This allows for tunneling for multiple well structures with narrow barriers in between. Such models are known as coupled quantum wells or superlattices, i.e., it can be described by the Kronig-Penny model presented in Sec. 2.1.1. Adapting this quantum well idea to a real device, the above considerations would nicely reflect the behaviour of a conduction band of a thin material layer in between two barrier layers. The confinement in such structures is one dimensional, along the growth direction of the structure and the remaining two dimensions are large enough not to show confinement effects. This leads to an in-plane dispersion of the carriers, since they are able to move inside this layer freely. Although, regarding the z direction, there would not only be an offset in the conduction band, the confinement effects on the valence band has to be considered.

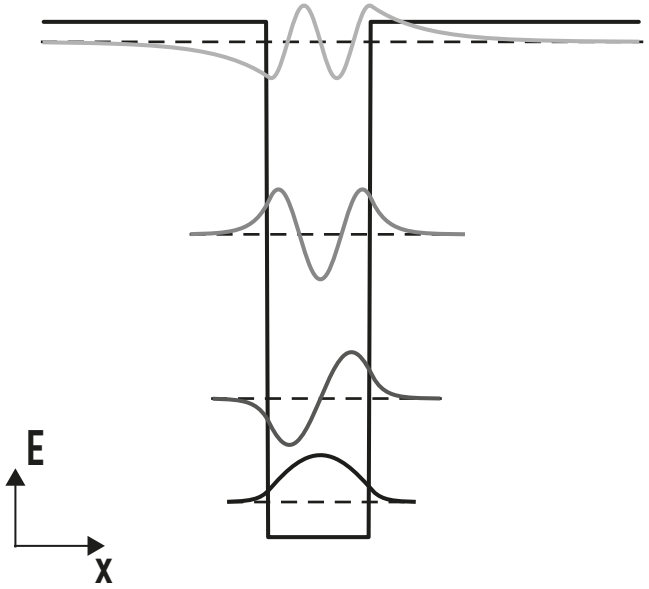

Figure 3.1: Electronic levels (dashed lines) and wave functions (curves on dashed lines) of an electron confined in a rectangular potential.

However, it is obvious from Eq. 3.2 that the energy levels scale inversely with the effective mass. Therefore, the quantization energies of heavy- and light-holes are different, lifting their degeneracy. Since the light hole is stronger affected by the shift the effect leads to band crossing of the in-plane dispersion. This yields a complex behaviour and a mass reversal between the two hole bands (Fig. 3.2). The hh band flattens, lowering its effective mass below that of the lh, which gets steeper through the mixing repulsion.

Obviously, already this straight-forward example shows the strong effects of confinement on the band structure of a material, leading to complex phenomena and new physical behaviour.

3.1 Growth

The prerequisite for a successful growth of a layered system is a suitable substrate. Such substrates are mostly grown by the Czochralski method. In the method, a seed crystal is used to grow a bigger single-crystal or ingot. Although the process is seemingly straight forward, caution has to be taken to produce a crystal with a low amount of defects. This is mostly controlled by extrinsic parameters, such as temperature, pulling rate or rotation speed. The width and length of the single crystal are controlled with this parameters as well, e.g., for modern silicon wafer production, ingots with a diameter of up to $300mm$ and a length of $2m$ are produced. The production of flat substrates from these ingots, again, seems straight forward. However, an elaborate process is necessary to determine the crystal orientation and to produce flat surfaces along the crystallographic axis. Flatness and accuracy of the cut is the basis for successful growth

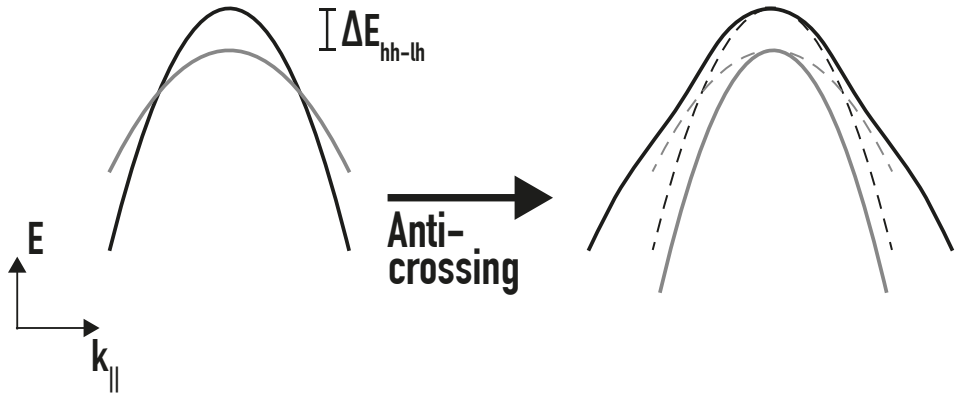

Figure 3.2: Mass reversal and anti-crossing of two valence bands due to different shifts under confinement. The left side shows genuine shifted bands only and the right side their change due to anti-crossing.

of layered structures. Often, to counterbalance roughness of substrates, a buffer layer is grown at a first layer on top to flatten the surface further.

Several techniques exist to actually grow a layer on top of a substrate or other layers. The growth can either happen on the same material (homoepitaxy) or on another material (heteroepitaxy). Generally, homo- and heteroeptiactic phases are cycled during the growth to produce materials of appropriate thicknesses and compositions. The first and most simple idea of such layer growth would be to simply accelerate atoms of different atomic species onto a heated substrate to let them bind on the surface and slowly grow a crystal. This technique is called molecular beam epitaxy (MBE) and is a powerful tool for the growth of high-quality heterostructures. Other techniques are based on vaporization with laser beams (pulsed laser deposition), showering of layered structures (atomic layer deposition) or chemical processes (chemical vapour deposition). A variant of chemical vapour deposition is MOVPE. In this technique, a metal-organic precursor is used to grow a material. The process is initiated by a device called "bubbler": a very pure carriage gas (i.e., hydrogen) is fed through the device from which it carries away the metal-organic compound. Accordingly, the material ratios can be controlled by the gas flow of the precursors. Instrumentally they are controlled by three main factors: The source gas flow through the bubbler, the bubblers inner pressure and the vapor pressure of the precursor. This vaporized compound contains an organic part and the element which should be part of the layer. Due to the molecular structure the vaporization pressure is rather low, allowing the complex to vaporize in the carrier gas. The enriched gas then flows into the growth chamber, where the substrate rests at a rather low temperature (around 400 to 500 °C). This temperature has to be sufficiently high to allow for the decomposition of the metal-organic molecule, only leaving behind the inorganic element. It will then diffuse across the surface until it sticks to the surface, gradually building up the crystallographic layer (Fig. 3.3). Often, the heterosystems are annealed after or in between different growth processes. This is often done by a short and steep temperature rise, allowing the atoms to diffuse and rearrange themselves in the lattice. Accordingly, defects are healed in the process, yielding an overall lowering of defects or misfits in the materials. The mode in which the material grows on the substrate is subdivided in

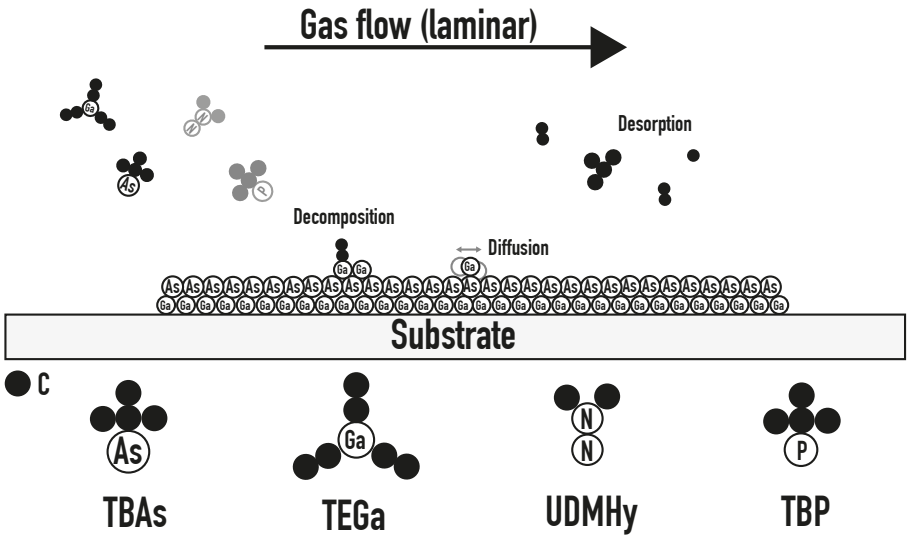

Figure 3.3: Schematic of metal-organic vapour-phase epitaxy (MOVPE) growth. The precursors are brought into the chamber with the laminar gas flow (left side) and decompose on the surface. The elements diffuse until they find their ideal lattice position and the residual parts of the precursor get carried away with the gas flow (right side). Below the four different precursors for Ga(NAsP) growth are shown. Hydrogen atoms are left out and the black circle depicts carbon.

three processes (Fig. 3.4). Basically, the layer is either grown as direct layer (Frank-van de Merwe growth[100]) or in pyramidal structure. Direct layer growth is only possible for low lattice mismatch between the substrate and the overgrown layer, whereas pyramidal growth happens for materials with a certain degree of lattice mismatch. Such pyramidal structures are further subdivided in a direct growth of these pyramids (Volmer-Weber growth[101]) or after a first non-pyramidal layer (Stranski-Krastanow growth[102]). The latter mode is mostly due to internal strain of the first layer, leading to a stacking in pyramidal patterns. Generally, the distinction between layered or pyramidal growth is through the relation of surface, interface and film free energies (per area). If the surface free energy is greater than the interface and film free energies combined, Frank van de Merwe growth occurs. Is it less than the other two growth modes occur. In reality, additional considerations to the minimization of the free energy are necessary to yield a

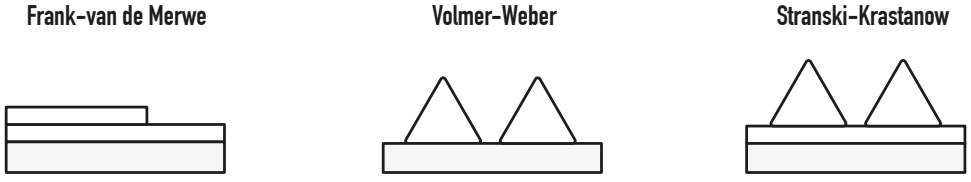

Figure 3.4: The three different growth modes for over-layer growth.

desired growth mode, e.g. interface roughness and homogeneity. Each of the growth types has its own advantage for certain fabrication processes. Pyramidal growth, as in Stranski-Krastanow growth, is desired for the growth of quantum dots[103]. Volmer-Weber growth naturally shows the biggest surface to volume ratio at the interface, thus it is important for high surface-coverage applications, e.g., catalysators. However, sometimes a Franck-van de Merwe growth is desired for heterostructures but not possible due to the material properties. With a matching combination of growth rate and temperature a (quasi-)layer growth is still possible. Typically, a low-temperature nucleation layer is firstly grown on top of the substrate to suppress the pyramidal growth modes[104]. On top of such a nucleation layer the deposition of following homo- or heteroepitaxial layers are then possible.

Another challenge which has to be taken into account is the lattice mismatch between the stacked crystal structures. If the materials are lattice matched, i.e., their lattice constant is the same or at least has only a very low difference, they can be grown on top of each other without any problem. Unfortunately, this is not the case for most systems one wish to grow. Therefore, the effects of the lattice mismatch have to be taken into account. There are three regimes of lattice mismatch with distinct effects. First, if the lattice constant mismatch is not to big the layer grows pseudomorphically strained. This means that the growing material adapts to the bigger lattice constant of the substrate in the lateral directions. However, this introduces strain in the structures which relaxes after a certain critical thickness after which misfits are introduced into the material. Second, if the lattice constant mismatch is increased further a relaxation layer grows, lowering the lattice mismatch until the growing material is basically strain free. In the third regime the mismatch is so big, that the materials cannot be grown on top of each other without an huge amount of defects or misfits and the materials cannot be grown on top of each other.

3.2 Interfaces and Band Alignment

The properties of a heterostructure is dominated by the energetically alignment of bands and the properties of their interface. It determines if exchange of carriers is possible between different materials. Typically, the properties of the band alignment is described in a schema of energy band positions over the confined axis. For comparability the band edge positions are given by their electron affinities , i.e., the energy difference from the band edge to the vacuum level.

Generally, three different configurations are possible for an interface between two materials with different band gaps (Fig. 3.5) In the first configuration, the band gap is completely enclosed in the band gap of the second material. This is a type I or straddled band alignment and reflects the simple particle-in-a-box model, if the first material is enclosed by material two on both sides. In this case, electrons and holes are both able to move from the surrounding material (barrier) into the quantum well, leading to a trapping and enrichment of carriers in the enclosed (active) material. Such configuration is often used for light emitting devices (LEDs or lasers), since for effective recombination a high carrier density is fruitful[105]. The second configuration exhibits an alginment, where the valence band of the second material lies in between the band gap of the first material. This is known as a type II or staggered band alignment.

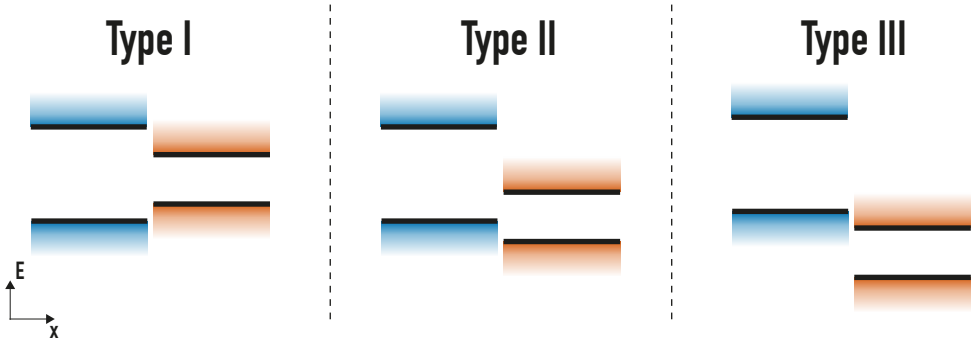

Figure 3.5: Possible band alignments for two materials in energy over space coordinates. From left to right: straddled (type I), staggered (type II) and broken gap (type III) alignment.

It's applied in so-called "W-structures", named after its potential form, when low band gap material is enclosed in the higher gap material[107–109]. In this case, narrow layers of material are grown, such that the wave function is coupled completely between active material and barrier. This can lead to a wave function which has its maximum in the - on first sight - unfavourable potential height, yielding again a high carrier density in the active material. The last configuration, called type III band alignment or broken gap, describes the alignment, where the materials are completely shifted away from each other, i.e., their complete band gap has completely different energy positions relative to the vacuum level. A band lineup for various Ga-based materials in comparison to silicon is given in Fig. 3.6.

As this differentiation is helpful in a first approach and theoretical description of material alignments it is obvious that for real devices the complete system has to be taken into account. The complex behaviour can only be described in a wave function of a full material, any other approach is only a crude approximation to the systems behaviour. Nowadays, there exists very complex structures with interesting properties, such as quantum cascade lasers[110].

Regarding a real interface between two semiconductors, the picture is not as easy as that the bands are besides each other without any interaction. Electric exchange between the two materials also has to be considered. This leads to an exchange of electrons until the Fermi level of the two materials are leveled out (Fig. 3.7). The vacuum level is then thought of to bend, since the electron affinity of the materials remain the same. However, the band offset between each of the materials stays the same. Accordingly, an offset forms at the interface between the materials and the bands are bent with respect to this offset. This behaviour depends on the alignment as well as the Fermi level offset between the materials. The Fermi level can be controlled through doping, such that the device has the desired properties. In early research on quantum-confined systems, the potential drop at an interface was used to trap electrons between the offset potential and the band bending[111]. Therefore, it is important to know the proper alignment at the interface for electrical and optical properties of a heterosystem.

Moreover, there are still multiple effects possible direct at the interface. One of them is the nature of the chemical bonding of the two materials, especially important for material alloys. Ideally there is complete charge neutrality due to bonding and orbital mixing at the interface of a binary material, such as GaP. In this case gallium donates three valence

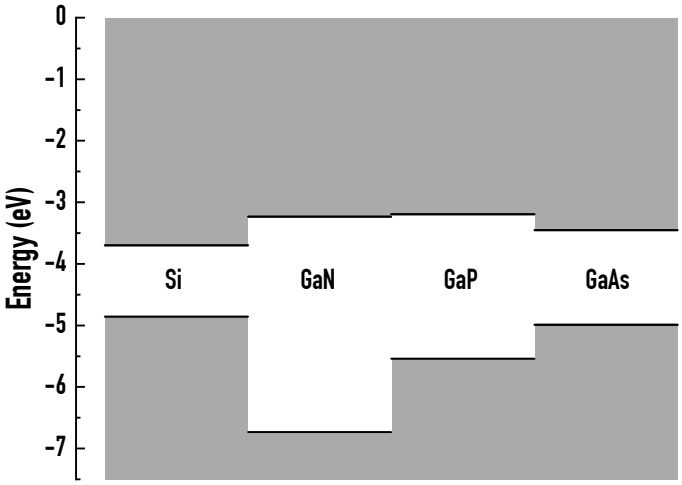

Figure 3.6: Valence and conduction band vacuum energies for silicon and three gallium based binaries. Data from Van De Walle and Neugebauer[106].

electrons and phosphorous donates five valence electrons. However, one of the atomic species is more prominent at the interface, which either acts as electrical acceptor (Ga) or donator (P), changing electrical state of the interface. The forming bonds are basically anti-site defects. Thus, the interface is now polar, which rises problems when grown onto a non-polar substrate. An example of such growth is the growth of GaP onto (0 0 1) Si substrate. Here, anti-phase domains are introduced in GaP if Si exhibits monoatomic steps at its surface[104]. Therefore, a multi-step process is necessary to grow a smooth GaP interface for further over-growth. A key in this process is to introduce double steps onto the Si surface with an homoeptiaxial over-growth of the genuine Si substrate. This results into an equal bonding of Ga and P bonds at the interface, thus no propagation of anti-sites are formed. Afterwards, the GaP is grown in a two-step process, first as a low temperature flow-modulated layer and second with a higher temperature over-growth to heal the remaining anti-phase domains in the material.

Generally, whenever a more favourable energy formation is available at the interface it will introduce propagation defects in the over-grown material.

Another effect is interdiffusion at the interface, which can happen at higher growth temperatures. This leads to unintended cross-doping across the surface, smearing of the interface - which is often desired to be atomically abrupt - happens.

3.3 Light-Matter-Interaction

The light interaction with a quantum well structure is strongly altered by the confinement. Besides the general blue shift due to the confinement induced shift of the energy levels and the change of the DOS, the relative strength of the absorption peaks is altered as well. Through the dimensional reduction excitons get smaller if the width of the structure

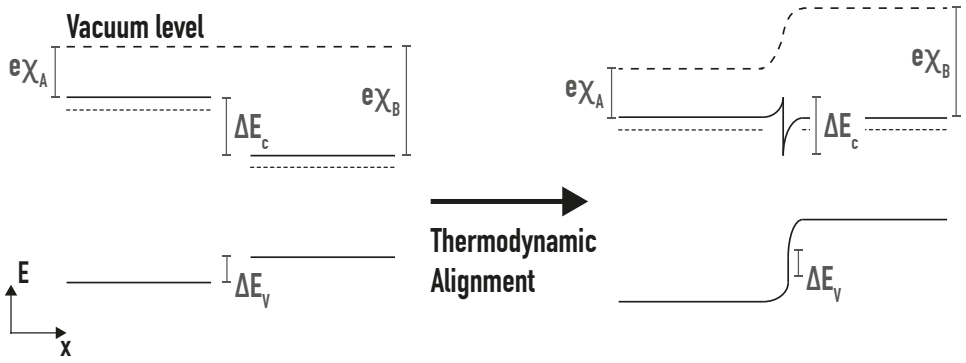

Figure 3.7: Interface alignment of two n-doped materials with different band gap. The left side shows the case for the separated materials, which align their Fermi levels, when brought together (right side). The offset between the materials stays constant as jump along the interfaces and the materials exhibit band bowing towards the interface. The electron affinities stay constant, therefore the vacuum level (dashed line) bends in the picture.

is around or below the exciton's Bohr radius. This is normally the case for Mott-Wannier excitons, since their binding radius is rather big. Typically, measurable confining effects take place around 10 nm of thickness, which is the order of typical exciton Bohr radii, too.

The 2D Elliot formula[48]

$$\alpha(\omega) = \alpha_0 \frac{\hbar\omega}{E_g} \left[\sum_{n=0}^{\infty} \frac{4}{(n+1/2)^3} \delta\left(\Delta + \frac{1}{(n+1/2)^2}\right) + \Theta(\Delta) \frac{\exp\left(\pi/\sqrt{\Delta}\right)}{\cosh\left(\pi/\sqrt{\Delta}\right)} \right] \tag{3.3}$$

describes the absorptive behaviour in this case. $\Delta = (E - E_g)/Ry^*$ is the detuning from the band gap position. The sum in the parenthesis reflects the contribution of excitons, whereas the latter part is the continuum contribution (as in Eq. 2.35). This contribution is the DOS scaled by the 2D Sommerfeld or Coulomb-enhancement factor[112]. Figure 3.8 depicts a comparison of two dimensional and three dimensional linear absorption curves. The structures are assumed to have a thickness of 5 nm (2D) and 1 μm (3D), therefore they are scaled with a factor of 200 relative to each other. The exciton peak is roughly enhanced by a factor of four in 2D structures in relation to the continuum states, i.e., exciton resonances are strongly visible. Further, there is a red shift due to the stronger exciton binding. It shall be noted here, that the zero energy refers to the effective band gap, i.e., it includes the confinement of the quantum well. Therefore, in a real structure there would be a blue shift of the two absorption curves relative to each other, due to this confinement.

However, this theoretical treatment accounts for infinitesimally narrow quantum wells, therefore a real system response lies between the 2D and 3D cases. The change of exciton binding energy can be approximated by a simple formula by[113]. The increase of binding energy with decreasing thickness is in the order of one to four times the Rydberg energy of the exciton for a well width between zero and five times the exciton Bohr radius

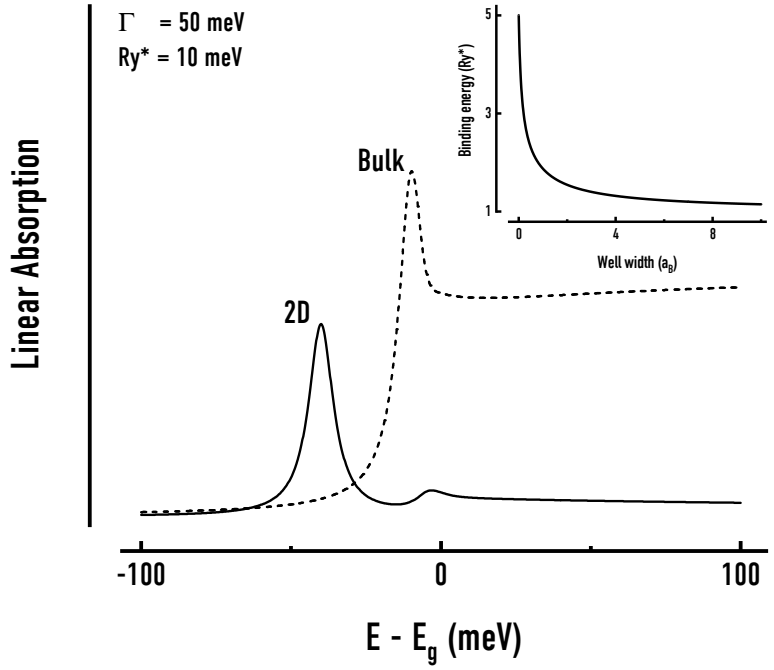

Figure 3.8: Comparison of the bulk (dashed line) and 2D linear absorption (solid line) of a semiconductor. The x-axis depicts the energy relative to the band gap of the material. The absorption is scaled by the respective sample thickness (5 nm for 2D, 1 m for 3D). The inset depicts the change of Rydberg energy with well width.

(inset in Fig. 3.8). Accordingly, in GaAs the exciton binding is increased by a factor of two (15 meV) for a typical well width of 5 nm. Studies of various heterosystems, such as (Ga,In)As/GaAs[114] or GaAs/(Al,Ga)As[115] are in accordance with this approximation. Moreover, the higher the barrier energy in comparison to the band gap of the quantum well material is, the stronger is the influence of the confinement on the lowering of exciton binding. This is reasonable, since a higher barrier prevents the exciton from impinging into the barrier, thus the exciton is more restricted in the active material.

The defect bound excitons are affected by the confinement as well. A lowering of well width leads to a stronger donator or acceptor binding in a material[116,117].

Regarding the polarization of the incident light the absorption is altered as well. As previously mentioned the confinement leads to a splitting of hh and lh levels. Since the two holes show a different total angular momentum, i.e., $J = \pm 3/2$ for the hh and $J = \pm 1/2$ for the lh, their absorption strength is sensitive on the polarization of light. For incident light perpendicular to the z axis, an electronic transition for e1 to hh is only possible with circularly polarized light (Fig. 3.9). Similarly, the e1 to lh transition is possible with circular (from $J = -1/2$ to $J = 1/2$ and vice versa) and linear polarized light ($J = \pm 1/2$ to $J = \pm 1/2$). Therefore, it is possible to distinguish the two peaks by polarized transmission measurements parallel to the quantum well plane to measure the hh-lh splitting in a material.

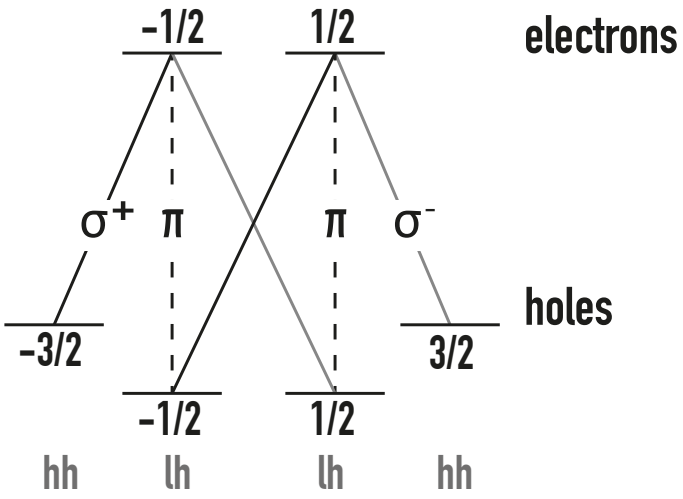

Figure 3.9: Possible transitions for light incident parallel to the quantum well plane. hhs transitions are only possible with circularly polarized light ($\sigma^{\pm}$) and lhs transitions are possible with linear (π)and circular polarizations.

4 | Electron Matter Interaction

The interaction of electrons with matter offers a unique approach to resolve either the real-space structure of materials or their energy landscape. The extremely low wavelength associated with electrons enable microscopy with extreme resolution, therefore electron microscopy is a valuable tool in material research today. Other methods reveal the lattice structure of a material by evaluating the scattering pattern of electrons, e.g. by low energy electron diffraction. Further, it is possible to deduce information on the electronic structure with techniques such as energy dispersive X-ray spectroscopy or X-ray absorption spectroscopy. However, the most straight-forward method to gain insight into the internal energy structure is through the photoelectric effect[118] and detect the kinetic energy of the electrons, which is given by

$$E_{\text{kin}} = E_B - \hbar\omega, \tag{4.1}$$

where E_B is the binding energy of the electron in the respective state and ω is the frequency of the incident light. This chapter deals with the process of this electronic emission and its energy dispersive detection, which technically is termed photoelectron spectroscopy (PES) and is employed in experiments such as XPS (excitation by X-rays) and UV photoelectron spectroscopy (UPS) (excitation by UV light). The process can be understood in terms of an inverse low energy electron diffraction[119] to deduce the spectral weights of different energies.

4.1 Three-Step Model

In essence, a three-step process describes the photoexcitation of a material (Fig. 4.1):

1. Absorption and ionization (initial state effects)
2. Travel to the surface
3. Emission into the vacuum.

Although, this approach is phenomenological, it has been used with great success in the description of the physical behaviour. Each of the three steps has its own probability or intensity of an electron reaching the detector: $P(E_{\text{kin}}, \hbar\omega)$, $T(E_{\text{kin}}, \hbar\omega)$, $D(E_{\text{kin}})$, for photoexcitation, travel, and vacuum emission, respectively. The total intensity of the emission process is then given by

$$I = P(E_{\text{kin}}, \hbar\omega) \cdot T(E_{\text{kin}}, \hbar\omega) \cdot D(E_{\text{kin}}). \tag{4.2}$$

The intensity P contains the relevant information about the electronic states, the other two have to be taken into account to correct the measurement values and to get comparable intensity values for different electronic levels. It is assumed that the photoexcitation process is non-interacting and instantaneous. Therefore, effects due to plasmons, excitons or interband excitations, and other satellite structures are neglected. However, they

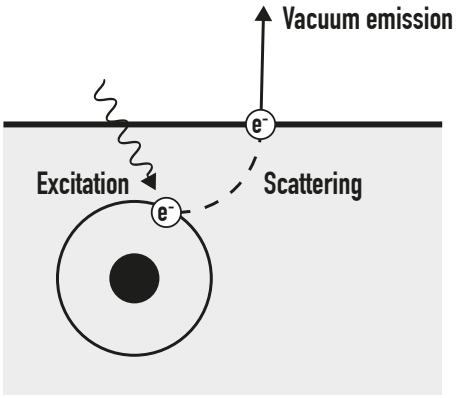

Figure 4.1: The three step model of electronic exciation: First, the electron is excited by X-rays from its electronic orbital into the material. Second, the electron travels to the surface and is scattered by the surrounding. Last, the electron is emitted into the vacuum.

can be treated as scattering terms in the travel process T or as a step between the first and second process if relevant. These interactions are known as final-state effects and are neglected here; note, however, they can be of vast importance in the compositional determination of a sample, which is not relevant for this thesis. Taking into account this approximation the process is described by a simple sum of Fermi's golden rule for each electronic level:

$$P \propto \sum_{fj} |\langle f| A\mathbf{p}_j |i\rangle|^2 \delta\left(E_f(N) - E_i(N) - \hbar\omega\right), \tag{4.3}$$

where $\langle f|$ and $|i\rangle$ denote the final and the initial states, A is the electromagnetic vector potential, p_j is the momentum operator for the jth electron excitation, and E_i are the respective electron energies. As stated above, the excited electron is interaction free, which is reasonable for high excitation energies, since the electron contains more energy than the remaining $N-1$ electron system. Further, the photoexcitation process is faster than the Coulomb interaction, thus it is not affected by it. This is known as Koopman's theorem[120] (*sudden approximation* or *frozen orbitals approximation*) and it is possible that it causes problems in PES of the valence band states, since they are typically strongly correlated. However, to date no serious problems have been reported[121]. From this point the final state energy equates to

$$E_f(N) = E_{\text{kin}} + \phi + E_f(N-1), \tag{4.4}$$

where ϕ is the work function of the material. If n photons are interacting with the electronic states, the finial and initial states become

$$|f\rangle = |n-1\rangle\,|E_{\text{kin}}\rangle\,|E_f(N-1)\rangle \tag{4.5}$$

$$|i\rangle = |n\rangle\,|0\rangle\,|E_i(N)\rangle\,, \tag{4.6}$$

where the first term describes the photon wave functions, the second the wave function of the free electron subspace in the material and the third term the wave functions of

the atomic orbitals. Thus, the electromagnetic interaction can be written as $M_{kj}a_k^\dagger a_j$ with the transition probability M from an electron state j to the free electron state k. Inserting this into Eq. 4.3 and execution of the electron operators yields

$$P \propto n \sum_{fi} |M_{kj} \langle E_f(N-1)| a_j |E_i(N)\rangle|^2 \\ \delta\left(E_{\text{kin}} + \phi + E_f(N-1) - E_i(N) - \hbar\omega\right). \tag{4.7}$$

Thus, the intensity is simply given by the sum of the transition dipole moments of the constituting electronic states. For an electronic excitation from the core levels of an atom, this formalism yields a curve with an intensity proportional to the number of excited atoms at the detection energy E_{kin}. The interaction is proportional to the cross-section of the atomic orbitals with the incident light, which typically depends on the energy of the light and the atomic species. This values are calculated and tabulated as the so called Scofield cross-sections[122] and are corrected with the actual detection angle and asymmetry of the incident beam[123]. They are calibrated for any PES after a standard procedure (ISO Standard 15472:2010[124]), which is valid as long the system stays under ultra high vacuum (UHV) conditions. The core-shell resonances are sensitive to their chemical surrounding, i.e., a doping or defect in the system leads to an increase (when charge is withdrawn - p doping) or decrease (when charge is added - n doping) of binding energy. Common chemical shifts are tabulated[125] and it is possible to extract further information on the binding of the investigated atomic species. Thus, it is possible to deduce molecular bindings in such experiments.

The second process - the travelling probability of the electrons to the surface - is dominated by the scattering of the electrons. The inelastic mean free path (IMFP) (λ) describes the distance an electron is able to linearly travel through a material. It typically depends on the kinetic energy of the electrons and has a minimum around $3-5\mathring{A}$ in the energy range of $15-200eV$ and a maximum around $100\mathring{A}$ for higher kinetic energies. This corresponds roughly to a monolayer of a crystalline sample, hence PES is very surface sensitive. Accordingly, the total probability of an electron reaching the surface reaching the surface reads

$$T = \frac{\alpha(\hbar\omega)\lambda(E_{\text{kin}})}{1+\alpha(\hbar\omega)\lambda(E_{\text{kin}})}, \tag{4.8}$$

which is often approximated as $T \approx \alpha\lambda$, since typically $\alpha\lambda \ll 1$. As a consequence, the contribution of bulk and surface emission can be controlled by the incident light energy. Typical sources available are the Al, Mg K_α Zr M lines ($1486.6\,eV$, $1253.6\,eV$ and $151.4\,eV$[123]) and the He I and He II lines ($21.2\,eV$ and $40.8\,eV$) from helium discharge lamps. The right choice of the light source depends on the IMFP, the cross section for the corresponding photon energy and the absolute energy necessary to excite electrons of the orbital under study.

The last relevant step is the transition of the electron into vacuum. The free electron inside the material can be described to be in a small potential of depth V_0 relative to the vacuum level. Therefore, it undergoes a sudden change of energy at the surface. Typically, the change in energy is negligible in the energy range of the detection, therefore, the effect is treated as a simple constant correction factor for experiments without angle resolution. For angle resolved experiments the k vector change of the electron along the parallel axis to the surface has to be taken into account to correct the angular information.

4.2 Background and Line Shape

The spectral width and shape of the photoelectron emission is determined by several physical and instrumental effects. In this section, the influence the background contributions and functions for peak fitting will be reviewed. It is necessary to know the background shape beneath the relevant spectral peaks for a resilient deduction of information from the peaks.

Often, the background intensities on the low and high energy side of the peak are significantly different. The physical reasons can be subdivided into two main loss contributions: extrinsic and intrinsic losses. The extrinsic losses are mainly happening in the traveling regime of the photoelectron. An electron can undergo inelastic scattering with other atoms or with other quasi-particles on its path through the material by electron-phonon scattering and the IMFP. Intrinsic loss features arise inherently from the photoemission process, i.e., mainly from electron-electron interaction events either due to Coulomb scattering or due to multiple (quasi-)particle processes. These lead to multiple potential final states from a defined initial orbital, thus creating background features and line broadening of the peaks. Further, electron scattering and loss lead to a decaying tail structure on the blue side of a feature.

The Tougaard fitting procedure[126] takes these different contributions into account. A reflection electron energy-loss spectrum is used to deconvolve the inelastic background contributions and to separate spectrally close peak structures. Additionally, several mathematical functions may be used to approximate the background change across peak structures, without employing any additional measurements. The most relevant are linear, polynomial, spline, Shirley[127] or universal Tougaard[128] functions. Typically, Shirley or Tougaard functions are employed in day-to-day experiments as they provide fast and comparatively reliable corrections. The Shirley background is used throughout the fitting procedures carried out in the scope of this work, therefore it will be explained in more detail here. In essence, it subdivides the background into two parts at the peak maximum, such that the areas under the peak are equal. This is often a realistic approach to the actual background, if the feature is not convoluted with a loss feature from another signal in the fitting range (which normally is very narrow around the peak), which typically is not the case. The Shirley fitting function reads as

$$S(E) = I_2 + (I_1 - I_2)\frac{A_2(E)}{A_1(E) + A_2(E)}, \tag{4.9}$$

with the background intensities I_i left and right of the peak (i.e., at the fitting boundaries) and the respective areas A_i. Obviously, the areas are only known if the background is already known. Thus, the method is iterated until the optimal parameters are found.

The line shape of a feature is governed by mainly five contributions. The first one is the inherent Lorentzian line broadening due to the electron life time ($\Gamma = h/\tau$) and temperature effects. Notably, the inner shells are broader due to their shorter recombination time. Second, the excitation bandwidth of the light plays a major role and leads to Gaussian broadening. Typically, the line width the Mg K_α line is narrower than the Al K_α, as the two are the two main excitation sources today. Yet, the lines are narrowed by monochromatization, which is often done by shining it onto a quartz plate and using the reflection as the excitation source. As a consequence of this procedure, the Al line exhibits a superior bandwidth ($\Delta E = 0.85\,eV$) compared to other sources, therefore it is mostly used in XPS experiments. The third line-shape contribution stems

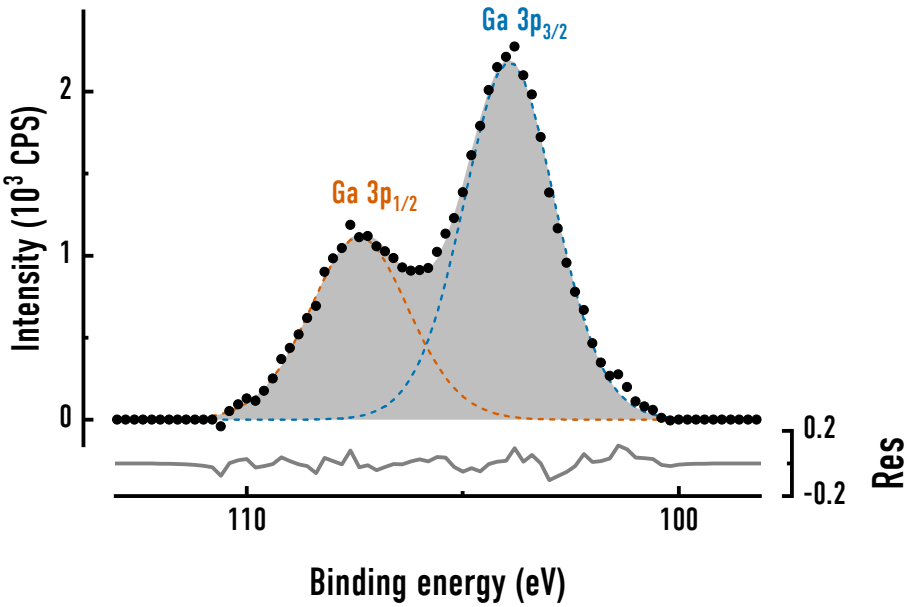

Figure 4.2: Example of core level fitting for the Ga 3p orbital. The background is fitted with a Shirley base line function and is already subtracted in the graph. Two summed Voigt curves (dashed lines) fit the data (black circles) accurately. The small graph below shows the fitting residual.

from the uncertainty in the analyzer, which usually depends on the parameters of the instrument (pass energy, slit width etc.). Since this contribution is mainly instrument related it will be further explained in the experimental section (Sec. 6.2), but it should be noted here, that it leads to a Gaussian broadening and a box function, i.e., energies get cut-off at a certain energy. Fourth, for non-conducting samples the surface of the sample is treated by an electron flood gun (neutralizer) to suppress the accumulation of surface charges. This leads to an energy spread in the surface potential, thus, again, Gaussian broadening is introduced. The last effect is contributed by possible satellite features of the excitation process, leading to an asymmetric line shape. In summary, the effect are grouped into three main parts, leading to a total line width of

$$\Delta E = \sqrt{\Delta E_{int}^2 + \Delta E_{K\alpha}^2 + \Delta E_{inst}^2}, \tag{4.10}$$

with the intrinsic, excitation and instrumental related contributions, respectively. Accordingly, the spectral features are a convolution of a Gaussian and a Lorentzian function, hence a Voigt function. Often, the simple product of a Gauss and Lorentz function is sufficient to represent the actual line shape. Then, the fitting is done with a least squares algorithm, e.g., Levenberg-Marquardt[129] or Simplex[130]. Typically, the residual of this fit is shown above or below the spectrum (Fig. 4.2).

4.3 Valence-Band-Edge Spectroscopy

Besides the core orbitals of the atoms, it is possible to measure the valence-band edge of a semiconductor by means of PES. Again, a non-interactive and instantaneous photoexcitation is assumed, therefore the binding energy of the jth electron equates to

$$E_{B,j} = E_f(N-1) - E_i(N) = \hbar\omega - E_{\text{kin}} - \phi, \tag{4.11}$$

which is directly related to the photon energy, the work function and the measured kinetic energy. An additional consequence of the relaxation-free interaction, the final and initial states have to be identical, thus $E_f(N-1) = E_i(N-1)$. The initial state energy is the sum of the one electron energy (ϵ_j) and the remaining system: $E_i(N) = \epsilon_j + E_i(N-1)$. Hence, the binding energy directly reflects the one electron energy

$$E_{B,j} = -\epsilon_j. \tag{4.12}$$

Introduction into Eq. 4.7 leads to a photoionization proportional to

$$P \propto \sum_{fi} |M_{kj} \langle E_f(N-1)| a_j |E_j(N)\rangle|^2 \delta(E_k + \phi - \hbar\omega - \epsilon_j). \tag{4.13}$$

In a valence band mixing process, the delta function represents the DOS, which is scaled here by its transition probability into the free electron dispersion. The final state function is known as the partial DOS (or pDOS), which is scaled by the relative Scofield cross sections of the hybridization orbitals of the semiconductor. This can lead to significantly deviating features at the valence band states. Figure 4.3 shows an example of a (Cu,In)Se_2 sample excited with two different photon energies (21 and 80 eV). The different contributions are attributed to either the Cu or Se pDOS, which have a different cross section, i.e., the Se 4p orbitals cross section scales roughly a factor 60 from 80 to 20 eV excitation (Cu stays approximately constant)[132]. Therefore, the contributions of both are differently pronounced in each of the two spectra. Thus, it is important to compare measured valence band spectra with the cross sections of the constituting orbitals to compare them to a measured or calculated DOS. Generally, the cross sections lower from the resonant excitation, hence for valence band states it is important to use photons with lower energy, such as UV light from helium discharge lamps. The difference of the cross sections between He excitation (40.8 eV) and Al K_α (1486.6 eV) is about 3 to 5 orders of magnitude. Figure 4.4 shows the dependence of the Ga 4s and As 4p orbital with excitation energy (from Yeh and Lindau[132]). In this extreme case it is obvious that for excitation below 40.8 eV the measured curves would significantly differ, with a strong increase of As contribution over the Ga contribution. However, excitation with the He(II) line would model an approximately equal Ga and As contributions, thus reflecting a realistic DOS.

Often one is not interested in the form of the valence band states but more in the valence-band-edge energy. Typically, this value is extracted by linear fitting or by using a theoretical DOS (where the relative cross sections are of major important). For semiconductors, only the DOS reflects the correct band edge, due to the neglected Coulomb interactions which can manifest themselves as tail states or broadening of the edge. Further, the measured data is instrumentally broadened (Gaussian), thus if theoretical DOSs are employed they have to be broadened, too. The full procedure of valence band edge fitting is given in the methodical section (Sec. 6.2).

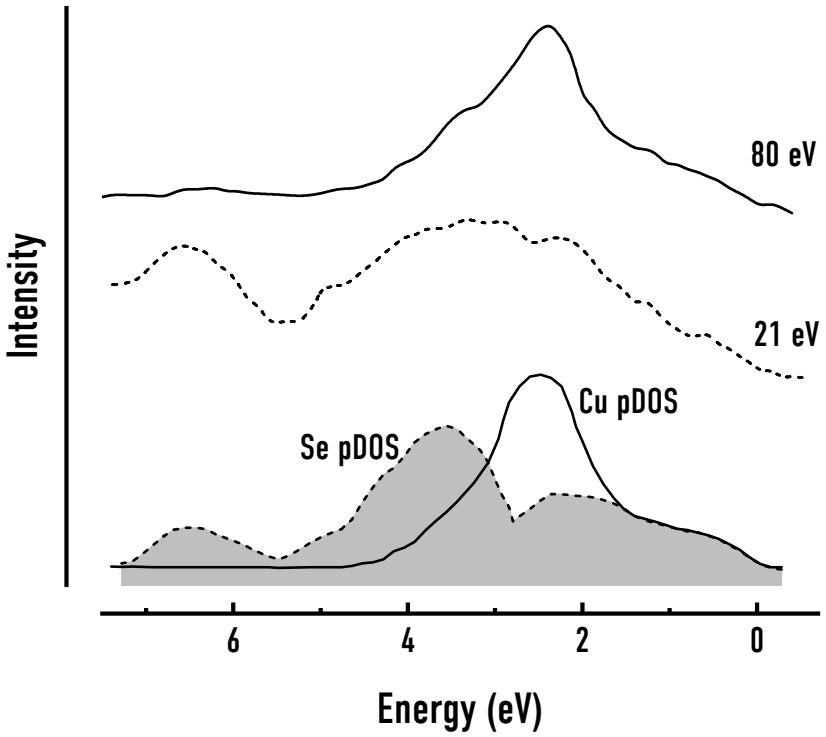

Figure 4.3: Influence of the excitation photon energy on the measured form of the valence band edge in $CuInSe_2$. The feature is differently composed by the different partial DOSs of Se and Cu (simulation shown on the bottom of the graph) due to different cross-section relations at 21 eV and 80 eV. Data from Löher et al.[131].

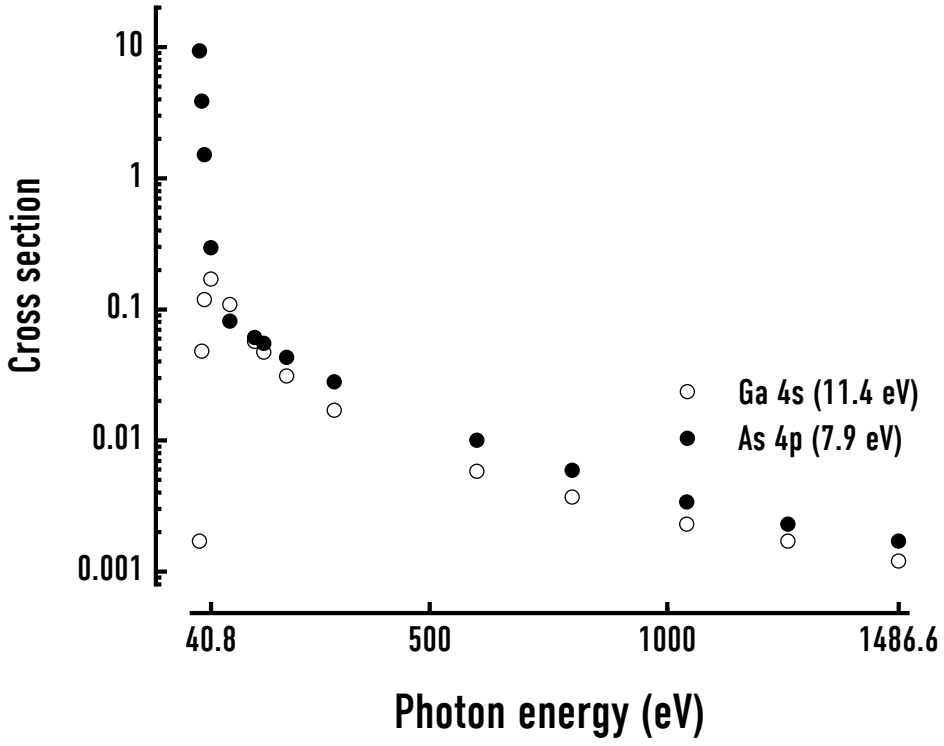

Figure 4.4: Comparison of scofield cross-sections for Ga 4s (hollow circles) and As 4p (filled circles) orbitals for different photon energies.

I

Determination of the Ga(N,As,P)/GaP Band-Offset

5 | Ga(N,As,P) Heterostructures

The material under study in the following sections is Ga(N,As,P). It is designed as active material for lasers on Si embedded in a heterostructure, i.e. multiple layered structures of different materials. In this section, the function of each of the layers will be discussed and the properties of the complete heterostructure will be reviewed. Further, the specific sample series on which the experiments are performed is introduced and explained.

The central idea behind the growth of such a quaternary system is its potential for integration onto CMOS ready Si substrates. Band gap and lattice constants in quaternary materials can be tuned independently within certain limits[133]. This enables pseudomorphical growth to silicon of a direct band gap structure with a residual band gap tuneability. The dependency of band gap and lattice constant for the alloy is shown in Fig. 2.8, from which the lattice mismatch to silicon is apparent. It is obvious that the compound can be grown with a low lattice mismatch, thus suppressing misfits and defects in the material. Strain may even be favorable for laser structures as it reduces the threshold[134]. This allows for devices in the datacom (880 nm) or telecom (1550 nm) wavelength regimes. Therefore Ga(N,As,P) is a promising material for replacing expensive GaInAs lasers on InP substrate used in data transmission today. First studies of the material show that the material stays direct for up to 26 % phosphorous with a constant nitrogen level of 4 %[20]. Moreover, the system can be grown with MOVPE, thus allowing for up-scaling on industrial levels.

The precursors for the different materials are tertiarbutyl arsin (TBAs), tertiarbutyl phosphine (TBP), unsymmetrical dimethylhydrazine (UDHMHy), triethyl gallium (TEGa) and triethyl boron (TEB) for arsenic, phosphorous, nitrogen, gallium and boron, respectively[21]. The material crystallizes in a zinc-blende structure through sp^3 hybridization, similarly to GaAs, as do all materials in the complete heterostructure. Further, nitrogen acts as an isovalent impurity above levels of $x \approx 0.2\%$ in Ga(N,As)[135], thus nitrogen is diluted into the Ga(As,P) host matrix of the material. This leads to BAC effects of the virtually dispersionless (defect-)band associated with nitrogen and the conduction band of the host matrix (see Sec. 2.1.4 for further information), giving rise to the strong anomaly of band gap bowing between GaAs and GaP . This is invaluable for device design, since nitrogen alters the lattice constant only relatively little. The small change is a consequence of nitrogen's diluted incorporation, yet nitrogen infers strong changes of the band gap energies. Therefore, this is a further advantage for band gap engineering with this material system.

It is necessary to compensate the compressive strain acting on the Ga(N,As,P) material despite the possibility of pseudomorphic strain. Further, the active layer should be rather thin, i.e., a quantum well, to maximize the carrier overlap and to increase the recombination efficiency. As a consequence, the cladding material has three major roles: the confinement of light through a higher refractive index, the confinement of carriers through a higher band gap and a suitable alignment and the possibility of strain compensation. It is self-evident that Ga(As,P) layers are good candidates, since the material can be lattice matched to Si in the multilayer structure. Moreover, an incorporation of boron into Ga(AsP) allows for tensile straining of the material through

the low covalent radius of boron[136]. Similarly to nitrogen, the boron is introduced diluted into the Ga(As,P) host lattice above a certain ratio. A MOVPE growth study for (B,Ga)P and (B,Ga)(As,P) layers reveals a maximum boron concentration of 7.8 % and 9.9 % atomic percent boron for good crystalline quality[136]. Above this atomic percent values boron exhibits surface segregation, local lattice distortions or phase separation leading to an inhomogeneous or defect related material.

However, the introduction of boron and the nitrogen in the active material raises an additional challenge: boron and nitrogen form strong bonds[137,138]. These lead to the formation of localized B-N non-radiative recombination centers at the interface[139], thus suppressing the light emission and may hinder lasing completely. As a consequence, the PL emission intensity is lower in the material[21]. Therefore, a boron-free material is introduced in between the barrier and the active layer, suppressing the bonding of nitrogen and boron. GaP is suitable, since the lattice mismatch to silicon is rather low (0.36 %). Although the mismatch is low, the layer should still be thin, in order to not introduce any misfits in the following material. Kunert et al.[21] showed that a GaP layer of roughly 3 nm to 5 nm (depending on surface roughness) is sufficient to suppress the B-N bonding and still maintain good crystalline quality. Further, the PL intensity is retained compared to a boron free barrier. However, it should be noted that the large band gap of GaP may yield these layers as effective barriers.

In summary, it is possible to grow defect-free and strained heterostructures of Ga(N,-As,P)/(B,Ga)(As,P) layers onto silicon. Yet, a major part of the integration is still missing: the defect-free integration onto silicon substrate. It is desirable to grow the system on such substrates as CMOS manufacturers require an exact (001) silicon surface with a maximum miscut of 0.5%. The growth parameters have to be controlled to achieve a smooth and defect free surface. The surface has to be nucleated before the MOVPE layering as GaP and GaAs tend to grow in Stranski-Krastanow mode on Si[140]. The pyramidal growth of GaP is mainly due to the monoatomic steps on the (001) Si surface, leading to an alternate binding of gallium and phosphorous atoms[140]. This introduces anti phase boundarys (APBs), which propagate through the overgrown material and in the extreme case leads to the pyramidal growth conditions. With a three step process the smooth integration of GaP onto Si is possible[104]. The first step is the overgrowth of a homoepitaxial buffer onto the Si substrate to reach a homogeneous covering with double atomic steps on the surface. These double steps allow the GaP to grow, such that the amount of surface bonds of Ga and P is equal, thus APBs are suppressed. The next step is an overgrowth of GaP at low temperature to suppress cross-doping of GaP and Si. Further, the flow rate of the precursors is modulated to achieve an even better layering of GaP, since the P-Si bond is stronger than the Ga-Si one. Thus, it is obvious to let Ga diffuse to its ideal energy position first and let the P atoms fill in the gaps between. This procedure enables the charge free growth of the first atomic layers of GaP, which is essential for a successful two dimensional overgrowth. Then, the last step is to overgrow this first GaP layer with a GaP layer at higher growth temperatures. This leads to self-annihilation of remaining APBs and other defects. The GaP surface is free of defects and APBs after a growth of roughly 40 nm to 50 nm, thus offering a smooth surface for the further growth of the heterostructures. In conclusion, the full heterostructures consist of at least seven different growth steps and six material layers. Figure 5.1 shows a typical arrangement of this structure, with the layers as introduced before. Typically, the system is grown as a multi quantum well (MQW) structure, therefore reaching a higher optical output and an intrinsic statistical averaging of the active layers. The barriers are roughly

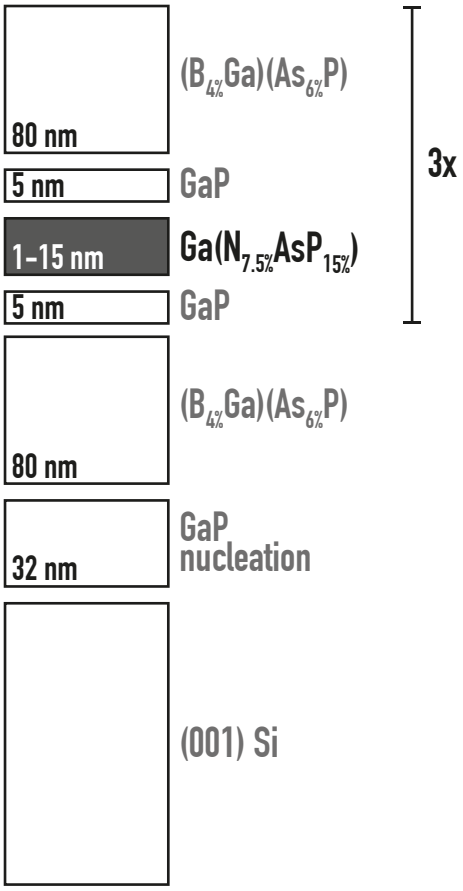

Figure 5.1: Sample structure of the Ga(NAsP) heterostructure.

80 nm wide and embed the active material (Ga(N,As,P)) of 5 nm thickness for typical samples. Further, the intermediate GaP layer has a thickness of 1 nm or 5 nm depending on the sample and its interface roughness.

The interface quality may be atomically abrupt for these samples, depending on the growth parameters of the structure[141]. Typical parameters are a growth temperature of 525 °C and a subsequent annealing step at 925 °C. For higher growth temperatures, the behavior of the system is rather unexpected: the interface roughness increases dramatically but the layer composition is more homogeneous[142]. The improved homogeneity is surprising, as it is to expect that the higher temperature leads to a stronger diffusion of the diluted nitrogen in the material, which can, in the worst case lead to phase segregation. A comparison of compositional variation from transmission electron microscopy images for a quantum well grown at 525 °C and 700 °C shows a stronger interface modulation of the high temperature grown sample[142]. Further, it is evident from Wegele et al.[142] that the fluctuations inside the well are less pronounced for the sample grown at 700 °C, compared to the one grown at 525 °C. In essence, there exists a trade-off between homogeneity and interface roughness regarding the temperature during the growth process. Both, homogeneity and interface roughness are important parameters for efficient light emitting and lasing.

For a theoretical description of the heterostructure, it is essential to know the relative atomic percentages of the constituting species in the active layer. Since the determination of composition and crystalline quality by x-ray diffraction (XRD) is only possible for ternary materials, additional parameters have to be taken into account when studying quaternary systems. A useful quantity to estimate the band gap energy of the material is the PL energy. However, local defect centers also show strong PL (see Sec. 2.1.6 for further details), which shifts the actual emission energy and masks the actual band gap emission energy. The composition is determined from the PL energy in conjunction with three additional energy shifts. These shifts arise from the confinement, the strain induced hh-lh splitting and the nitrogen induced BAC effects on the conduction band The BAC coupling constant of the Ga(N,As,P) heterostructure on GaP and Si substrate have been determined to be $C = 1.9\,\text{eV}$ and $C = 1.75\,\text{eV}$ from Jandieri et al.[143]. This approach in conjunction with XRD measurements offers a resilient tool for the elemental ratios in the active material with an error of $\Delta x_n = 1\%$ and $\Delta x_P = 5\%$ for nitrogen and phosphorous concentrations. In the experimental section of this work a similar method is employed, therefore the reader is referred to Sec. 7.1 or Jandieri et al.[143] for a more detailed review of this method.

The capability of these multilayer structures as lasing devices has already been demonstrated for low temperatures (150 K) on a Si substrate[22] and on a GaP substrate[144]. Around the lasing threshold, the modal gain of the sample is in the order of $10\,\text{cm}^{-1}$. This is a good value given a modal gain of $50\,\text{cm}^{-1}$ in the material (GaIn)(NAs)/GaAs[145]. Yet, room temperature lasing of such devices has not been reported to date. Therefore, a further study of internal fluctuations and non-radiative channels is necessary. Moreover, the relative band alignment of the layers with respect to each other remains unknown. This knowledge can shed light on the internal structure and behaviour of this system, enabling further optimization regarding carrier and optical confinement. The following results section deals with the deduction of the band alignment of the several layers by means of two different methods: PLE and XPS.

The sample series under study has been grown by keeping the growth parameters constant. They were grown at a temperature of 525 °C. Subsequently, the samples have been annealed at 925 °C to heal lattice defects. The growth times of the active layers have been varied from 6 s to 54 s leading to well widths between 1.5 nm and 12 nm as well as slight variations of their phosphorous contents. The ratios for each sample are given in Tab. 5.1 for the active layer.

Figure 5.1 depicts a schematic of the full stack with all involved layers. It exhibits a MQW structure with three quantum wells with 80 nm thick (B,Ga)(As,P) barriers in between. The boron and arsenic group III composition ratios are $x_B = 4\%$ and $x_{As} = 6\%$, respectively. A thin GaP layer is grown in between the active and barrier layer to prevent B-N bonding at the interface.

Additionally, one sample (27152), which consists of 143 nm (B,Ga)(As,P) in between two 32 nm GaP layers on Si substrate is used for the XPS measurement. Growth temperature and group ratios are the same as for the other Ga(N,As,P) heterostructures. The sample is used for the determination of the sputter rate of the (B,Ga)(As,P) barrier, as well as the (B,Ga)(As,P) / GaP and GaP / Si interface.

Table 5.1: Sample thickness and P and N content for the Ga(NAsP) well width series. The thicknesses were determined by XRD and TEM measurements.

Sample	d_{XRD} (nm)	d_{TEM} (nm)	x_P (%)	x_N (%)
26431	1.5	1.6	-	-
26446	4.0	4.2	14.7	7.0
26403	5.7	6.9	14.6	7.3
26432	8.4	9.3	13.0	7.1
26447	9.9	12.1	12.0	7.3

6 | Methods

6.1 Photoluminescence Excitation Spectroscopy

PL is a versatile tool to measure the emission emerging from semiconductor band gap and defect state transmissions. It is often employed as a method to characterize the band gap energy of samples[143]; its intensity change is neglected in most cases. Mainly, there are two extensions based on the intensity of PL: absolute emission measurements, where an integrating sphere is used to collect all the light emitted by the sample under study. The intensity is relevant for two common PL based techniques: quantum efficiency measurements with an integrating sphere and PLE. PLE monitors the relative PL intensity during the change of incident photon energies. It provides an absorption-like dataset incorporating effects of relaxation of excitations towards the band gap energies. Therefore, it is most suitable to measure absorptive behavior of an opaque sample, where transmissive linear absorption measurements are challenging. Albeit, it is possible to measure reflection and deduce the absorption by Kramers-Kronig transformation, its use for thin buried layers is challenging, too. Similar to reflection measurements, it is possible to measure states with energies above the band gap of semiconductors as their characteristics are often not visible in typical linear absorption measurements, due to strong attenuation of light above the band gap. This is especially useful for the investigation if an incident photon is absorbed and followed by radiative emission of the electronic excitation. Typically, the emitted intensity is calculated as

$$I_{\mathrm{PL}} \propto \alpha\left(\lambda\right) \Phi_{\mathrm{PL}} I_{\mathrm{exc}}\left(\lambda\right). \tag{6.1}$$

In first approximation, only the absorption coefficient α and the excitation intensity I_{exc} are wavelength dependent. If the luminescence quantum efficiency Φ_{PL} (i.e., carriers converted to photons) is independent of excitation energy the technique is able to measure a value proportional to that of the absorption coefficient of the material under investigation. Accordingly, it is ideally for absorptive measurements of materials with a low absorption cross-section on opaque substrate, such as the quantum well systems on silicon investigated in this work. While the measurements seem straight forward at first, the technique is often challenging for such samples, regarding the supply of high intensity and wide bandwidth excitation sources. Incandescent sources often don't supply the necessary photon fluxes and lasers commonly do not cover the desired tuning ranges or are available for discrete wavelengths only. Accordingly, one has to use an optical parametric amplifier or take advantage of the recent emergence of high power non-linear PCFs. Such fibers are able to produce a broad emission under pumping with short-pulsed monochromatic laser light. White-light spanning nearly 2 octaves is generated by self-phase modulation and soliton formation. In the experimental setup, a "holey" photonic crystal fiber optimized for Ti:sapphire fs lasers is used. The Ti:sapphire laser has a total output power of 800 mW and a pulse duration of 30 fs. In the experimental setup (Fig. 6.1) a spectrum with 150 mW total power from 0.62 eV to 3.1 eV nm is generated with a PCF (Femtowhite PCF 800). Peak spectral powers have been 0.5 mW/nm at around 500 nm (Fig. 6.1).

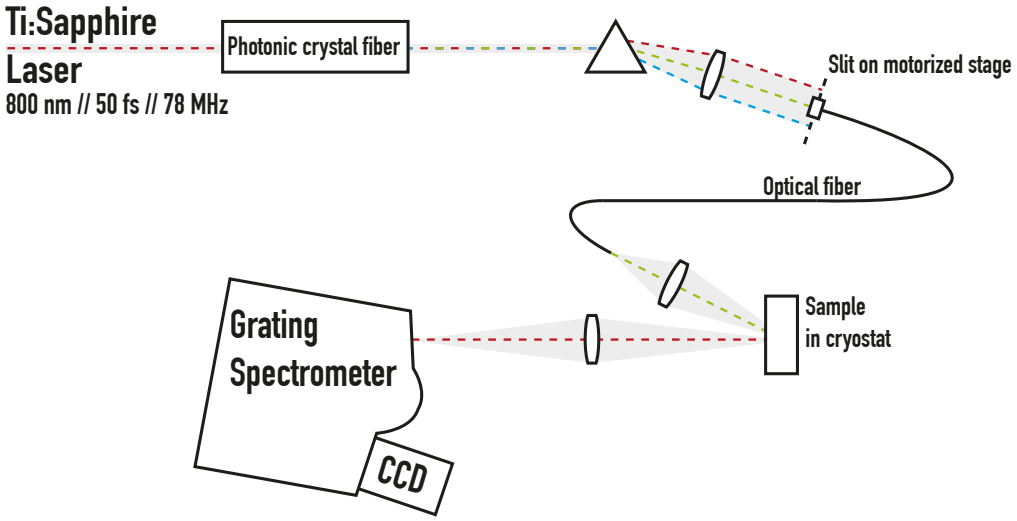

Figure 6.1: Schematic drawing of the PLE setup. The photonic crystal fiber generates white-light, which is dispersed by a prism and collected by a slit on a motorized stage. The sample is excited by the monochromatized light and the emission is collected by a grating spectrometer and Si charge-coupled-device (CCD).

The desired wavelength is selected from the supercontinuum white-light by dispersing the light in a prism and imaging the light into an optical fiber. This optical fiber is mounted on a movable stage to select the desired wavelength. Additionally, a slit is placed in front of the fiber to improve wavelength resolution. The output facet of the fiber is imaged onto the sample surface by an achromatic lens. The sample itself is mounted in a closed cycle helium cryostat (CTI-Cryogenics 8300 compressor and M22 cryodyne refrigerator). The PL emission efficiency is enhanced by temperatures as low as 15 K, which are achievable with this cryostat. The low temperatures suppress non-radiative recombination channels and phonon scattering and thus, yield a higher probability of radiative recombination. A 5:95 beamsplitter extracts 5 % of the light for power measurement with a commercially available power meter (Thorlabs PM100) to account for power fluctuations. The PL signal from the sample is imaged onto the entrance slit of a f/4.1 Czechy-Turner spectrometer (Jobin Yvon Horiba Triax 320). After dispersion the light is detected by a liquid nitrogen cooled Si CCD, which is mounted at the output port of the spectrometer.

The use of an array detector allows the recording of a spectrum for each excitation wavelength. Accordingly, it is possible to record 2D excitation maps of the PL emission to compare different emission peaks from a sample. Additionally, the signals are spectrally integrated to extract an absorption like curve from the sample. For resonant measurements a filter cuts off the higher energetic parts of the spectrum. Therefore, only the lower energetic tail of the PL is detected in such cases.

Since the PCF retains the pulses of the exciting laser it is in principle possible to measure transient PLE with the appropriate time resolving detection. This extension is planned as further step of such measurements.

6.2 X-Ray Photoeelectron Spectroscopy

Considering measurements of energy levels inside any material, electron spectroscopy is a very powerful tool. This approach uses the photoelectric effect to experimentally determine energy levels. Energy-rich X-ray radiation excites the photoelectrons from the core levels (CLs) of a material. This method is simply called XPS, formerly known as electron spectroscopy for chemical analysis (ESCA), the term which is nowadays used more broadly. The technique was developed in the late 1950 and 1960 by the group of Kai Siegbahn, who was honored with the Nobel prize in 1981 in physics for his achievements, together with Schawlow and Townes for their pioneering work on laser spectroscopy. His father, Manne Siegbahn also received the Nobel prize in physics in 1924 for his work on X-ray spectroscopy, already preparing the ground for the work of his son. However, electrons have a very short IMFP and therefore measurements not only have to be carried out under UHV but they are very surface sensitive, too. In this work XPS is the tool to determine the band-offset between two materials inside a heterostructure. Accordingly, a much greater depth information is needed compared to the IMFP of the electrons, which can be employed by different methods. Here, destructively sputtering with Ar^+ ions of the sample is employed to measure slices at different depths. In this section a detailed explanation of XPS and the determination procedure of band-offset between semiconductor interfaces is given.

It is very important for any electron spectroscopy to employ excellent vacuum conditions (UHV systems are mandatory) and therefore XPS systems are often available as fully equipped commercially available setups. Here, a PHI VersaProbe by Physical Electronics is used throughout the experiments. The X-ray excitation energy is provided by the Kα line of Al, which lies at 1486.6 eV. It is monochromatized by Bragg scattering on a quartz crystal to suppress the bremsstrahlung and additional lines. The emission is focused onto the specimen in the analysis chamber under an incident angle of 45°(Fig. 6.2). The chamber is equipped with an electron flood gun, to neutralize the surface of isolating samples, an Ar^+ ion and C_{60} (not shown in Fig. 6.2) gun, for sputtering and a helium lamp for UV radiation, too. To provide an absorption-free environment for both X-rays and electrons, the chamber is kept at a pressure better than 10^{-8} mbar. To ensure a contamination free transfer of samples, a load chamber is used to change between vacuum and atmospheric pressure. The emitted photoelectrons are collected by an electron lens system, which fulfills two major tasks: retardation of the electrons and collecting as well as focusing onto the entrance slit of the concentric hemispherical analyzer (CHA). The retardation is done to decelerate the electrons to an appropriate pass energy in the CHA. This is necessary to ensure a sufficient energy resolution, which is given by the relation $\Delta E = 0.63 w_1/R_0 \cdot E$. Accordingly, the retardation of electrons ensures firstly the same resolution across the recorded spectra and secondly higher intensities, i.e., the hemisphere can have a smaller radius in relation to the aperture, which results in a higher throughput. Electrons in the CHA are dispersed by the inner and outer potential (V_1 and V_2 in Fig. 6.2) of the hemispheric surfaces. This establishes a Wien filter selecting the electrons to pass through the output slit w_2. There a 128 data channel detector digitizes the signal and the spectrum is read by a computer system. The electron lens and CHA supply two different operation modes: fixed retardation ratio (FRR) and fixed analzyer transmission (FAT). The FRR mode is mostly used in Auger electron spectroscopy, which ensures high intensities but spectrally changing energy resolution. Contrary, a constant resolution is desired for XPS measurements.

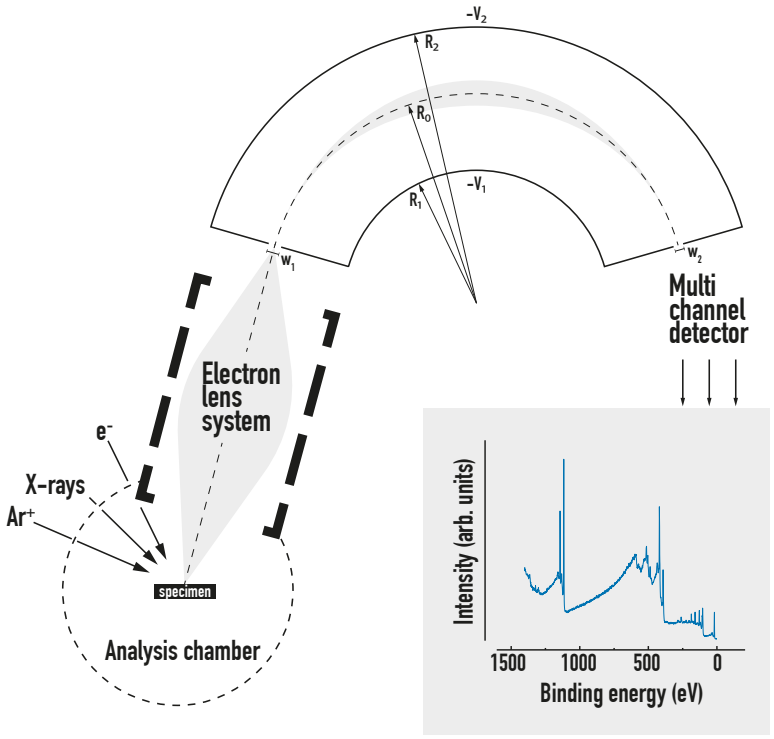

Figure 6.2: Schematic drawing of the XPS experimental setup. The sample is illuminated with X-rays and the emitted electrons are collected by an electron lens system. A hemispherical analyzer disperses the electrons and at the end of the analyzer they are detected by a multichannel detection system. The inset on the bottom right depicts a typical XPS spectrum.

The constant resolution desired for XPS is provided by the constant energy pass in FAT mode. In this case, the retardation of the electron lens is changed throughout the energy-range scan, such that the photoelectrons have the same energy at the entrance slit of the CHA (w_1). Therefore, the FAT mode is commonly used for XPS acquisition.

Although, the measurement appears straight forward, it is prone to different instrumental and material specific errors and uncertainties. The electron lens doesn't have a constant transmission for different kinetic energies which distorts measurements in the FAT mode. Therefore, the intensity of the photoelectron signal is altered throughout the spectrum. The transmission function of the PHI VersaProbe is given by

$$T(E_K) = E_P \left(\frac{a^2}{a^2 + (E_K/E_P)^2} \right)^b , \tag{6.2}$$

where E_K is the kinetic energy of the photoelectrons, E_P is the pass energy of the CHA and a, b are instrument related constants which are provided by calibration routines. Additionally, the cross-section of the orbital compared to the X-ray radiation yields an error for different atomic species. These Scofield cross-sections can be calculated and are tabulated in the literature[123] for the magic source angle of $54°44'$. They have to be corrected for the instruments source angle and are taken into account during the fitting procedure of the peaks. The IMFP of the photoelectrons is the most important

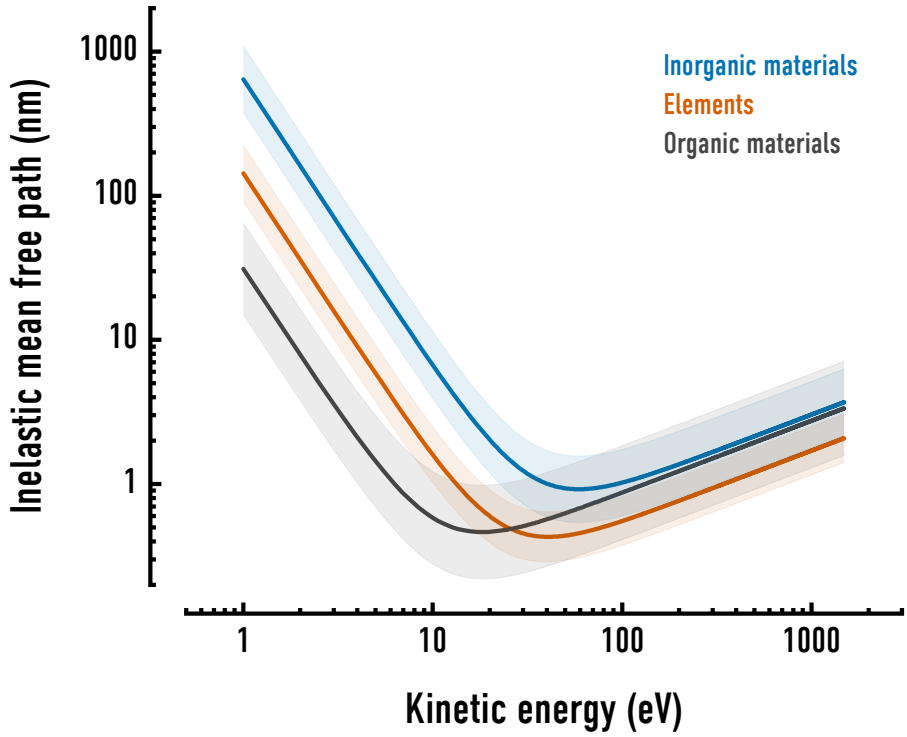

Figure 6.3: Theoretical electron ineleastic mean free path for elements (orange), inorganic (blue) and organic (grey) materials in dependence of the electron energy. The shaded areas depict the deviations from the curve found throughout different materials. Data from Seah and Dench[147].

error source in depth profiling. It describes the absorption coefficient for electrons in a material. Assuming the Beer-Lambert[146] law the surface intensity I_s of emitted electrons from depth d is calculated as

$$I_s = I_0 \exp\left(-d/\lambda \cos\theta\right),$$

where λ is the IMFP, I_0 the source intensity of electrons and θ is the incident angle. Subsequently, about two thirds of the electrons originate from a depth of 1λ and nearly all of the intensity (95 %) comes from a 3λ depth. Electrons from different depth regions of the sample are measured in different energy positions in the spectrum. Accordingly, the electron count reaching the surface depends on the scattering characteristics inside the sample, which depend on sample composition. Figure 6.3 shows a comparison of different IMFPs for several elements, as well as for organic and inorganic materials. All of the curves follow the same standard formula[147]

$$\lambda = \frac{A}{E_K^2} + B\sqrt{E_K}. \tag{6.3}$$

Here, E_K is the kinetic energy (in eV) of the electrons and A and B are fitting parameters, λ is the IMFP in nm. For inorganic materials like the ones studied here, the parameters are $A = 641$ and $B = 0.096$, respectively. The high kinetic-energy side is most important since the aim in this work is to measure the valence band (VB) offset of two materials.

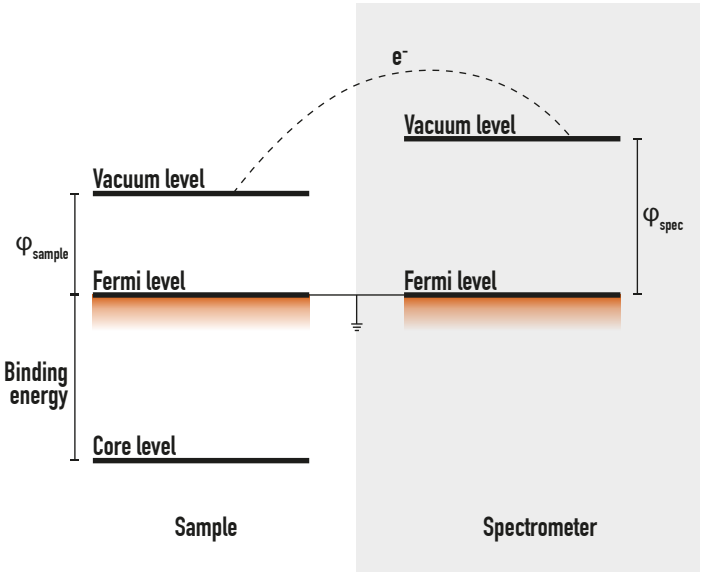

Figure 6.4: Alignment of a conducting sample with respect to the Fermi level of an XPS detector. Through the known work function of the spectrometer the samples work function can be measured with great precision. For isolating samples, the Fermi levels are not connected, thus an additional energy uncertainty is added to the measurement.

VB photoelectrons mostly carry the excitation energy in their kinetic energy, since the vacuum level energies of most semiconductors are around or below 1 eV. Accordingly, the IMFP is around 4 nm (2/3 of signal) to 10 nm (95 % of signal), or 7 to 20 atomic layers, respectively, for photoemission around the Al K_α line (1468.6 eV). All of these three measurement uncertainties mainly affect the electron flux, which is important for composition determination of samples but not for offset determination, since this solely depends on the energy of the photoelectrons. The kinetic-energy measurements are also influenced by the instrument response.

For the accurate determination of the binding energy, the Fermi energies of the sample and of the detector have to be related, which is easily done for conducting samples. The Fermi levels of conducting samples and detector align simply by connecting both to electrical ground (Fig. 6.4). The binding energy is then given by

$$E_K = h\nu - E_B - \phi_{\text{sample}} - (\phi_{\text{spec}} - \phi_{\text{sample}}) = h\nu - E_B - \phi_{\text{spec}}, \qquad (6.4)$$

which solely depends on the work function ϕ_{spec} of the spectrometer, which is known and corrected by the software. For isolating samples, however, the situation is less straight forward as the work function of the sample and the spectrometer are arbitrarily aligned. Their difference $\Delta\phi$ is determined by taking a known CL energy and use it to correct the offset in the measurement. Mainly carbon or oxygen peaks are used for this, since they are present as contamination on virtually any surface. However, the samples Fermi level stays not the same throughout the measurement. It is altered by surface charging due to constant electron loss from the emission process. Therefore, the sample is neutralized during the measurement by flooding the sample with low energy electrons from an electron flood gun mounted in the analysis chamber.

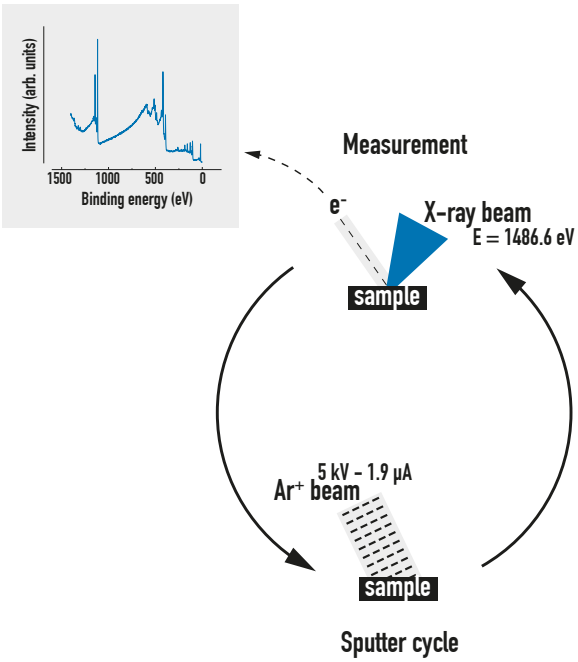

Figure 6.5: Cycle of a depth scan XPS measurement. The data collection (top) alternates with sputtering of different times (bottom), according to the actual investigation depth.

Regarding the determination of offset between to materials the IMFP is very important, as well. It does not only alter the intensity of the sample but it also restricts the depth in which measurements can be made. As stated above, the escape depth around the maximal kinetic energy is limited to about 3λ. It is therefore impossible to investigate an interface between two samples of thicknesses above 10 nm. It is possible, however, to measure interfaces where one of the materials is thinner than 10 nm without destroying the sample by tilting of the sample delivers depth information due to the changing path length. Samples exceeding this thickness can only be measured destructively by sputtering through the sample. The setup is equipped with an Ar^+ ion gun for this purpose. It is capable of producing an ion bombardment with an kinetic energy of up to 5 keV as well as much lower energies for surface cleaning of samples. For depth profiling of a sample, alternating cycles of photoelectron measurements and ion beam bombardment are carried out (Fig. 6.5). Basically, any thickness of samples can be measured with this technique, the only restraints are the time it takes to sputter through a sample and that the samples fit into the measurement chamber. Sputter rates are typical in the range of a few tenths of nm/s, allowing for great precision of depth profiles regarding the depth accuracy. Albeit, this technique allows for measurement of arbitrary depths inside a sample it comes with a few drawbacks. These can be divided into three main factors: instrumental, sample-specific, and ion radiation related factors. Instrumental uncertainties include mainly sputter gun related issues: the purity, uniformity, and time dependence of the ion beam. These factors are often specified in great detail for a given system and therefore very predictable. Additionally, the issue of redeposition and adsorption of residual gas exist, which depend on the samples constitution and composition. Similarly, the interaction of the Ar^+ ions depend on

the sample configuration, such as surface roughness (as cascading effects from the original surface), the crystalline structure and defects which can lead to channeling inside the sample. Most importantly, there is the effect of preferential sputtering: different atomic species are more easily sputtered than others and accordingly some elements are overabundant after a certain sputter time. Unfortunately, this effect is cumulative and gets stronger the deeper the sputter crater. The only way to avoid preferential sputtering is using an ion bombardment of less kinetic energy, since the sputtering effects scale with it[148]. Some researchers also reported strongly reduced sputtering effects using C_{60} as bombardment[149]. However, this has been studied on organic materials, where the sputtering effects of Ar^+ ions are very profound. On III/V semiconductor samples, as investigated here, the effects of preferential sputtering are visible but can be mostly neglected for VB offset determination. To reduce the effects further, Zalar rotation[150] is employed. In this procedure the sample is slowly rotated by nearly 360° during the ion bombardment, yielding a very homogeneous and wider sputter crater. This reduces the sputtering defects and ensures that the measurement is not disturbed by higher lying layer of the sample. Additionally, it enhances the depth precision of sputtering, allowing for the measurement of more abrupt interfaces. However, surface defects from ion beam bombardement, altering the measurements are still present. In general, a stronger bombardement, i.e., higher particle acceleration and higher amount of ions, leads to increased effects from defects, amorphous overlayers and ion implants[148,151].

With the possibility of depth profiling it is now possible to use a spectrum at each to monitor the change in the VB edge energy taking into account the above-mentioned limitations. The difference of these energies yields the VB offset between the two materials. The low intensity around and the unclear energy on-set of the VB edge render it necessary to accurately fit the VB edge. There are two possible ways of fitting: an error function (erf) and deriving a Tauc-like[152] intersection point from it, or calculating a density of states function, fold it with a Gaussian broadening function to account for instrumental broadening. The erf method is a great tool to deduce a value from a rather unknown material, where microscopic simulations are not available, yielding a rather coarse estimate. Contrary, the DOS method is more precise and the actually correct method for semiconductors, i.e., for materials in which the DOS changes rapidly around the valence band maximum (VBM) the erf intersection is not sufficient[153]. It should be applied wherever possible, but such calculations are not always available. Non-local pseudopotential methods have been previously employed with great precision to get the DOS around the VBM of a material[154], nowadays standard simulation techniques, such as DFT or $k \cdot p$ are often used to deduce it. For most standard materials, where a sufficient pseudopotential parameter set is available[51], it is possible today to carry out the calculation on a standard office computer. The simulated dataset is then fitted with the relation

$$I(E_B) = S N_{\mathrm{VB}}\left(E_B - E_{\mathrm{VB}}\right) + B \tag{6.5}$$

to the data, where S, B and E_{VB} are fitting parameters and $N_{VB}(E)$ is the Gaussian broadened valence band density of states. The parameter E_{VB} represents the actual VB edge energy. However, DOS data is not always available for new materials and simulation is not only possible in every case, due to missing material parameters or special cases. Therefore, the erf method is a good first estimate for such cases. To get a

VBM value from it, the intersection of the tangential slope in the turning point of the erf and the zero line is calculated. Assuming an erf fit of the form

$$I(E_B) = \frac{a_0}{2}\,\mathrm{erf}\left(\frac{E_B - a_1}{a_2}\right) + a_3, \tag{6.6}$$

where E_B is the binding energy, I is the photoelectron intensity and the a_x are fitting parameters. From Eq. 6.6 the tangential line

$$I(E_B) = \frac{a_0}{2a_2}E_B + a_3 - \frac{a_0}{2a_2}a_1 \tag{6.7}$$

is derived by differentiation and calculation of the axis intercept. The intersection with the zero line at $a_3 - \frac{a_0}{2}$ yields the VBM position

$$E_{\mathrm{VB}} = a_1 - a_2. \tag{6.8}$$

It solely depends on the fitting parameters and its value and errors can completely be determined from the erf fit.

With the sputtering technique and fitting procedures at hand, it now seems possible to deduce a band offset with high precision. The fitting is simple applied to the different spectra throughout the depth range, achieved by sputtering. Through statistical averaging and thoroughly monitoring the interface, the offset could be calculated. Albeit, due to different surface charges the offsets for non-conducting samples are shifted, because the Fermi energy of sample and spectrometer are not connected in this case. Typically, they are corrected with the C 1s orbital, as it is present on virtually any surface. A better method, however, would not rely on the relation between spectrometer and material work functions, but only the difference between the work function of the interfacing materials. Kraut et al.[155] came up with a simple method to put only these two materials into relation: not only the difference of VBM is calculated, but also the difference of a certain CL. If the two materials forming the interface are compounds and have an element in common as one as their constituents, a difference between a specific CL signal in material A and B can be used to measure the change of work function. Albeit, this only works under the assumption, that the CL is not affected much by the different chemical surroundings in the different materials, it does not detract from the general power of the method, because CLs are virtually never altered by their chemical surroundings for materials with sufficiently filled electron orbitals. Since the method is applied to III/V semiconductors, here, it is safe to take this assumption for granted. However, if the two materials do not share the same element, one CL signal for each material is chosen and their aligned by their energy difference at the interface. Therefore, it is crucial to hit the interface directly, such that both of the signals are present. With this interface states, the VB offset is calculated to

$$\Delta E_{\mathrm{VB}} = \left(E^B_{\mathrm{CL}} - E^B_{\mathrm{VB}}\right) - \left(E^A_{\mathrm{CL}} - E^A_{\mathrm{VB}}\right) - \left(E^B_{\mathrm{CL,\,int.}} - E^A_{\mathrm{CL,\,int.}}\right) \tag{6.9}$$

for an offset in the direction of material $B \rightarrow A$. Here, core levels, valence band edges and interface states are denoted with the subscripts CL, VB, and int, respectively.

This general procedure allows for the measurement of any band offset directly. The directness of the method is a clear advantage over PL based methods, which only deliver the transition energies of the active material. However, the accuracy of the method is quite limited due to the weak signals around the VB edge. The edge fitting error mainly

contributes to the complete offset error, which can be as great as 0.5 eV. Albeit, this is fairly good considering the energy resolution of a XPS system (~0.1 eV), it is a rather poor estimate for most semiconductor offsets. These offsets are often well below 1 eV. Therefore, the actual offset can vanish in the error bars of the measurement. To improve the measurement precision an UV light source instead of an X-ray source can be used for photoelectron emission. The UV light has a stronger cross-section with VB states and the detection of lower energetically electrons is more precise. Typically, a He lamp is used for UV light generation, which generates 40.81 eV (He II) and 21.22 eV (He I) lines.

With this excitation source, the method is a complete tool to tackle band offset measurements with great precision (UV resolution around 30 meV). In Sec. 7.2 the method will be applied to the Ga(NAsP)/GaP/Si heterostructure to determine the offset between each of its interfaces.

7 | Hetero-Offsets in Ga(N,As,P) Structures

In the following chapter band-offset measurements at the Ga(N,As,P)/GaP and GaP/Si interface are presented. The band-offset is an important measure for the performance of any device based on semiconductor heterostructures, e.g., diodes, transistors, and lasers. It is crucial in the efficiency of electron capture inside the quantum well and for the waveguiding properties in terms of optical confinement. Here, two methods are used to deduce the material band-offset: PLE as an optical method and PES as an electron spectroscopy method. The first is an indirect method, which uses three theoretical models to account for different shift contributions. The latter method, in contrast, is a direct method where the electrons at the valence band edge are directly measured by photoemission.

7.1 Indirect Measurements by Photoluminescence Excitation Spectroscopy

The excitation bandwidth of the PLE spans a broad range from 1.24 eV to 3.1 eV. This broad range makes it not only possible to investigate electronic states near the band-gap resonance, but also higher lying interactions, e.g., channels from different layers into the active region. In fact, three different recombination regions can be identified throughout the PLE spectrum of the Ga(NAsP) heterostructures (Fig. 7.1). The energetically highest contribution arises from absorption in the GaP X-band and scattering into the active region (Fig. 7.1 *GaP region*). Accordingly, a peak around 2.26 eV (band-gap of GaP) is seen. The second contribution between 1.8 eV and 2.0 eV is a more complex diffusion term from the in-plane dispersion of the active material into the GaP X-band. This diffusion term will be explained later in more detail. The last region seen in the spectrum has the lowest energy and lies near the actual on-set energy of the PL. It shows two resonances which arise from lh and hh to first electronic state, e_1, recombination inside the quantum well.

The deduction of the band-offset will completely be based on the hh/lh resonances in the lower energy region. Therefore, the graphs and considerations in this section will mainly show and deal with this spectral region. In addition, a discussion of the diffusion contribution in the mid-energetically excitation region (~1.8 eV) will be given at the end of this chapter.

As already mentioned, PLE as an optical method is tied to be an indirect measure of the band-offset. For a resilient measurement of the band-offset, a sample series of increasing quantum well width is used[156]. The increase induces a shift of on-set energy, as well as splitting of the hh and lh resonances. Obviously, the on-set energy scales with d^2, according to the general solution to a one dimensional particle in a box, where d is the well thickness. This condition is well fulfilled for the investigated sample series (Fig. 7.2). The layer thicknesses are determined by XRD and transmission electron microscopy (TEM) (circles and squares in Fig. 7.2).

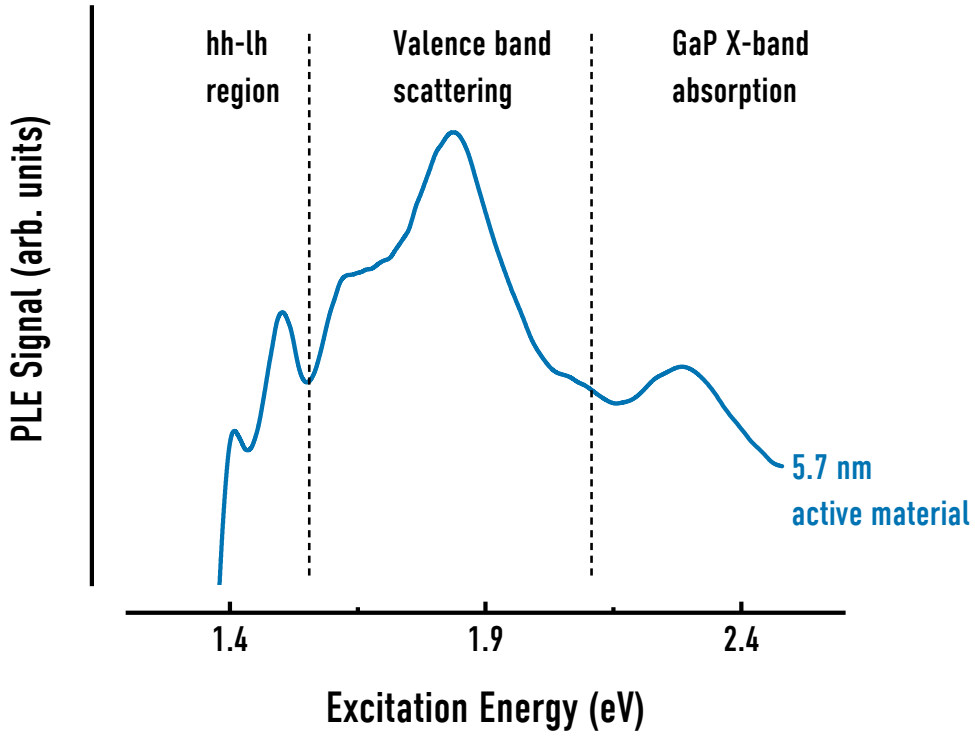

Figure 7.1: Full PLE spectrum of a 5.7 nm thick Ga(NAsP) sample. The spectrum has three different sections: the low energy region, where the hh and lh features are visible. The mid region, where valence band scattering terms contribute to a rise in intensity and the high energy part, where electrons are lifted in the GaP X-band.

The splitting of hh and lh resonances increases with increasing well width (Fig. 7.3). This correlation validates that the peaks actually arise from the hh / lh $\rightarrow e_1$ transition. In contrast, if transitions into higher electronic states have taken place, the gap between the resonances would decrease with increasing thickness. Moreover, the Stokes-like shift between PL and PLE and the full-width-half-maximum (FWHM) of the PL decrease with increasing well-width. This indicates that the influence of disorder is more prominent in thinner samples. Apparently, the relative interface disorder states are more pronounced in a thinner sample due to the volume ratio between disordered interface and material unaffected from disorder[156]. As a consequence, care has to be taken here not to introduce systematic errors due to differing disorder tails of the samples. Therefore, the samples are evaluated carefully, i.e., the peak positions are checked relative to the integration region (shaded area in the PL in Fig. 7.3). Additionally, the energy difference between the PL maximum and the high energy integration threshold is kept constant to observe mainly equally deep local disorder potentials.

To deduce the exact energy of the peaks they are least square fitted with Gaussian functions. This yields two transition energies for each sample.

The experimental data is compared to results from a model calculation considering three main effects: VCA, BAC and conduction and valence band shifts. The valence

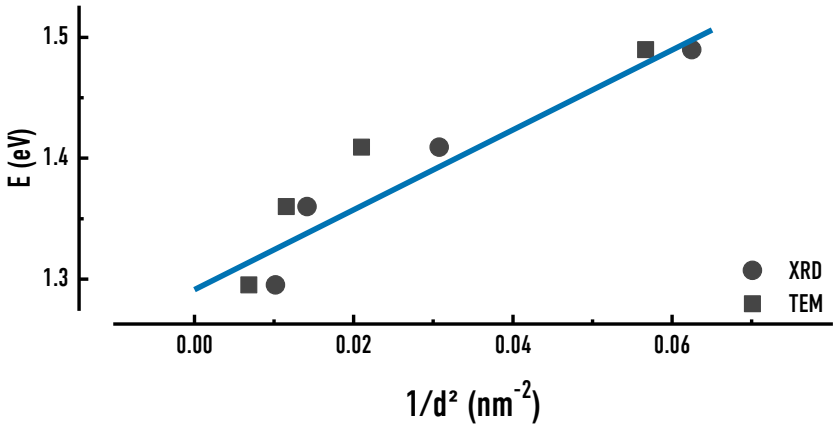

Figure 7.2: Absorption edge for the samples in dependence of their inverse squared thickness. Thicknesses are either determined by XRD (circles) or TEM (squares).

band shifts are described by the model solid theory (MST) from which the hh and lh shifts ΔE_{hh} and ΔE_{lh} are extracted:

$$\Delta E_{hh} = -\delta E_h - \delta E_s \tag{7.1a}$$

$$\Delta E_{lh} = -\delta E_h - \frac{1}{2}\Delta_0 + \frac{1}{2}\delta E_s + Q \tag{7.1b}$$

$$Q = \frac{1}{2}\sqrt{\Delta_0^2 + 2\cdot\Delta_0\delta E_s + 9\delta E_s^2}, \tag{7.1c}$$

where $\delta E_x (x = h, s)$ are contributions due to hydrostatic (h) and shear (s) strain and Δ_0 is the spin-orbit splitting energy. Additionally, hydrostatic strain effects are included in the shift of the conduction band[143]. Often, the hh-lh-splitting is treated in the approximation $\Delta E_{hh} - \Delta E_{lh} \approx -2\delta E_s$, for $\delta E_s \ll \Delta_0$[157]. However, this is a low nitrogen content approximation which is not sufficient here ($x_n = 7.5\%, x_p = 15\%$). For a nitrogen content as in the present sample series, we rather get the relation $\Delta_0 \approx 3.5\delta E_s$. These shifts are employed in combination with the quantum well confinement and VCA of the contributing species. The complete set of crystal parameters used is given in Tab. A.1 in the appendix.

Accordingly, the only free parameter is the valence band offset, which is now used as a fitting parameter to the data. The smaller the VB offset is, the smaller is the hh/lh splitting. With this splitting trend the intersection between calculation and measurement is found (Fig. 7.4). From this point, the offset for each sample is determined (Fig. 7.4 right side).

Generally, the offset is constant across different thicknesses. Accordingly, the sample series for which only the thickness changes can be treated similarly. These size-dependent transition energies can be used to deduce the offset energy with great precision. To model this the combined theory of MST, BAC and quantum well approximation is used to calculate the ground level energies of electron and holes (Fig. 7.5). The differences of these different ground level energies yield the transition energies for hh and lh, respectively. Moreover, the only free parameter - the band offset - fits these ground level energies to the measured transition energies. This yields an offset of 120(50) meV for the given concentration of 7.5% nitrogen and 15% phosphorous.

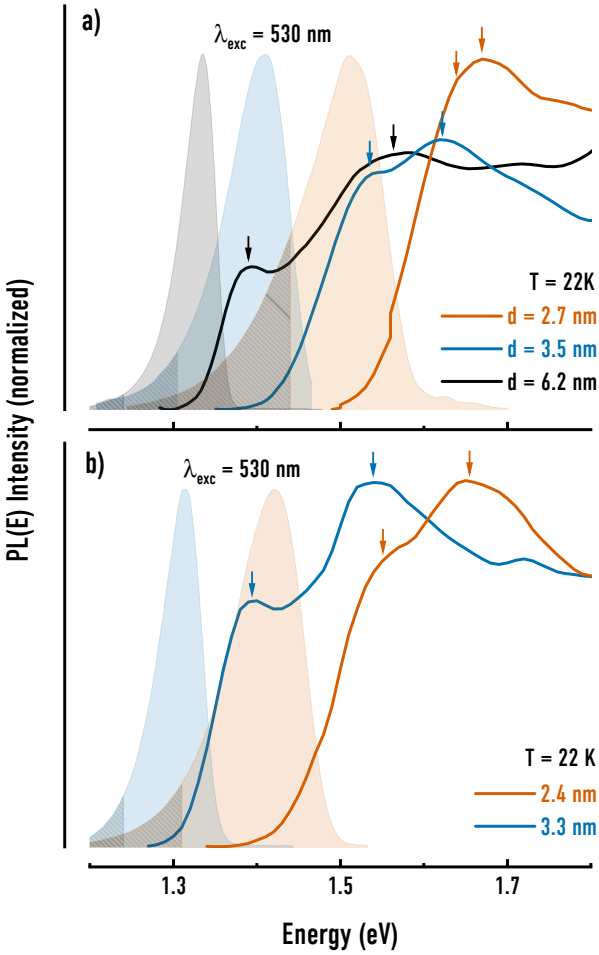

Figure 7.3: PL and PLE spectra for three different Ga(N,As,P) quantum wells (top graph) and for two Ga(NAs) samples (bottom). The shaded areas depict the integration region for the PLE and the arrows indicate the hh and lh transition peaks.

Figure 7.5 shows the comparison of the experimental data and the calculated levels from theory. The experimental data is summed up with the fitting hole level, such that an easy comparison with the electron level is possible. Overall, the agreement is very good. However, the error bars on the offset value is rather high since the transition energy is not strongly affected by low changes in this parameter. This is due to the relatively low valence band offset in comparison to the general offset to the GaP layer. The valence band to band gap ratio is 94 % for the composition here. Accordingly, nearly all of the band gap change is in the conduction band. Forming rather deep wells for the electrons, i.e., they are strongly confined inside the active layer. On the other hand, the material is not deeply trapping the holes. Therefore, coming to lasing and recombination processes, out scattering of holes may lower the effective wave function overlap, decreasing the overall emission efficiency.

As already mentioned in the beginning, there is a resonance at 1.8 eV in the PLE spectrum. This resonance is attributed to a diffusion of holes from the in-plane dispersion in the active material into the GaP X-band. The dispersion of the active material surpasses the valence band edge of GaP beyond a critical energy, allowing the holes to scatter out

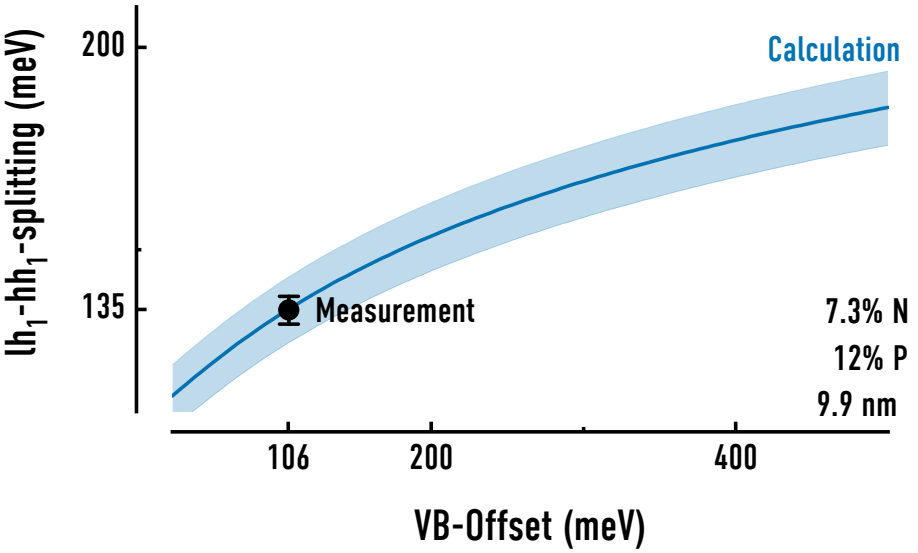

Figure 7.4: Example of the fitting procedure for the thickest sample. The hh-lh splitting is calculated in dependence of the valence band offset. From this relation the offset for a given splitting can be deduced.

of the active layer. Further, the hh and lh bands are shifted due to many effects: the confinement, alloy concentrations, and inherent strain in the sample. This gives rise to complex band interactions, which may lead to anti-crossing of the valence bands for higher k values, in turn shifting this resonance. Moreover, the local nitrogen centers may arrange in clusters, giving rise to scattering centers into higher conduction band levels, thus enhancing the emission intensity. However, the full understanding of the higher energy resonances remains unclear and further investigation in combination with a fully theoretical understanding are part of future projects on this system.

Accordingly, microscopic simulations are necessary to validate this theory. For this reason, DFT simulations are applied with an approach to model band offsets with great precision[158]. In this model, the known uncertainties in the energies calculated with DFT are ruled out by an alignment of the core levels of the participating atoms. However, this restrains the method to be applicable only to interface in which both of the sides contain the same atomic species. In this case, the microscopic structure and semiconductor bands are calculated for each material separately, as well as the CLs of the two atomic species. If these two energies differ their difference is a unique tool to align the overall energy of the two calculations. In such case the same atomic level energy (e.g., of the 1s orbital) of the atoms inside the bulk structure (i.e., under the assumption that they are not affected by the interface) are set to the same value. It is assumed that the core level is not affected by the band structure, which is true for many semiconductors. Moreover, the method approximates implicitly that the full wave function for the complete structure is represented by two separate wave function of each material. With these simplifications in mind, the band offset can be readily extracted.

Applying this method to the Ga(N,As,P)/GaP interface one finds a much greater offset of 430(20) meV (for $x_n = 7.8\,\%$ and $x_P = 10.9\,\%$) compared to the experiment. Nevertheless, the method is capable of reproducing similar materials, such as Ga(As,Sb)/-GaAs/Ga(In,As) type II systems very well[159]. Moreover, the discrepancy cannot be

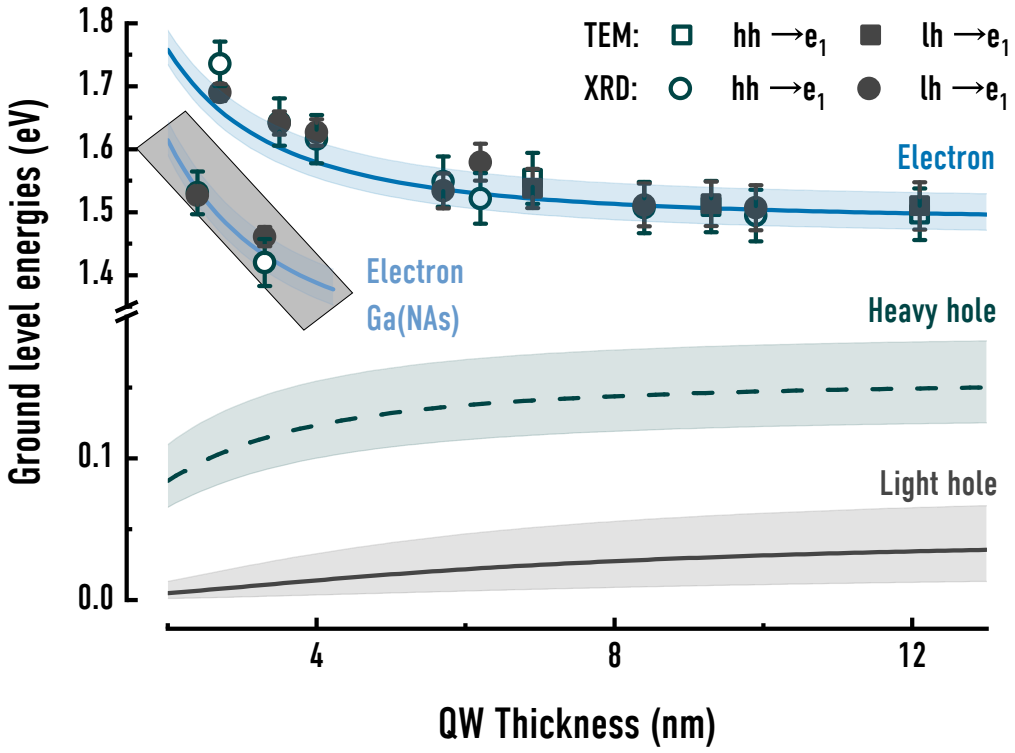

Figure 7.5: Ground level energies with respect to the GaP valence band edge. The lines depict the calculated values from the model and the shaded area their error. Circles and squares are the measured transitions, added to their respective lh (grey) or hh (green) energy. The thicknesses are either determined by XRD (circles) or TEM (squares).

explained by compositional variation or different site positions of the nitrogen atoms. The overall error due to these uncertainties into account is in the order of few tens of meV. Therefore, this cannot be the source of this deviation.

Another possible cause is that the MST fails for this quaternary diluted nitride material. As nitrogen incorporation is often known to produce unpredictable results, it is possible that the perturbation band shifts the interface in such manner that the strain correction cannot be applied correctly. Nevertheless, the questions cannot be answered by the DFT simulation and PLE experiment alone. Another method to directly measure the band offset is XPS, which is applied to the material to get a direct measurement of the offset.

7.2 Direct Measurements by Photoelectron Excitation

The method outlined in the following chapter was first described by Kraut et al.[155]. It is very similar to the process happening in the DFT alignment method described above: the core levels of the material are measured to correct the valence band measurement and to align for different surface work functions of the materials. Importantly, the valence band edges are measured directly and without any additional theoretical assumptions the

valence band offset is determined. Unfortunately, the kinetic energy of the photoelectrons is rather high in the valence band regime. The absorbed X-ray energy is nearly fully converted into the kinetic energy, due to the very low binding energy of maximally a few eV. Since the energy resolution of the hemispheric detector scales approximately with the energy of the electrons, the system is operated at its detection limit and the spectral resolution is lowest. However, the spectral resolution is crucial for these experiments, as the edge position is either determined by a Gaussian error function fit or DOS fit. This is pointed out in more detail in Sec. 6.2. Due to these uncertainties, all CLs and VB fit permutations are evaluated separately and their instrumental weighted mean is calculated to derive a resilient offset value.

This approach is applied for all of the interfaces in the Ga(N,As,P) heterostructure. Firstly, the GaP/Si offset is calculated for benchmarking the method and to compare the material to literature values. Secondly, the Ga(N,As,P)/GaP VB offset is derived with the exact same method. The last part is a deduction of the (B,Ga)(As,P)/GaP offset and considerations if there is any measurable offset at all.

7.2.1 GaP/Si Offset

The offset is measured on the *27152* sample (see Ch. 5 for details). Accordingly, the (B,Ga)(As,P) material is sputtered completely prior to the measurement of the interface of interest. From this run, the sputter rates for the barrier materials of the Ga(N,As,P) quantum well is obtained. The sputter process is carried out with an Ar^+ acceleration voltage of 2 kV and a current of 1.9 A after a surface cleaning step with a low voltage (0.2 kV). Every 30 s a complete overview spectrum from 0 V to 1400 V and detail spectra of the species of interest is taken.

Most of the photoelectron signals are expected to arise in the 0 eV to 200 eV region of the spectrum, except Ga 2p signals around 1100 eV are on the opposite end of the spectral region. The narrowness of emission energies constrains the measurement depth of the signals, given by the IMFP to energy relation[147]. For a detected binding energy of around 200 eV, i.e., a kinetic energy of around 1300 eV (simply related by Koopmans theorem and Einstein equation), the electrons have an IMFPs of 3.6 nm. This means that 95 % of the signals stems from approximately 10 nm of the samples surface, which is around 20 atomic layers. Accordingly, the approximately same sampling depth for most of the signals, as well as the valence band edge are applied throughout the measurement. Contrarily, for the only outlier - Ga 2p - 95 % of emission comes from a depth of 5 nm or ten atomic layers.

For both, GaP and (B,Ga)(As,P) predominantly Ga and P lines are seen and the overview spectra are very similar (Fig. 7.6 bottom). Unfortunately, an exact interface measurement needs a clear indicator in terms of a testing probe for interface transitions. Luckily, the (B,Ga)(As,P) spectrum shows a small deviation compared to the GaP spectrum, which is a small As Auger peak around 250 eV (Fig. 7.6). In detailed spectra, the As 3d around 40 eV peak is observed, too. Therefore, the vanishing of the As 3d peak indicates the transition from the (B,Ga)(As,P) to the GaP layer (Fig. 7.7). The sputter time in between the visibility and vanishing of the As 3d peak and the thickness determined by XRD measurements yields a sputter rate of 0.211 85 nm/s for the (B,Ga)(As,P) layer with a concentration of 4.1 % B and 6 % As. The distinction of the actual GaP/Si interface is lesser painful: a smooth transition in the energy range around 100 eV is visible and

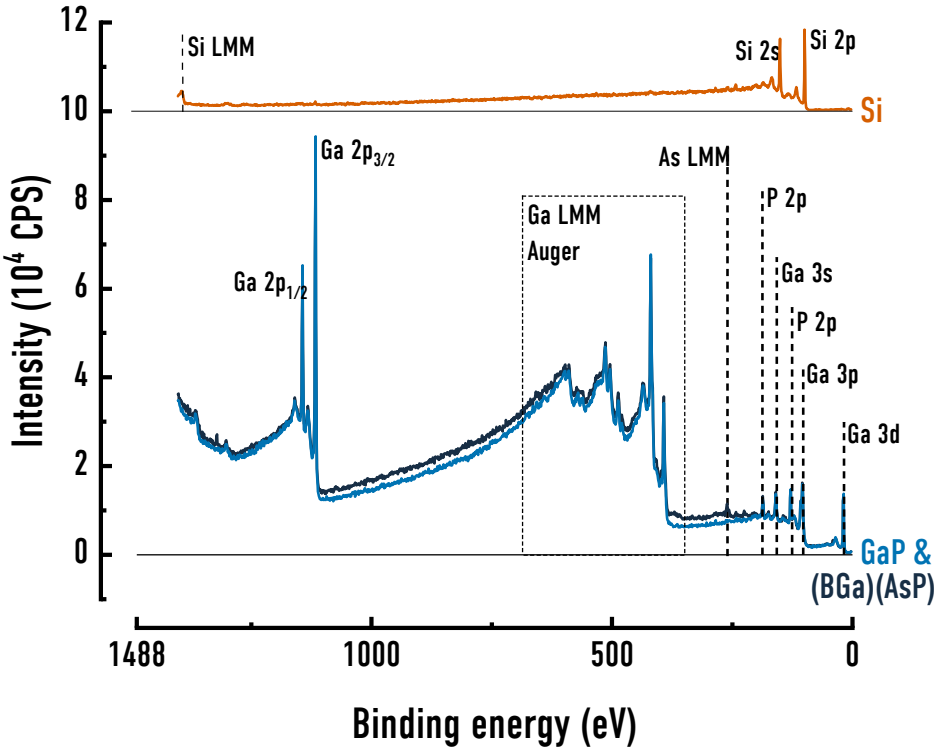

Figure 7.6: Overview spectrum of Si, GaP and (BGa)(AsP). The corresponding orbitals are denoted with dashed lines. The Si spectrum has an offset of $10 \cdot 10^4 CPS$ for clarity.

an overall change of the overview spectrum (Fig. 7.6 top). Here, the Si 2p peak rises besides the double featured peak of Ga 3p, allowing for exact monitoring of the transition and good observation of shifts. Figure 7.8 shows an example of the transition from GaP bulk, over the interface to Si bulk and the corresponding shifts. Although, shifts between the materials are rather small, they are crucial as they are used to correct for the work function of each of the materials. Accordingly, the right choice of CL peaks is very important. Therefore, all different combinations of Ga, P, and Si CL positions are evaluated and compared to each other. The CL positions are determined by fitting a Voigt line shape (30 % gaussian) with a Shirley baseline to the data (see Sec. 6.2 for further details)

The valence band edge is fitted as well. This is done in two ways as stated in Sec. 6.2: either by fitting an error function or a theoretical/literature Gaussian broadened density of states function to the data. For comparison, both fits are carried out for Si (Fig. 7.9) and GaP (Fig. 7.10), indicated by an orange line and a red line for the error function fit and the VB DOS fit, respectively. It turns out, that there are significant deviations between these two fits in the order of 0.1 eV to 0.2 eV. Yet, for Si it yields a significantly different value somewhere in the seventh to eight σ interval. Nevertheless, the different CL to VB differences will be calculated for both of the fits. However, since the VB DOS fitting approach should yield more accurate values for semiconductors[153], it is used for the determination of the band offsets. Moreover, the error function fitting approach is mostly deemed to fail in the case of a fast varying DOS around the VB

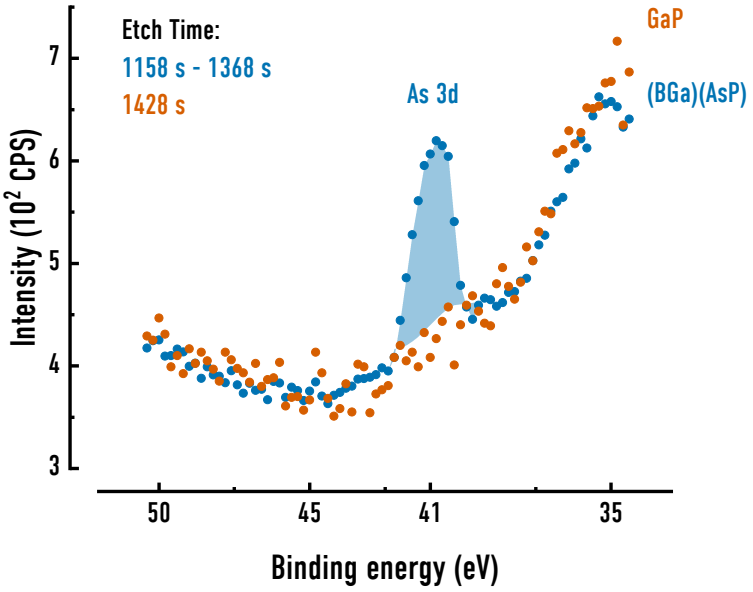

Figure 7.7: Vanishing of the As 3d peak between the GaP (orange) and (BGa)(AsP) layer (blue).

Table 7.1: Comparison of core level to valence band difference between experiment and literature.

Orbital	Experiment / eV	Literature / eV	Source
Si 2p	99.40 ± 0.03	98.95 ± 0.04	Yu et al.[162]
Ga 3d	19.16 ± 0.19	18.81 ± 0.02	Kraut et al.[155]
As 3d	41.44 ± 0.10	40.73 ± 0.02	Kraut et al.[155]

edge[153]. Therefore, theoretical or experimental literature values for the DOS for Si and GaP are needed. Papaconstantopoulos[160] has broad calculations by means of the non-local pseudopotential method[154] (which is also applied by Kraut et al.[153] and is known to yield accurate VB edges) for all elemental materials. This reference gives a DOS for Si, which produces an excellent fit to the experimental data. Unfortunately, for GaP the situation is less clear. Here, a XPS study[161] and a non-local pseudopotential calculation[154] are available. Surprisingly, the simulation yields a far better fit to the data, since the measurement as well as the simulation is lacking a very long tail below the VB edge present in the study of Shevchik et al.[161]. The theory shows a much steeper edge at the VB onset in comparison to the XPS literature curve. It is possible that the XPS study suffers strong Gaussian broadening which is not present in our measurement due to better resolution available nowadays. As a consequence, the theory compares much better to the present measurement and therefore it is used to extract the VB edge. Consequently, the calculated CL to VB edge values for different atomic species are stated in Tab. 7.1 and compared to literature.

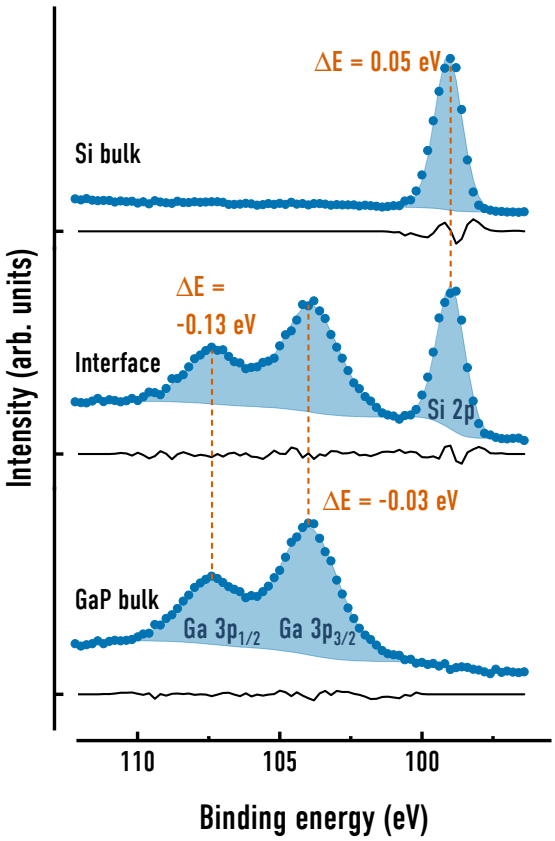

Figure 7.8: Transition from the Ga 3p core level feature to Si 2p across the interface between GaP and Si. The orange lines and ΔE values depict the peak shift along the interface (change from bottom to top). Below each graph the fit (blue shaded area) residuals are given (black lines).

Finally, after CL position are fitted, compared, and the VB edge position is extracted it would now be possible to deduce offset values, however, any significant drifts in any of the energy values have to be avoided. To solve this issue, the differences of the interface CL energy to any other depth position is calculated and plotted over etching depth (open circles in Fig. 7.11). For comparison, the VB edge energy is plotted as well (filled circles in Fig. 7.11). Three regions can be separated in Fig. 7.11, each one representing one of the layered materials. The core level energy in the GaP regime is constant, despite the slight drift observed in the (B,Ga)(As,P) layer for both of the Ga orbitals (2p and 3p, as well as their spin splittings). However, two major features are found at the GaP/Si interface: a strong change in the VB edge energy and a rapid change of GaP and Si core level energies. The rapid change shows the importance of the relative energy alignment for non-conducting samples employed in this method. Notably, there is a slight shift of the Si energy in dependence of edging depth in Fig. 7.11. It is well below 0.1 eV and is treated as standard deviation of the bulk mean value of the Si energy in the following. Still, this effect may be important considering the prospecting value of the band offset, which is in the order of magnitude of several hundreds of meVs, too.

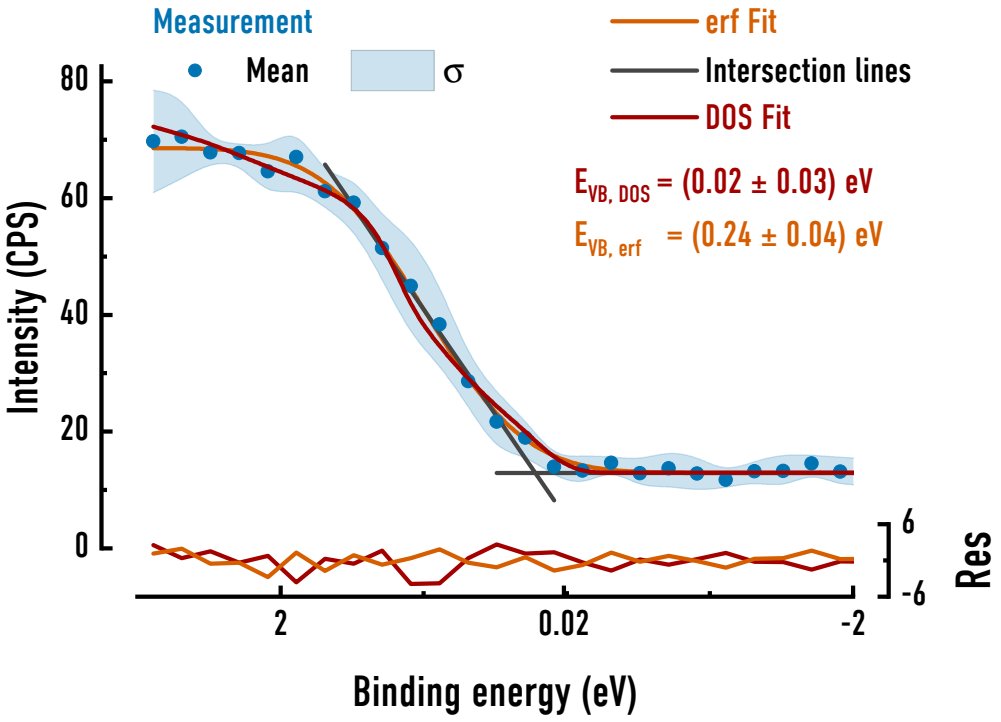

Figure 7.9: Valence band edge fit for Si, with either a theoretical DOS (red) or an erf (orange). Below, the residuals are shown in the same color. The data are averaged over an appropriate depth, during which the material was present in the measurement.

The CL to VB difference is a useful quantity to compare the data with literature. It stays constant throughout measurements, as the difference eliminates the spectrometer work function distorting each of the CL or VB energies. Table 7.1 shows the difference for three selected orbitals. The experimental and literature values are comparable in their uncertainty. The agreement is rather good considering the chemical shift of the CL orbitals due to different compositions compared to literature and the low resolution of XPS at the VB edge.

The instrumental weight of all of the CLs and VB energy combinations reduces the overall uncertainty. The final offset at the Si/GaP interface is then given according to

$$E_{VB,Si/GaP} = 0.22(5)\,\text{meV} \tag{7.2}$$

7.2.2 (BGa)(AsP)/GaP Offset

No VB offset is found between the (B,Ga)(As,P) and GaP VBs according to the XPS measurements. Figure 7.12 shows a comparison between the averaged GaP and (B,Ga)(As,P) valence band edge, the As 3d and the Ga $2p_{3/2}$ CL feature. The vanishing As 3d feature (Fig. 7.12c) indicates the presence of the different layers. The indicator constrains the averaging boundaries for the VB and CL features. The form and on-set of the averaged VB edge does not change between the materials (Fig. 7.12a). Additionally, the CLs do not shift (Fig. 7.12b), hence the surface potential stays the same throughout the two layers.

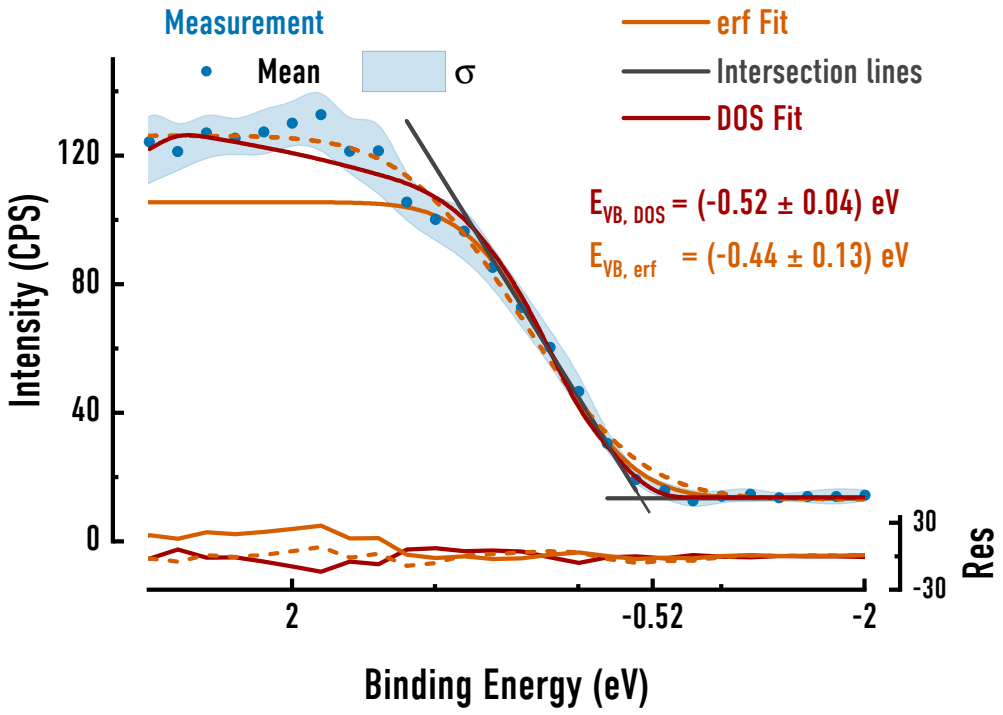

Figure 7.10: Valence band edge fit for GaP, with either a theoretical DOS (red) or an erf (orange). Below, the corresponding residuals are shown in the same color. The data are averaged over an appropriate depth, during which the material was present in the measurement.

As a consequence the valence band offset between (B,Ga)(As,P) and GaP is effectively zero or at least well below the resolution of the measurement. Therefore, the conduction band offset ratio is 100 %. The band gap of (B,Ga)(As,P) is not accurately known, but is estimated from boron and arsenic incorporation. The conduction band edge shifts by $-6.2(2)$ eV per percent boron incorporated. In conjunction with the weaker shift due to As incorporation (-0.19 eV[163]) the band gap shift of ($B_{4\,\%}$,Ga)(As,$_{6\,\%}$P) is roughly 250(10) meV relative to GaP.

7.2.3 Ga(N,As,P)/GaP Offset

The Ga(N,As,P)/GaP offset is deduced similar to the GaP/Si offset. The sample under study is a Ga(N,As,P) multilayer structure with an active layer width of 9.9 nm (26447). An accurate sputtering rate for the barrier material is crucial to actually take data from the thin active layer. The rate is calculated from the measurements on the (B,Ga)(As,P)/-GaP sample of the previous section ($0.21185\,nm/s$ for the $2\,kV$, $1.9\,\mu A$ Ar^+ sputter setting). Again, a pre-measurement cleaning step ($0.2\,kV$, $0.5\,\mu A$ Ar^+) is performed and a low-resolution overview spectrum is recorded. Afterwards, the barrier is sputtered for $348\,s$, which corresponds to approximately $74\,nm$ of (B,Ga)(As,P). The sputtering time is deliberately underestimated due to heating effects of the Ar^+ ion gun, i.e., the longer the gun runs, the more effective it becomes. A following low-energy setting of $1\,kV$

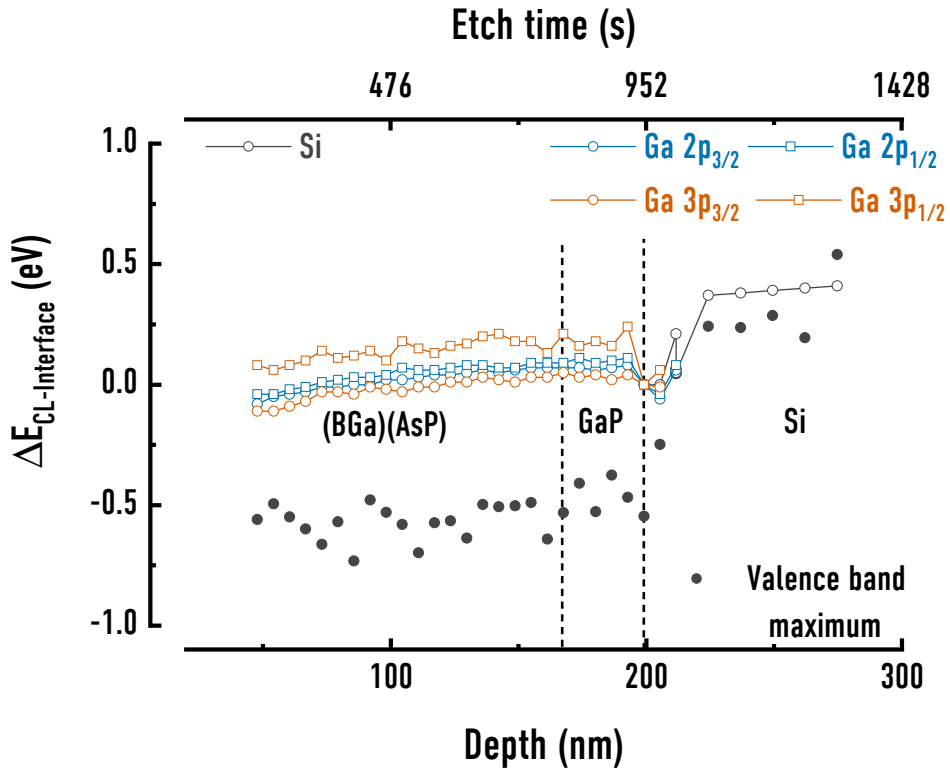

Figure 7.11: Core level shift differences for different Ga orbitals along the (B,Ga)(As,P)/GaP and GaP/Si interface. Each core level energy is shown as the difference to the respective energy at the GaP/Si interface. Additionally, the valence band maximum across the interface is shown (grey dots).

and $0.5\mu A$ allows for a more detailed measurement of the quantum well layer and less sputter-related defects. 34 steps with a sputter time of $30\,s$ each are performed. An overview spectrum from $0 - 1400\,eV$ with a pass energy of $117.4\,eV$ ($20\,ms$ integration time and 3 sweeps) and detailed spectra of the core levels with a pass energy of $23.5\,eV$ ($20\,ms$ integration time and 10 sweeps) are recorded in each step. The pass energy is set to $11.75\,eV$ at the valence band edge and the averaging is raised to 50 sweeps ($20\,ms$ integration time) to account for the lower intensities and resolution present there.

The features of the different layers are very similar, therefore, the indication of the interface is less clear. The boron and nitrogen features would allow for a distinct difference between the different layers. However, they both have very low cross sections and are superimposed by the pronounced Ga Auger lines. Therefore, the detection of the features is not possible and other indicators for the interfaces have to be found. Fortunately, the As and P concentrations differ strongly, such that their intensity change can be used. The arsenic group V ratio lowers from $80.7\,\%$ in the Ga(N,As,P) layer to $0\,\%$ in the GaP and $6\,\%$ in the (B,Ga)(As,P). Accordingly, the P ratio rises from $12\,\%$ to $100\,\%$ and $96\,\%$, respectively. The As feature does not vanish completely in the GaP, since the IMFP is greater than the GaP thickness (4 nm to 5 nm) and can not be separated from the (B,Ga)(As,P) bulk material beneath it. Certainly, the intensity of the As 3d (Fig. 7.14) and P 2s (Fig. 7.13) orbital changes according to the compositional ratio between the layers. The P 2s and As 3d intensity ratios change by a factor of four and eleven, respectively.

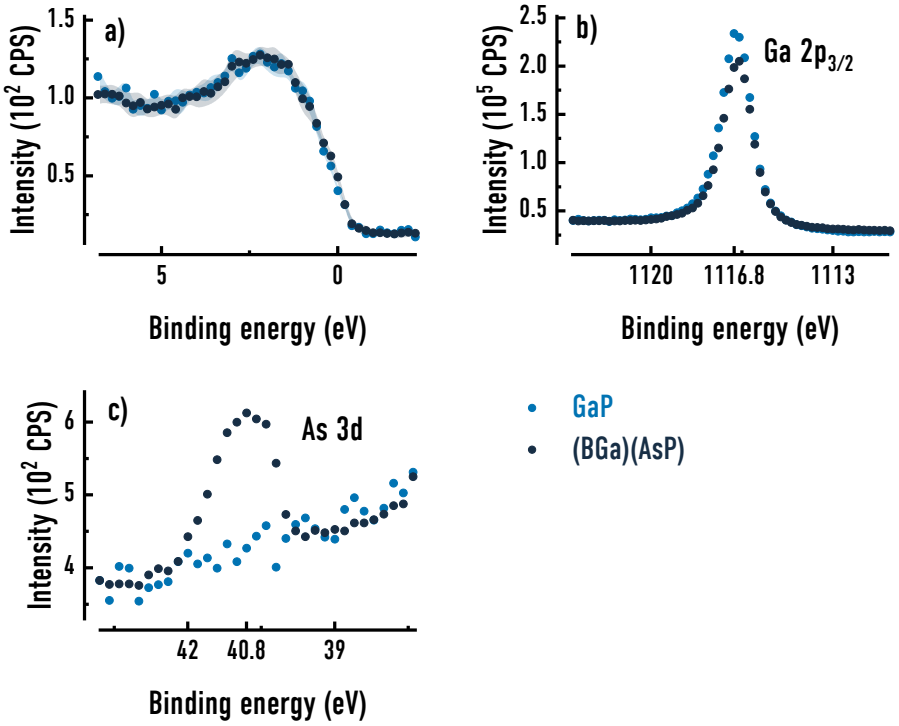

Figure 7.12: Comparison of the valence band edges of the GaP (light blue) and (B,Ga)(As,P) (dark blue) layer (**a**), their Ga $2p_{3/2}$ orbital feature (**b**) and the change of the As 3d feature (**c**).

Approximately, this corresponds to the change of group V ratio in the materials (14 for As and 8 for P). The difference to the exact composition is due to scattering contributions to the background and the features. To extract reliable alloy fractions, all of the contributing atomic orbitals have to be summed up to normalize the fractions to a comparable scale. Unfortunately, this normalization cannot be calculated for Ga(N,As,P) and (B,Ga)(As,P) due to the undetectable N and B peaks. However, this does not hinder the deduction of relative VB and CL positions, since they solely depend on the energies.

In addition to the change of core level intensities the form and position of the valence band edge indicates the change of material clearly (Fig. 7.15). Due to the pronounced contribution of As p-orbitals in Ga(N,As,P) and its bigger cross-section (one order of magnitude compared to phosphorous p-orbitals near the valence band edge[132]) the peak around the binding energy of $2\,eV$ shifts and increases strongly. The $11\,eV$ peak may arise from Ga 4s contributions, which is enhanced in Ga(N,As,P) due to different scattering. However, the orbitals undergo sp^3 hybridization to form the VB, therefore, the attribution of single-atomic energy levels to valence band peaks is generally wrong. Consequently, calculations of the mixing process must be performed, such as non-local pseudopotential methods[154], which reproduce the energies at the valence band quite well[153]. From literature the peaks are attributed to X-point contributions for the features at 2 eV and 6 eV and the Γ-point of the next lower valence band ($11\,eV$) The Ga(N,As,P) VB dataset resembles the form of the GaAs VB edge from literature[154,164]. This is not

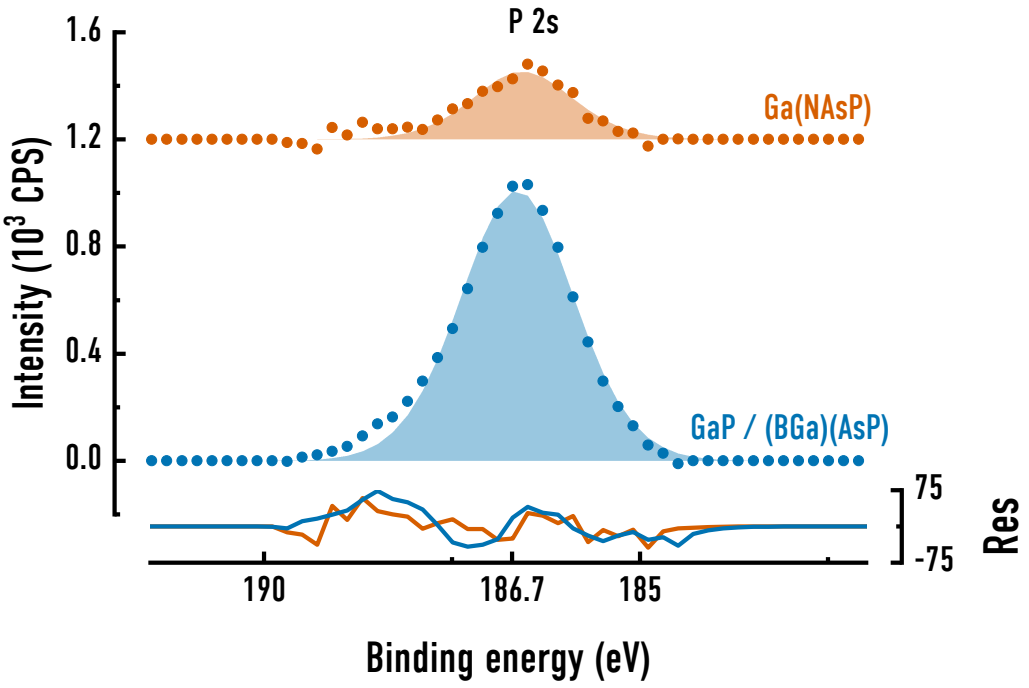

Figure 7.13: Comparison of the P 2s feature in the Ga(N,As,P) (orange) and in the GaP / (B,Ga)(As,P) (blue) layer with their corresponding residuals. The spectra are averaged over the appropriate etch times during which the respective materials are present. The Ga(N,As,P) feature has an offset of 1200 CPS for clarity.

surprising regarding the low cross-sections of N and P orbitals in this energy region, accordingly their contribution at the edge is negligible. For GaP, the weaker contribution of P states to the pDOS, emerging from lower cross-section due to higher photon energies, leads to an altered form of the experimental data compared to literature[154].

Figure 7.16 shows the experimental data (dots) and two fits (lines) to the VB edge. The GaP VB edge is fitted with two approaches: a theoretical valence band DOS[154] fit (red line in Fig. 7.16) and a linearly interpolated erf fit (orange line in Fig. 7.16). The data (blue bullets in Fig. 7.16) is averaged over the etch time during which the material is present, as indicated by the As 3d and P 2s intensity changes. Constraining the erf fit in the interval $-1\,eV$ to $1\,eV$ best reproduces the linear behavior at the rising edge. As a consequence, its value is too low for binding energies above $1\,eV$, which is reasonable, regarding that the erf only takes the instrumental broadening into account. Thus, it does not resemble the lower resonances of the valence band, leading to the underestimation for higher binding energies. It is clear that the erf approach is not fully sufficient to fit the VB edge in semiconductors. Nevertheless, it is a reasonable estimate, as it provides good agreement around the actual VB edge energy, regardlessly. In particular, this approach may be a useful first step if either the pDOS of the material is not known or distorted due to scattering effects. Contrary, the DOS fit suffers from projection related differences, due to varying cross-sections of the orbitals. As a consequence, L-band contributions[154] lead to a pronounced side-peak at around $1\,eV$ for the theoretical DOS in comparison to

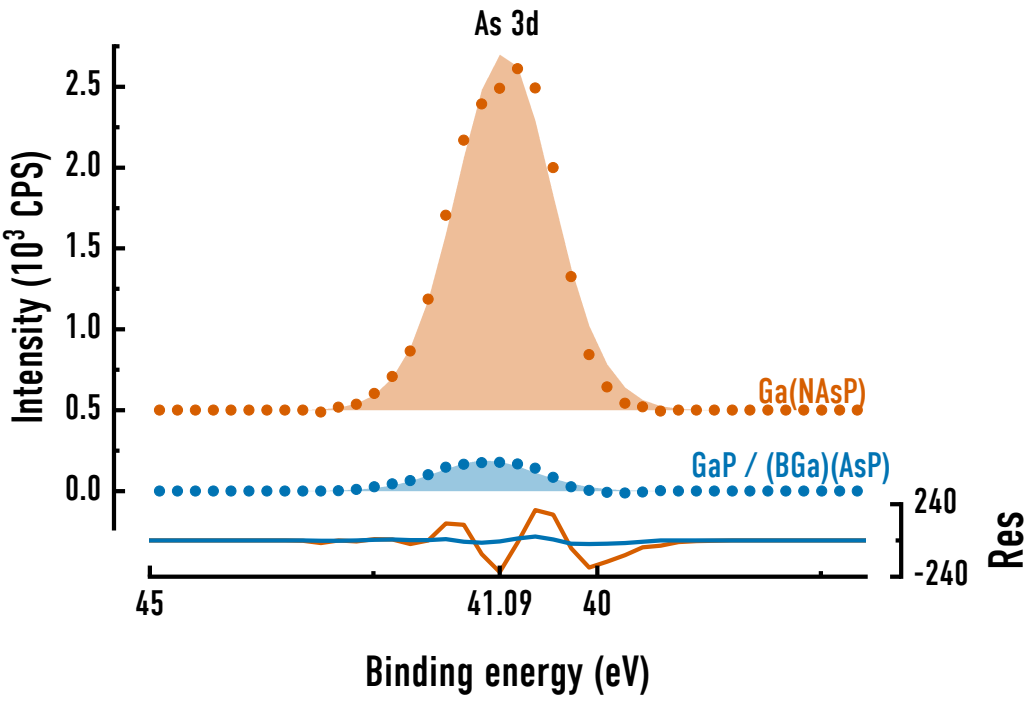

Figure 7.14: Comparison of the averaged As 3d feature in the Ga(N,As,P) (orange) and in the GaP / (B,Ga)(As,P) layer with their corresponding residuals. The Ga(N,As,P) feature has an offset of 500 CPS.

the experimental data. They are less pronounced in the experiment due to less relative phosphorous p-orbital contributions for high photon energies. Yet, the behavior at the edge is in good agreement with the experimental data. The uncorrected valence band energies are then given according to

$$E_{GaP,VB,DOS} = (-0.13 \pm 0.02)\, eV \tag{7.3}$$

$$E_{GaP,VB,erf} = (-0.10 \pm 0.09)\, eV. \tag{7.4}$$

They are not corrected with the surface potential, hence they do not reflect the energy relative to the vacuum level. The energies are equal or at least comparable in their experimental uncertainties, thus the erf approach is appropriate as a first estimate for the material. In the following, both values are used and compared for the VB offset between the materials.

Identical fitting procedures are employed for the Ga(N,As,P) layer (Fig. 7.17) as for the GaP layer. Similarly to GaP, the erf approach underestimates the real intensity above $1\, eV$, due to L-band resonances the instrumental broadening does not reflect. However, the literature GaAs DOS[164] resembles the experimental data well. Therefore, the assumption that the N and P states do not contribute to the measured pDOS is a fairly good approximation for this material. The only significant deviation there from the literature values is found at the on-set around -0.2 eV; theoretical DOS considerations[154] do not show these tail states. Accordingly, the states may arise from various instrument related artifacts: a spread of excitation energies, cross-sections, and, surface states or disorder

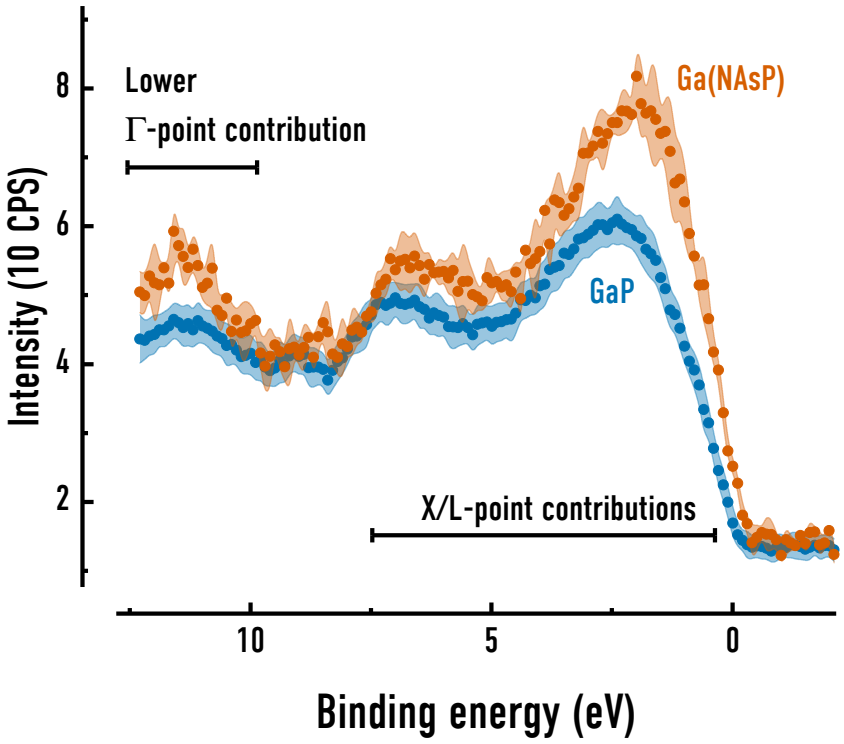

Figure 7.15: Comparison of mean Ga(N,As,P) (orange bullets) and GaP / (B,Ga)(As,P) (blue bullets) valence band signals. The features are averaged over the appropriate etch times, with the shaded area as their standard deviation.

in the system. Here, the broadening and resonance between $1\,eV$ and $2\,eV$ is better reproduced by the XPS literature data, hence, this data is used for the fit. Then, the fits yield the uncorrected valence band positions:

$$E_{Ga(N,As,P),VB,DOS} = (-0.20 \pm 0.02)\,eV \tag{7.5}$$

$$E_{Ga(N,As,P),VB,erf} = (-0.23 \pm 0.13)\,eV. \tag{7.6}$$

The different values are equal or at least comparable, again, rendering the erf fit a useful estimate.

The offset at the Ga(N,As,P)/GaP interface is now determined with these values. Contrary to the GaP/Si offset, no interface CL correction is necessary, because the same atomic species are present in both materials. Thus, only the core level differences between the two layers are taken into account. To enhance the accuracy of the fit, the differences are averaged over the layer depth. Prior, it has to be assured that no significant drifts of the core level energies occur throughout the layer. Figure 7.18 depicts the core level energy difference to their respective interface state over the etching time. Voigt functions are used to fit the core levels to account for the intrinsic lorentzian shape and the instrumental broadening. Here, no reliable depth information is available, since the sputtering rates are unknown, both for the material itself as well as for the particular ion fluxes. Additionally, only one interface of the quantum well was found experimentally during the sputtering cycles. The sputtering rate is approximately equal for each investigated layer and by a factor of six smaller than for the setting used for the

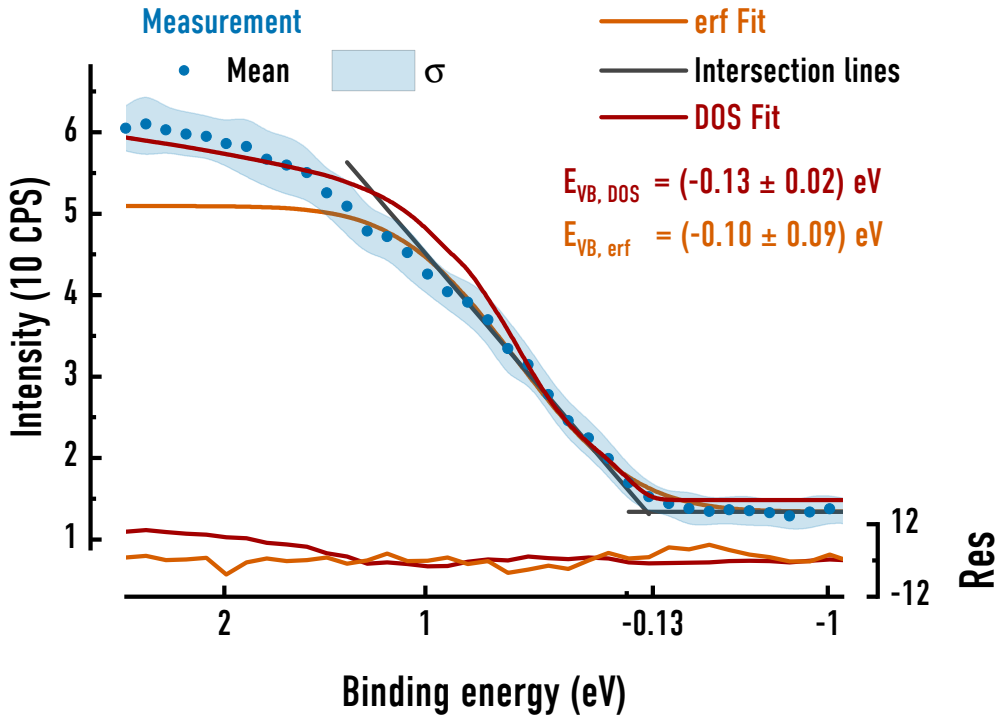

Figure 7.16: Valence band edge of GaP (blue bullets) with DOS (red) and erf (orange) fit averaged over the appropriate etching times during which the material is present. The gray lines are the linear interpolation of the erf fit. The blue shaded area is the standard deviation. The residuals of the fits are given below in the same color. The theoretical GaP DOS is taken from Chelikowsky and Cohen[154].

barriers. This relation yields a rate of $0.035\,nm/s$, thus the total scan-depth in Fig. 7.18 is approximately $30\,nm$. A clear change of core level energies in the Ga(N,As,P) depth region towards the interface is visible (left side in Fig. 7.18). The core level energies stay constant in the barriers, allowing for an averaging over the whole depth of the material. The corresponding uncertainties of the core levels is in the order of $0.01\,eV$ to $0.5\,eV$ depending on the orbital (not shown in Fig. 7.18 for clarity).

Applying the averaged core level energies and into Eqs. 7.3 to 7.6 yields the band offset of Ga(N,As,P) relative to GaP according to

$$\Delta E_V = \left(E_{VB}^{Ga(NAsP)} - E_{CL}^{Ga(NAsP)}\right) - \left(E_{VB}^{GaP} - E_{CL}^{GaP}\right). \tag{7.7}$$

For the DOS fit this yields

$$\Delta E_{VB} = (0.01 \pm 0.15)\,eV, \tag{7.8}$$

and for the erf fit:

$$\Delta E_{VB} = (-0.01 \pm 0.15)\,eV. \tag{7.9}$$

The values are instrumentally weighted over all measured Ga and P 2p core levels. The P 2s and As 3d are not considered due to their very low intensity and, consequently, poor fit quality. The valence band offsets for each orbital are given in Tab. A.2 in the appendix.

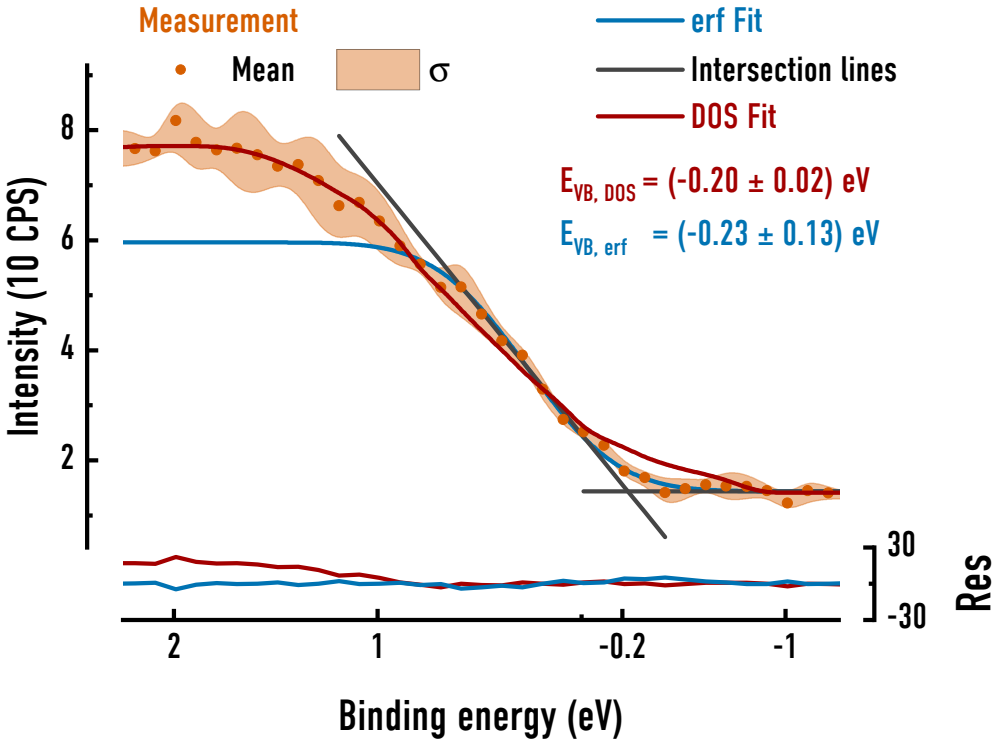

Figure 7.17: Valence band edge of Ga(NAsP) (blue bullets) with DOS (red) and erf (orange) fits averaged over the appropriate etching times during which the material is present. The gray lines are the linear interpolation of the erf fit. The blue shaded area is the standard deviation. The residuals of the fits are given below in the same color. The literature value of the DOS is the GaAs edge from Grobman and Eastman[164].

The confinement in the valence band is very weak according to these values and even of type II character for the outcome of the DOS fit. Notably, both valence band offsets are equal within their uncertainty. The direct statistical uncertainty (as in Tab. A.2) is even lower and has a value of $\pm 0.02\,eV$ for both offsets. However, it contains only the blank statistical fit uncertainties and is therefore regarded as a lower boundary. Accordingly, no fit residuals are taken into account in the propagation of the uncertainty, thus the fit quality is completely neglected. An uncertainty on the order of $100 - 200\,meV$ is found when taking the fit quality into account. Therefore, an average value of 150 meV is used in the uncertainty in Eq. 7.8 and Eq. 7.9.

7.3 Review of the Offsets

This section shortly reviews the band offsets in the Ga(N,As,P) multilayer structure. The valence band offset at the Ga(N,As,P)/GaP interface is deduced by means of XPS and PLE experiments. The PLE approach is indirect, i.e., model considerations are necessary to yield the VB offset. The models include strain in the sample due to the lattice mismatch and subsequent derivation of the strain-induced hh-lh splitting, as well as, the nitrogen BAC models the conduction band shift. A confinement shift is calculated

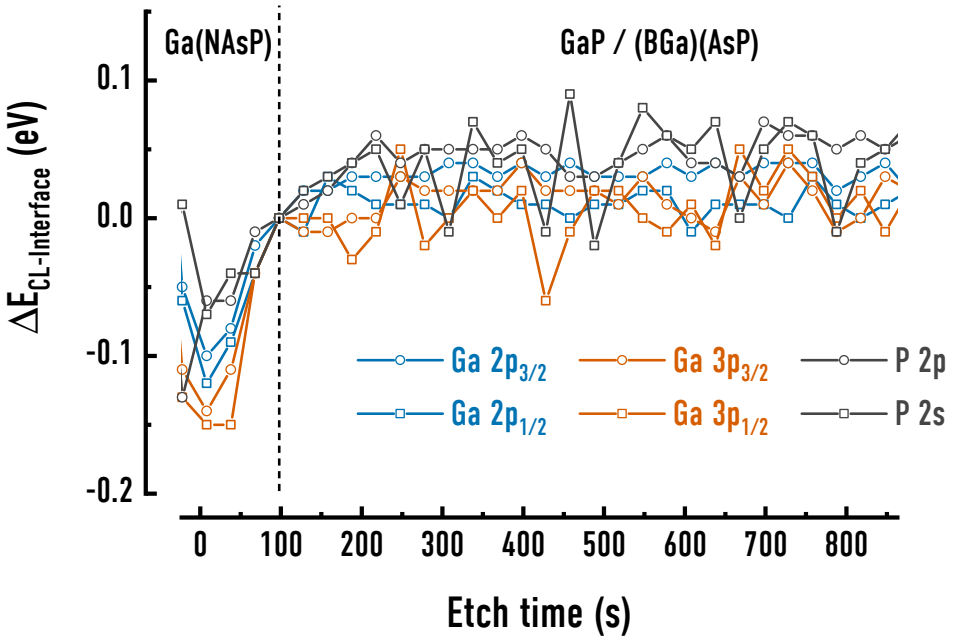

Figure 7.18: Core level shifts with etch time (corresponding to the depth) for different atomic orbitals. The core levels are shown as their difference to their interface value at $\Delta t = 100\,s$.

for all levels and the material parameters are extrapolated by VCA, as they are not fully known for Ga(N,As,P). In summary, the PLE measurements yield a Ga(N,As,P)/GaP offset of 100 meV to 150 meV and a type I alignment of the structure.

Additionally, XPS measurements were carried out to provide complementary and direct, i.e., model free data. However, these are prone to uncertainties due to the low cross-sections for the high excitation energies and poor resolution of the excitation bandwidth. The experimental data yields an VB offset energy of $\pm 0.01\,eV$, depending on the applied fitting method. This suggests an even more shallow quantum well compared to the band offset determined by PLE or even a type-II configuration. Therefore, the underlying confinement model for the PLE results may fail, since the confinement for the hole states is generally in question. PES measurements with lower photon energy would allow for a definitive answer. This will reduce the the spectral resolution to a few tens of meV and allow for more resilient values of this shallow VB offset. This is possible either by using Helium discharge lamps, synchrotron radiation or HHG as excitation source for the PES experiment. Further, the (B,Ga)(As,P)/GaP and GaP/Si offsets are determined by XPS, too. No change in either the core levels energies or the valence band position could be found for (B,Ga)(As,P)/GaP, i.e., there is virtually no or at least low band offset, which is below the resolution of the measurement. The GaP/Si offset is found to be $(0.22 \pm 0.15)\,eV$, hence a type II alignment of GaP and Si is present. Figure 7.19 shows the energy levels across the Ga(N,As,P) heterostructure, with the conduction band levels calculated from the PL transition energies or by VCA.

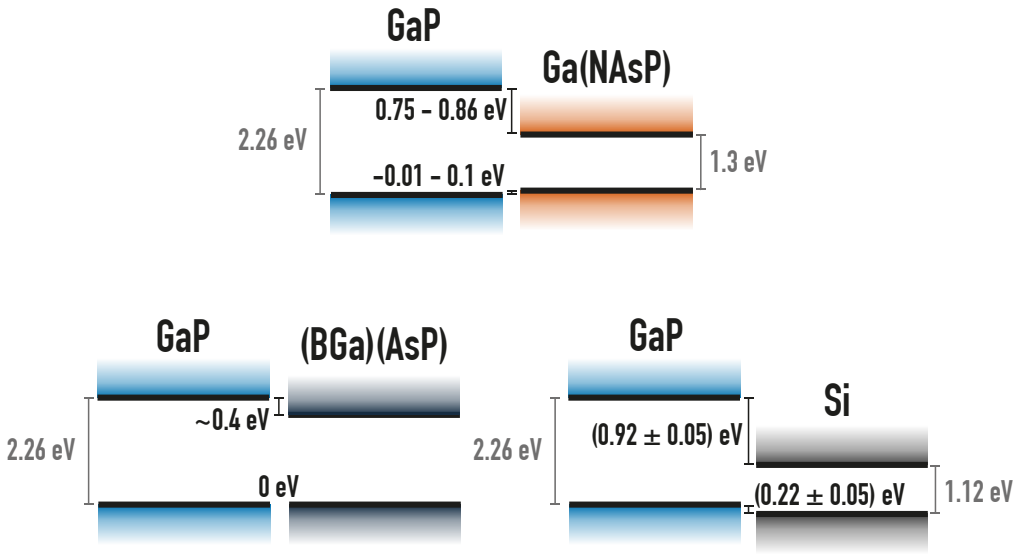

Figure 7.19: Band offsets for the interface in the Ga(NAsP) multilayer structure: the GaP/-Ga(N,As,P) interface (top), the GaP/(B,Ga)(As,P) interface (bottom left) and the GaP/Si interface (bottom right).

For the Si and GaP offset, values between 0.33 eV to 2.26 eV are given in the literature. A type-I alignment is found throughout the literature values (for a good overview see Ostheim[165]). Several effects may cause the large deviations in the literature and the discrepancy to the experimental data. The crystal quality may affect the alignment of the interface[166]. Further, strain of the GaP layer leads to a change of the offset, too[167]. The general influence of APBs, which are present at interface of the investigated sample is unclear[104]. After a growth of a certain thickness (i.e., 40 nm) the GaP layer is defect free, but the interface itself is still defect related. A slow change of the offset should be visible throughout the depth scan of the GaP layer in the XPS measurements. Such shift is not seen for different depths; hence, a gradient effect towards the interface seems unlikely. Investigations by UPS are already planned and have the potential to clarify the behavior for the material.

II

Nonlinear Effects

8 | Materials

8.1 $KNbO_3$

Potassium niobate ($KNbO_3$) is an oxide perovskite crystal exhibiting strong optical nonlinearities. Its second-order susceptibility is in the order of 10 to $20\,pm/V$ at $1064\,nm$ and thus, is fairly high compared to other common frequency conversion materials, such as BBO ($2.2\,pm/V$), LBO ($0.85\,pm/V$) or KTP ($14.6\,pm/V$)[168]. Thus, it is a strong frequency converter similar to $LiNbO_3$, which is often used in frequency conversion systems (i.e., frequency doublers and triplers).

The material shows four different crystal symmetries depending on temperature. Above $430\,°C$, potassium niobate is cubic, below until $200\,°C$ it shows a tetragonal structure. From $200\,°C$ to $-\,50\,°C$ (i.e., at room temperature) it has an orthorombic phase and for lower temperatures the crystal habit is rhombohedral. These phase transition are for temperature lowering, for a rising temperature the system changes at $10\,°C$, $216\,°C$ and $435\,°C$ from rhombohedral, orthorombic, tetragonal to cubic, respectively[169]. Figure 8.1 depicts the unit cell of the orthrombic phase. The room temperature lattice constants are $a = 5.697\,Å, b = 3.971\,Å$ and $c = 5.722\,Å$[169]. Further, it is a negative biaxial crystal showing three different refractive indices depending on crystal orientation. The material is transparent in the range from $400\,nm - 4500\,nm$[168]. The orthorombic room temperature phase has an mm2 point group. The mm2 point group is non-centrosymmetric, thus allowing non-linear processes. Its second-order susceptibility tensor shows five non-vanishing elements, of which three are independent under Kleinman symmetry (Fig. 8.2). The coefficients at $1064\,nm$ are $d_{31} = 15\,pm/V$, $d_{32} = 18\,pm/V$, $d_{33} = 27\,pm/V$, $d_{15} = 16\,pm/V$ and $d_{24} = 17\,pm/V$[170].

Furthermore, potassium niobate is ferroelectric along the crystallographic c axis. It forms ferroelectric domains inside the material, which are enhanced by Fe doping[171]. Accordingly, $KNbO_3$ shows the photorefractive effect, i.e., coherent patterns can be stored inside the material through domain polarization. Hence, iron doped potassium niobate is a suitable holographic storage material and is often used in such application.

The sample investigated in this thesis is a commercially available orthorombic Fe:$KNbO_3$ ($5\,ppm$) crystal[1]. The crystals were polished for a smooth surface and less scattering in the optical experiments.

8.2 Quartz

Silicon dioxide occurs in many forms: as sand, glass or single crystalline form. Several polymorphs exist of its crystalline form: α- and β-quartz, β-tridymite, coesite, and many more. Its phase changes with temperature and pressure applied to the structure, too. α-quartz is the common polymorph of single crystalline SiO_2 under room temperature and

1 from the Forschungsinsitut für mineralische und metallische Werkstoffe Edelsteine/Edelmetalle GmbH (FEE)

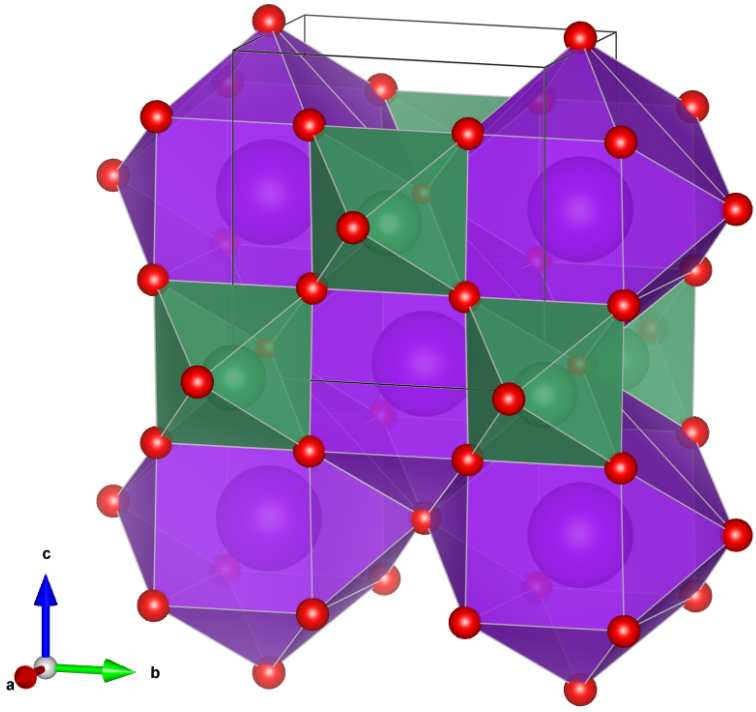

Figure 8.1: Crystal structure of $KNbO_3$ in the orthorhombic phase. The atoms are color coded: green for Nb, violet for K, red for O.

normal pressure conditions. It crystallizes in a tetragonal structure with point group 32 (Fig. 8.3) and is a positive uniaxial crystal, thus shows birefringence and has two optical axes. The second order non-linear susceptibility tensor has five non-vanishing elements, of which two are independent. Its most important coefficient is $d_{11} = 0.30\,\mathrm{pm/V}$ at 1064 nm[168], which is a common correction value for relative SHG measurements. Here, an α-quartz reference is used as a calibration standard for the absolute non-linear coefficient of $KNbO_3$, too. A 3 mm thick z-cut α-quartz plate is used throughout the experiments.

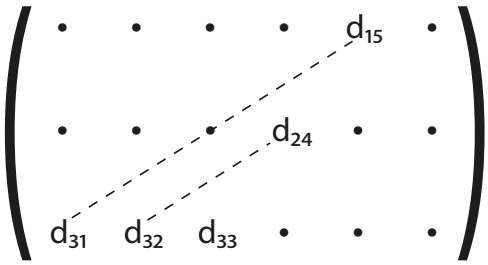

Figure 8.2: Second-order susceptibility tensor of the mm2 crystal class.

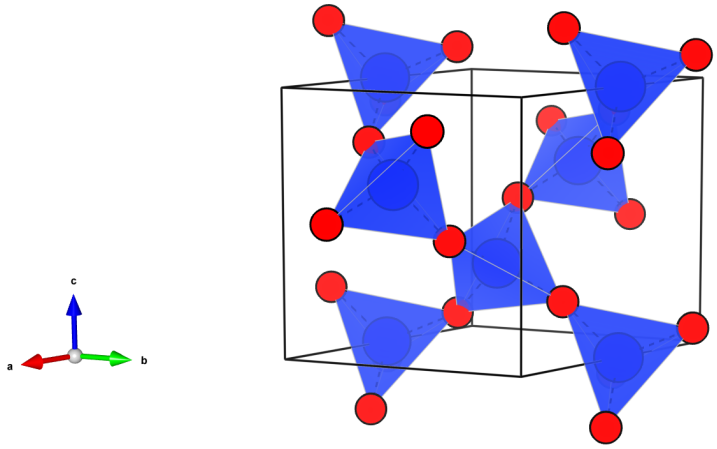

Figure 8.3: Crystaline structure of α-quartz. The atoms are color coded: Si in blue, O in red.

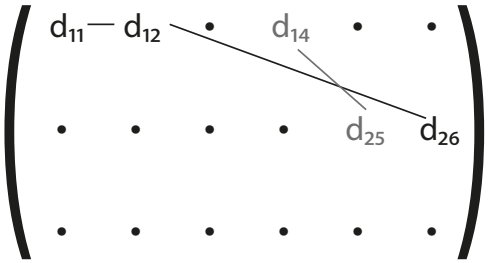

Figure 8.4: Second-order susceptibility tensor of the 32 crystal class.

8.3 Organotin Sulfide Clusters

A recently synthesized molecule shows white-light emission under irradiation with an infra-red cw laser diode. Several slightly different molecular structures exhibiting such white-light emission exist to today. They mutually consist of a tin-sulfur cluster core in an adamantane-like arrangement ($Sn_4S_6^{4+}$) with four attached ligands, typically having an aromatic ring structure. $[(PhSn)_4S_6]$ is the simplest structure fulfilling these structural prerequisites, showing white-light emission. Hence, it acts as a prototypical compound and reference for functionalized derivatives of the molecular family. On a macroscopic scale the molecules exhibit an amorphous state due to their complex form and high rotational degree of freedom of the ligands.

First investigations on this structural family were carried out by Rosemann et al.[23]. Here, a variation of the molecule ($[((4\text{-}(CH_2{=}CH)\text{-}C_6H_4)Sn)_4S_6]$) shows white-light emission with a high non-linear dependence, i.e., the input-output power relation scales with a power of eight. Moreover, the emitted white-light retains the directionality of the driving laser, hence the process is similar to supercontinuum generation. Remarkably, the process is efficient for cw laser excitation, in contrast to common supercontinuum processes, which require short pulse excitation and a high frequency bandwidth. As a consequence, the internal process of supercontinuum generation is different as in common devices, such as PCFs. The underlying microscopic process is still unclear. In

a simple picture the process may be understood in terms of the bond-charge model: the high electron polarizability, orbital asymmetry and highly delocalized wave functions of the steric ligands give rise to non-linear emission. Further, the ligands have a high degree of vibrational freedom, i.e., they can tilt and rotate with respect to the cluster core. This vibrational motion may create a complex dynamic potential, broadening the incident light through vibrational scattering. Another factor is the amorphous habitus of the molecule, i.e., the orientation of the molecules with respect to each other is randomly. Hence, further broadening and scattering occurs due to the overlapping of randomly oriented vibrational potentials along the optical path. In combination, these effects have the potential to create the strong supercontinuum emission observed in the experiments.

Another report[25] investigates the influence of the aromatic ligand and replacement of the cluster-core tin with Ge or Si. The ligand is varied from 1-napthyl, styril, phenyl to methyl, thus decreasing the size of the ligand. Accordingly, the presence and nature of the aromatic ring system is changed. In methyl, the aromatic ring is not present at all and decreased in size throughout the other three ligands. The form of the aromatic ring system alters the inter-molecular arrangement, changing the ordering from amorphous to crystalline. Two conclusions are drawn from the behavior of the different molecules: the π-system is essential for white-light generation, as methyl shows only SHG emission. Additionally, the double aromatic ring system of napthyl create a macroscopic order between the molecules, thus suppressing white-light emission. As a consequence, inter-molecular disorder is an important prerequisite in this novel process in white-light generation. Further, the variation of the clusters group IV elements shows a similar picture, as they change the molecular ordering. The $[(PhSi)_4S_6]$ molecule crystallizes and, accordingly, shows SHG. The cluster molecules with core containing tin and germanium exhibit an amorphous ordering and generate white-light.

As a consequence, the direct behavior of crystalline versus amorphous states is studied[172]. The similar molecule $[AdPh_4]$ with an adamantane cluster core is synthesized in amorphous and crystalline form. Again, it was found that the crystal structure suppresses the white-light generation process and shows SHG. Here, the input-output power efficiency scales with the sixth power of the incident power.

In this work, an additional sample series is investigated. Three different organo-coinage metal molecules replace one of the phenyl ligands: Au ($[(Me_3P)_3Au]$), Cu ($[(Me_3P)_3Cu]$) and Ag ($[Et_3P_3Ag]$).

9 | Methods

9.1 Absolute Second Harmonic Generation

This section describes the measurement of the second-order non-linear coefficient in potassium niobate. The second-order susceptibility is a widely used tool in reaching before unreachable regions in the light spectrum. There are several mechanisms depending on the existence and strength of the second-order nonlinear coefficient: SHG, sum frequency generation (SFG) and parametric amplification. For Centrosymmetric materials suppress these effects, since their even non-linear coefficients vanish in the Taylor expansion of the susceptibility (see Sec. 2.2 and Boyd[69] for further insights)

The experimental setup consists of two identical beam paths where the investigated sample is placed in one branch and a z-cut quartz reference sample is placed in the other branch. The quartz plate is used to correct for laser fluctuations and to scale it to an absolute scale with the literature-known coefficient for quartz. It is aligned, such that the linear polarization of the laser light is parallel to the x axis, such that $d_{eff} = d_{11}$. Additionally, different correction terms have to be considered to account for different reflectivity, sample geometries and phase matching quality.

Setup

To accurately determine the absolute SHG coefficients of a material a calibration standard is needed to account for experimental fluctuations. The main causes for errors are either systematic errors due to detector response curves, aberrations of optics and geometrical efficiencies or fluctuations due to changing beam properties, emerging from different spectral and temporal pulse widths and changing overall laser power. To account for all of these experimental uncertainties, the experiment has two branches (Fig. 9.1): a sample branch and a branch with a z-cut quartz reference. Quartz is an excellent reference material due to its well-known d_{11} coefficient[168].

A pulsed laser is required to generate strong SHG responses. In the experiment (Fig. 9.1) a 80 fs to 10 fs titanium-sapphire oscillator with a repetition rate of 78 MHz is used. The oscillator is equipped with a spectrally broad mirror set to achieve a tuning range from 1.15 eV to 1.72 eV. Accordingly, the pulse energies lie between 10 nJ to 35 nJ. In the next stage, an active stability control (Fig. 9.1) corrects for geometrical fluctuations of the laser beam and ensures that the laser does not drift in the optics and that the same spot on the sample is hit for each measurement. It consists of a beamsplitter and two silicon CCDs, which are divided into four sectors to determine the beam position. The detectors have a path difference to correct either for position and angle of the beam. Two piezo actor mirrors correct the beam path and build a feedback loop together with the detectors. Additionally, the power of the beam is controlled by a polarizing beam splitter and a rotatable $\lambda/2$ plate to keep the excitation power stable throughout the experiment. The beam emerging from the laser oscillator is divided by a 50:50 beam splitter into two equal branches to perform simultaneous measurements on the sample

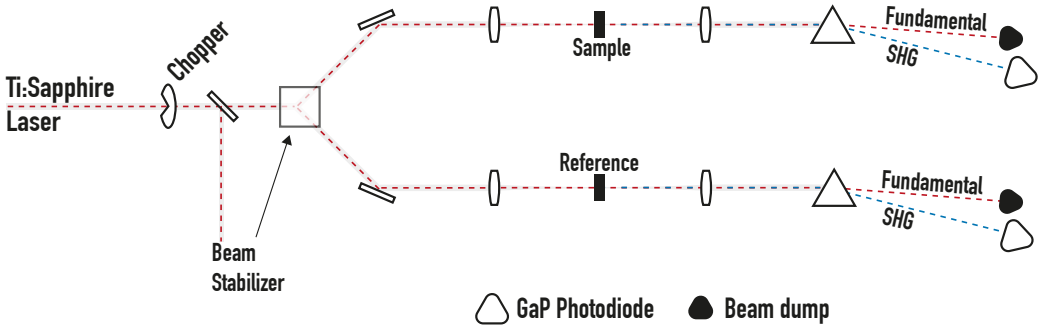

Figure 9.1: Experimental seutp for the measurement of the absolute second-order nonlinearity. The light is split in two equal branches to do an accurate measurement with a calibrated reference. In both branches a prism with a GaP diode is used to disperse and detect the SHG SIGNAL.

and reference system (Fig. 9.1). Each of the branches contain two lenses of amorphous SiO_2 with a focus length of 100 mm. They focus and collimate the light into and coming from the sample. The collimated beam is dispersed by a rotatable prism to select the SHG wavelength. The fundamental beam is dumped and the SHG beam is collected by a gallium phosphide photodiode. To suppress any residual fundamental beam on the photodiode a colored glass filter with a pass band from 2.13 eV to 3.44 eV (Schott BG39) is used. A lock-in amplifier measures the signal in current mode (Stanford SR830), for which a chopper is installed in front of the beam splitter. The chopper is set to a chopping frequency of 666 Hz for low pink $(1/f)$ noise.

Correction

The correction of the absolute values is done in two domains: first, the values have to be scaled relative to the quartz reference and for different efficiencies and transmission factors of the samples. Second, the relative factor is scaled with the d_{11} coefficient of quartz, where its frequency dependence has to be taken into account.

Different efficiencies and transmission factors at the interfaces of the samples have to be considered. They can be treated in the wave picture. Generally, the Maxwell equations (Eq. 2.1 to Eq. 2.4) describe all the phenomena for SHG generation and propagation inside a crystal and its interfaces. From this, the wave equation for electricl fields in vacuum can be easily deduced:

$$\nabla \times \nabla \times \mathbf{E} + \mu_0 \frac{\partial^2}{\partial t^2} \mathbf{D} = 0. \tag{9.1}$$

By inserting **D** and the general relation of a double curled vector field[1] into this equation, we obtain

$$\nabla^2 \mathbf{E} - \frac{1}{\epsilon_0 c^2} \frac{\partial^2}{\partial t^2} \mathbf{D} = \frac{1}{\epsilon_0 c^2} \frac{\partial^2 \mathbf{P}}{\partial t^2}. \tag{9.2}$$

This equation is valid as long as $\nabla(\nabla \cdot \mathbf{E}) = 0$. Fortunately, the relation is fulfilled for transverse, infinite plane waves and negligible small in virtually any other case in

1 $\nabla \times \nabla \times \mathbf{E} = \nabla(\nabla \cdot \mathbf{E}) - \nabla^2 \mathbf{E}$

nonlinear optics. It is convenient to split the polarization in its linear and nonlinear part: $\mathbf{P} = \mathbf{P} + \mathbf{P}_{\text{NLS}}$. Under the general relation $\mathbf{D} = \epsilon_0 \epsilon_r^{(1)} \mathbf{E}$ we obtain

$$\nabla^2 \mathbf{E}_{2\omega} - \frac{\epsilon_r^{(1)}}{c^2} \frac{\partial^2}{\partial t^2} \mathbf{E}_{2\omega} = \frac{1}{\epsilon_0 c^2} \frac{\partial^2 \mathbf{P}_{\text{NLS}}}{\partial t^2}. \tag{9.3}$$

This is the wave equation for the propagation of the SHG in a material and $\mathbf{P}_{\text{NLS}}$ is a nonlinear source term, which describes the driving of the second-harmonic wave by the fundamental. $\mathbf{E}_{2\omega}$ is the electric field of the second harmonic wave. The nonlinear source term is represented by the term

$$\mathbf{P}_{\text{NLS}} = \mathbf{e}_p \cdot P_{\text{NLS}} = 2\epsilon_0 d \cdot \mathbf{E}_\omega^2. \tag{9.4}$$

Here, $\mathbf{e}_p$ is the unit vector of the induced polarization, d is the reduced effective nonlinear coefficient (Sec. 2.2) and $\mathbf{E}_\omega$ is the fundamental wave. For a vanishing nonlinear source term Eq. 9.3 can be easily solved by using plane waves and we obtain for the free electric and magnetic field, respectively:

$$\mathbf{E}_{2\omega,\text{hom.}} = \mathbf{e}_f A_f \exp\{[\mathrm{i}\,(\mathbf{k}_f \cdot \mathbf{r} - 2\omega t)]\} \tag{9.5}$$

$$\mathbf{H}_{2\omega,\text{hom.}} = \frac{1}{2\omega} (\mathbf{k}_f \times \mathbf{e}_f) A_f \exp\{[\mathrm{i}\,(\mathbf{k}_f \cdot \mathbf{r} - 2\omega t)]\}. \tag{9.6}$$

Here, $\mathbf{k}_f$ is the wavevector of the free second-harmonic wave and A_f is its amplitude. To account for the inhomogeneous part of the differential equation, we use a special solution ([173]):

$$\mathbf{E}_{2\omega,\text{inhom.}} = \frac{\omega^2 P_{\text{NLS}}}{\epsilon_0 c^2 (k_b^2 - k_f^2)} \left(\mathbf{e}_p - \frac{\mathbf{k}_b (\mathbf{k}_b \cdot \mathbf{e}_p)}{|k_f|^2} \right) \exp\{\mathrm{i}(\mathbf{k}_b \cdot \mathbf{r} - 2\omega t)\} \tag{9.7}$$

$$\mathbf{H}_{2\omega,\text{inhom.}} = \frac{\omega^2 P_{\text{NLS}}}{\epsilon_0 c^2 (k_b^2 - k_f^2)} (\mathbf{k}_b \times \mathbf{e}_p) \exp\{\mathrm{i}(\mathbf{k}_b \cdot \mathbf{r} - 2\omega t)\}. \tag{9.8}$$

Accordingly, $\mathbf{k}_b$ is the wavevector of the bound wave. The total electric field is then given by $\mathbf{E}_{2\omega} = E_{2\omega,\text{hom.}} \mathbf{e}_f + E_{2\omega,\text{inhom.}} \mathbf{e}_b$, where $\mathbf{e}_b = \mathbf{e}_p - \mathbf{k}_b (\mathbf{k}_b \cdot \mathbf{e}_p)/|k_f|^2$.

Boundary conditions

The SHG emission at interfaces and surfaces have to be considered and taken into account since they break the inversion symmetry. The transmission and generation factors are deduced by the boundary conditions at the $z = 0$ and $z = L$ interface, where L is the thickness of the sample. The coordinate system is chosen, such that the $z = 0$ plane represents the sample facet and the plane of incidence is the $y = 0$ plane (Fig. 9.2). The tangential component of the electric field is continuous across interfaces. Therefore, a reflected SHG wave has to exist. Accordingly, the x components of the k vectors have to be equal at the interface.

Harmonic waves are chosen as solution, such that the electric field vector is normal to the plane of incidence, $\mathbf{e}_f = \mathbf{e}_R = \mathbf{e}_y$. The continuity of the tangential components demands at the boundary $z = 0$ that for the y component of the field

$$k_R E_{2\omega}^R = E_{2\omega} + \frac{\omega^2 P_{\text{NLS}}}{\epsilon_0 c^2 (k_b - k_f^2)}. \tag{9.9}$$

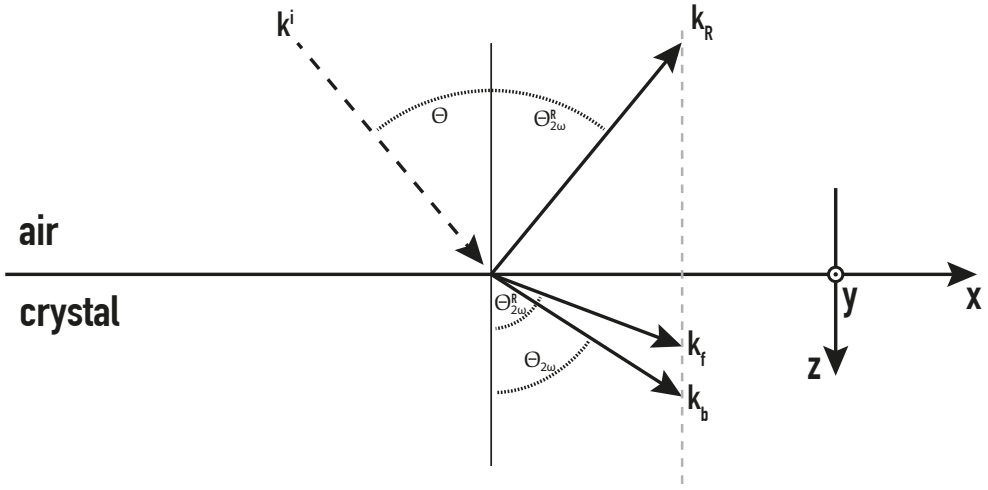

Figure 9.2: Geometry of the reflected and transmitted fundamental and SHG beam at the interface of air and the nonlinear material. After Boyd[69]

The magnetic field is retained in the x component, which yields

$$-k_R E^R_{2\omega} \cos\theta^R_{2\omega} = k_f E_{2\omega} \cos\theta_{2\omega} + k_b \cos\theta_\omega \frac{\omega^2 P_{\text{NLS}}}{\epsilon_0 c^2 (k_b^2 - k_f^2)}. \tag{9.10}$$

By inserting Eq. 9.9 into Eq. 9.10 the amplitude of the nonlinear field is obtained:

$$E_{2\omega} = -\frac{k_R \cos\theta^R_{2\omega} + k_b \cos\theta_\omega}{k_f \cos\theta_{2\omega} + k_R \cos\theta^R_{2\omega}} \cdot \frac{\omega^2 P_{\text{NLS}}}{\epsilon_0 c^2 (k_b^2 - k_f^2)}. \tag{9.11}$$

The absolute values of the k vectors can be expressed as $k_i = n_i \cdot 2\omega/c$ and the equation simplifies to

$$E_{2\omega} = \frac{\cos\theta^R_{2\omega} + n_\omega \cos\theta_\omega}{n_{2\omega} \cos\theta_{2\omega} + \cos\theta^R_{2\omega}} \cdot \frac{P_{\text{NLS}}}{\epsilon_0 (n_{2\omega}^2 - n_\omega^2)}. \tag{9.12}$$

This equation is now used to construct the continuity relation at the output facet in the same manner. Again, for each of the fields a constraint is used and both equations are used to eliminate the reflected field, which yields

$$E^{\text{out}}_{2\omega} = E' \exp\left(\mathrm{i}(\mathbf{k}_b - 2\mathbf{k}_\omega) \cdot \mathbf{e}_z L\right) + E'' \exp\left(\mathrm{i}(\mathbf{k}_f - 2\mathbf{k}_\omega) \cdot \mathbf{e}_z L\right) \tag{9.13}$$

$$E' = \frac{n_\omega \cos\theta_\omega + n_{2\omega} \cos\theta_{2\omega}}{\cos\theta + n_{2\omega} \cos\theta_{2\omega}} \cdot \frac{P_{\text{NLS}}}{\epsilon_0 (n_{2\omega}^2 - n_\omega^2)} \tag{9.14}$$

$$E'' = \frac{2 n_{2\omega} \cos\theta_{2\omega}}{\cos\theta + n_{2\omega} \cos\theta_{2\omega}} E_{2\omega}. \tag{9.15}$$

This easily yields the output intensity by the straight-forward relation $I_{2\omega} = \sqrt{\epsilon_0/\mu_0} \cdot |E^{\text{out}}_{2\omega}|^2$ yielding the emitted and measurable SHG intensity from the sample:

$$|E^{out}_{2\omega}|^2 = (E' + E'')^2 + 4E'E'' \sin^2\left[\mathrm{i}(\mathbf{k}_b - \mathbf{k}_f) \cdot \mathbf{e}_z L/2\right] \tag{9.16}$$

The first term is not dependent on the sample thickness and generally much smaller than the second term (four orders of magnitude for quartz and $KNbO_3$[173]) and is therefore

omitted in the following. By redoing all substitutions and for the case of normal incidence the refractive index depended correction factor is obtained:

$$I_{2\omega} = \frac{8cP_{\mathrm{NLS}}^2}{\epsilon_0} \cdot \frac{n_{2\omega}(n_\omega + n_{2\omega})(1 + n_\omega)}{(1 + n_{2\omega})^3} \cdot \frac{\sin^2\left[\pi L/(2l_c)\right]}{(n_{2\omega}^2 - n_\omega^2)^2} \tag{9.17}$$

Here, $l_c = \frac{\lambda}{4}|n_\omega - n_{2\omega}|$ is the coherence length for normal incidence (Sec. 2.2). The three factors of this equation represent a physical effect each (in the order of their appearance):

1. The generation efficiency & the dependency on the driving field.
2. The reflectance and transmittance factors for the SHG wave ($= \tau$).
3. The phase mismatch, both of the coherence length and of the wave vector ($= \Delta\phi$).

Substitution of these new labels, leads to the more simple equation

$$I_{2\omega} = \frac{8cP_{\mathrm{NLS}}^2}{\epsilon_0} \cdot \tau \cdot \Delta\phi. \tag{9.18}$$

It is important to consider two things about this equation: first, it does not account for multiple reflection, which in turn can create additional SHG power. Generally, this is neglected for low refractive indices, but unfortunately potassium niobate shows a rather high refractive index[84]. In our case, it is still not taken into account, since the electromagnetic field is focused inside the sample. Therefore, the laser beam diverges for the backward reflection leading to decreasing power density and vanishing SHG power. The error due to multiple reflection in potassium niobate is roughly 4 % and the attenuation of the electric field due to a focused Gaussian beam on the length scale of the crystal is approximately one order of magnitude. This leads to a total error of less than a half percent not taking into account aperture effects at the collecting lens.

The second thing to pay attention to is the attenuation of the incident fundamental beam at the input facet giving rise to the nonlinear polarization P_{NLS}. Accordingly, the scalar nonlinear polarization needs to be scaled down by the Fresnel transmission coefficient t_ω of the fundamental beam.

9.2 Steady-State White-Light

Steady-state white-light spectroscopy is done with a confocal microscopy setup (Fig. 9.3). The excitation source was either a 100 fs Ti:sapphire laser oscillator with a repetition rate of 78 MHz or a cw laser diode with an wavelength of 1450 nm. The emission wavelength of the Ti:sapphire laser oscillator can be tuned, but was set to 800 nm throughout the experiments present in this thesis. Further, the light from the oscillator can be frequency doubled or tripled to extend the intrinsic operation range. This allows for the generation of 266 nm laser light, used in the PL experiments.

The confocal setup employs a 0.5 NA Schwarzschild objective, which focuses the beam onto the sample under vacuum conditions and room temperature. The objective collects the back reflected or emitted light and focuses it into an imaging camera and the entrance slit of a quarter meter Czechy-Turner monochromator (Oriel Instruments MS260i Imaging 1/4m Spectrograph). This spectrograph is equipped with a grating blazed at an angle of 410 nm and 122 gratings / nm. A silicon deep-depletion CCD

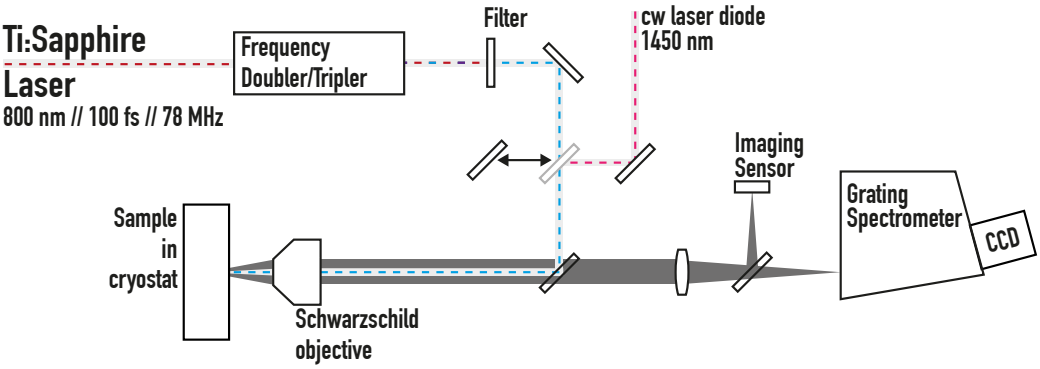

Figure 9.3: Schematic of the confocal PL and white-light detection setup. The light of the incident laser can be frequency doubled or tripled. A Schwarzschild objective focuses the light onto the sample and collects the emission of the sample. The emission is detected by a grating spectrometer and a CCD.

array-detector (Andor DU 440 BU) is mounted to the output port of the spectrograph and detects the dispersed light. The camera is thermoelectrically cooled to −60 °C to minimize thermal noise and dark current.

10 | Results

10.1 Absolute Second-Order Nonlinear Coefficient of $KNbO_3$

This section presents the measurements of the second-order nonlinear of $KNbO_3$ relative to a z-cut quartz reference. The experimental setup (Fig. 9.1) as outlined in Sec. 9.1 is used throughout the measurements. For some of the measurements, a stability control is used (Fig. 9.1) and for all the other measurements the SHG signal is maximized.

Equation 9.18 corrects the intensity measurements for sample and reference taking into account the known nonlinear coefficient of the reference and scales the $KNbO_3$ measurements to the correct values. Accordingly, the relative intensity is rearranged, such that the d coefficient of $KNbO_3$ is obtained:

$$d = \sqrt{\frac{(\tau \cdot t_\omega^4 \cdot \Delta\phi)_{\text{Quartz}}}{(\tau \cdot t_\omega^4 \cdot \Delta\phi)_{KNbO_3}}} \cdot \sqrt{\frac{I_{2\omega}^{KNbO_3}}{I_{2\omega}^{\text{Quartz}}}} \cdot d_{\text{Quartz}} \tag{10.1}$$

Each effect of the different contributions will be considered individually and then the complete experimental data will be presented. First, the contribution of the oscillating function of the phase mismatch $\Delta\phi$ is considered. The refractive indices of potassium niobate and quartz enter the calculation. Here, the works of Ghosh[174] and Uematsu[170] are used for quartz and for $KNbO_3$, respectively (similar results in Zysset et al.[175]).

Due to the very small coherence length of a few microns in potassium niobate and tens of microns for quartz the oscillations are very narrow in the wavelength regime for normal incidence. Thus, the oscillation does not affect the actual output intensity due to the spectral bandwidth of the fundamental laser beam. Averaging the oscillation with a Gaussian function ($\sigma = 10\,nm$) leads to a constant correction factor arising solely from the wave vector mismatch. Thus, the oscillatory behaviour of the SHG will be dropped completely in the following discussion.

The evaluation of the other correction factors is straightforward, as they depend only on the refractive indices of quartz and $KNbO_3$. Therefore, the other parameters are all calculated at once. At this stage we are now able to calculate the total SHG power relative to d_{11} of quartz. To deduce absolute values from this point the data is simply multiplied by the quartz coefficient. Unfortunately, this factor is only known for few discrete wavelengths ([168]). Miller's delta rule is used to expand these selected wavelengths across the whole measurement range Miller's delta rule is used[66] (Sec. 2.2):

$$d_{11} = \delta_{11} \cdot \epsilon_0 \left(n_{2\omega}^2 - 1\right)\left(n_\omega^2 - 1\right)^2. \tag{10.2}$$

The parameter δ_{11} is the miller delta, which is deduced empirically. Here, we use the refractive indices and d_{11} at 1064 nm ([168]) for quartz, which yields $\delta_{11} = 1.328 \cdot 10^{-2}\, m/C$.

A b-cut $KNbO_3$ crystal is measured and corrected with the above considerations. The a axis is aligned such, that it is parallel to the polarization of the incident laser beam. Accordingly, the non-linear coefficient for this measurement geometry is the

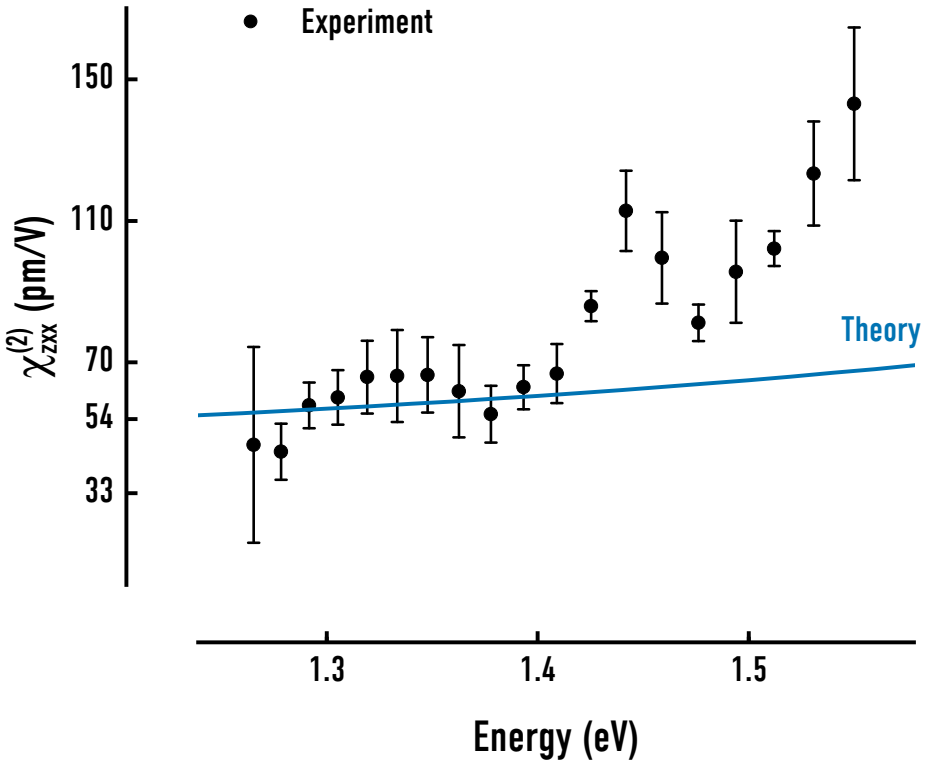

Figure 10.1: Measurement data of the $\chi^{(2)}_{zxx}$ coefficient of b-cut $KNbO_3$ (black dots) in comparison with DFT calculations (blue line).

$\chi^{(2)}_{zxx}$ coefficient, since the polarization along x is suppressed in this direction due to the polarity of the crystal lying along the z axis. Therefore, the SHG is type II in the given geometry.

The experimental data (black dots in Fig. 10.1) are compared to results from DFT calculations (Fig. 10.1 blue line) from the group of Sanna et al.[176]. Excellent agreement for the energies below 1.4 eV is achieved. However, a large discrepancy between measurement and theory is found for energies above 1.4 eV. The nonlinear coefficient is expected to be resonance-free in the measurement range, however, a strong increase of up to a factor of two in the nonlinear coefficient is found in the experiment. We attribute this to different mechanisms which could be present here. First, the material has a low doping of Fe, which of course would affect the properties of the material system. For instance, it is known that high Fe doping concentrations shift the absorption edge to lower energies[177]. Generally, potassium niobate is known to show domains during growth, which makes it hard to grow as single crystal. It is the reason why this material is not used in broad industry scale production for instance as frequency doubler or tripler material. It is likely to assume that the doping introduces even more domains inside the crystal which of course affect the generation of SHG, since every breaking of inversion symmetry introduces another SHG signal. Therefore, Fe doping can act as local SHG generation centers inside the material. There are different processes which arise from this local defect centers. First, generation of additional SHG increases the total intensity compared to a single crystal material. Second, the SHG can stronger convert back into the fundamental compared to undisturbed electric field inside the crystal. The latter

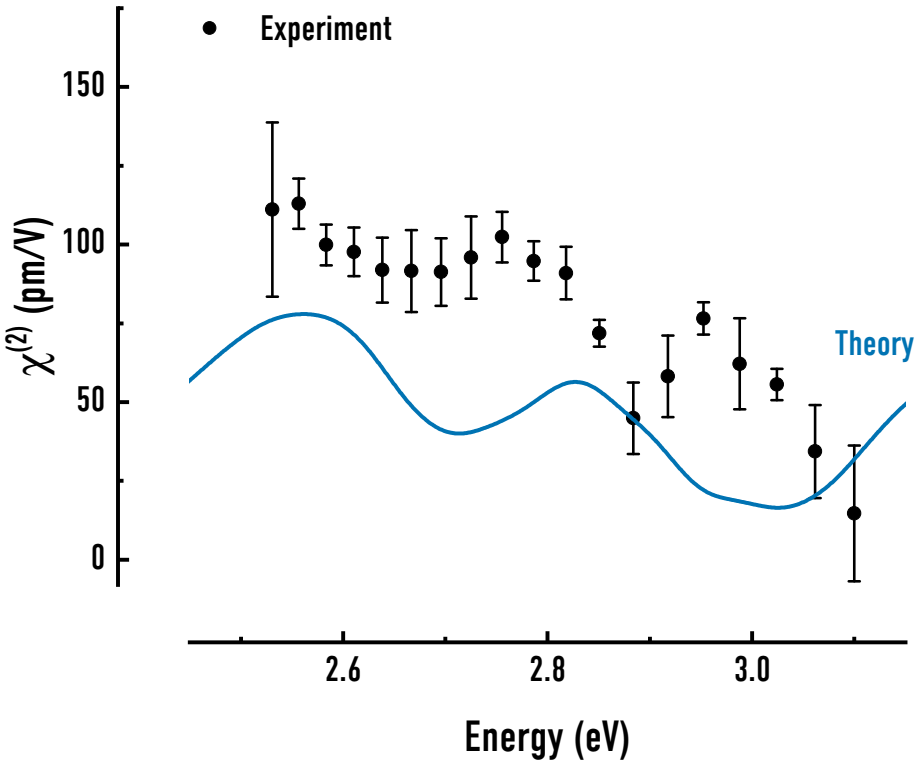

Figure 10.2: $\chi^{(2)}_{zxx}$ measurement data (black dots) shown at twice the energy to compare with the theoretical resonances at this regime. The measurement data is flipped around its mean.

effect is generally valid also for single crystals: the SHG can in turn generate SHG for itself giving rise to a cascaded second harmonic effect. This could be greatly enhanced by Fe doping centers, giving rise to light at the quarter of the fundamental beam. The light is affected by the resonances at twice the fundamental wavelength of the incident beam. Nevertheless, light is not only found at the cascaded SHG but also converted back into the SHG light, giving rise to resonances only available in twice the energy range of the actual SHG.

Therefore, the measurement curve is compared to the theoretical data at the fourth of the fundamental energy (Fig. 10.2). For better comparison the measurement values are plotted flipped around their mean value. Except for the relatively strong resonance at 2.85 eV the curve is reproduced quite well. The data is slightly blue-shifted by around 500 meV compared for the theoretical findings. This could be due to temperature difference between measurement and theory, as the experiments have been carried out at room temperature, while the simulations assume 0 K.

To further substantiate these findings, the emission from potassium niobate is dispersed in a spectrometer and detected by a silicon charge-coupled array detector. The incident photon energy is varied, as in the other SHG experiments, and the emission ranging from 4.72 eV to 6.61 eV is monitored (Fig. 10.3). Unexpectedly, light at a quarter of the incident wavelength can be seen. Intriguingly, this emission is split into a doublet, two smaller peaks centered around the actual fourth harmonic. Furthermore, the fourth harmonic shifts to a constant and stronger resonance for 1.23 eV and lower fundamental

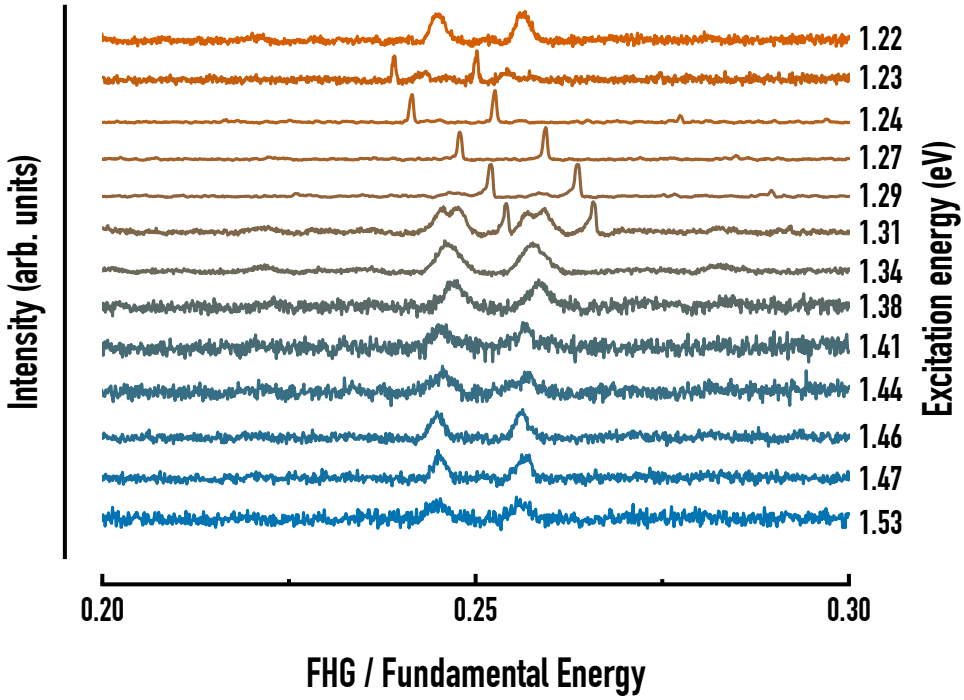

Figure 10.3: Fourth harmonic spectrum of $KNbO_3$ for different incident energies. The energy is normalized to the incident photon energy.

photon energies. This tentatively Fe-related resonance is constant over the entire range from 1.23 eV to 1.31 eV. It is created by phase-matching of the cascaded SHG, which happens to take place around 1.26 eV. The slight shift of emission is attributed to the increased efficiency around the phase matching wavelength (Fig. 10.5): when the spectral distribution of the fundamental driving field overlaps with the phase matching region, the efficiency easily surpasses the generation at exact the fourth of the fundamental energy by many orders of magnitude. Moreover, only the generation at the phase-matching energy is seen and its intensity changes as long as the driving laser overlaps this region.

The mode-splitting resembles phenomena observed for Mie scattering in nano--structures[178] or cascaded photonic structures[179]. This effect is attributed to Mie or Rayleigh scattering at local defect centers arising from Fe doping since the strong interplay between multiple SHG processes is assumed to arise from Fe doping centers or domains inside the crystal. However, if the process is mainly governed by Rayleigh scattering it becomes obvious that it is strongly enhanced for the very blue wavelengths in cascaded SHG, due to the λ^{-4} dependency of Rayleigh scattering.

Phase-matching energies for cascaded SHG cannot be deduced from literature values alone as the Sellmeier fitting formula is only valid in the visible to near-infrared, as it only describes the dielectric function in the non-resonant part of the spectrum[180]. However, the frequency doubling is already affect by resonances in the dielectric function for energies above 2 eV. To accurately model these resonances, the full DFT calculation is used (Fig. 10.4). The calculations describe a wide bandwidth of potassium niobate, allowing for further investigation for very blue wavelengths. Obviously, each optical axis shows possible phase matching for energies around 2 eV to 3 eV, due to a resonance

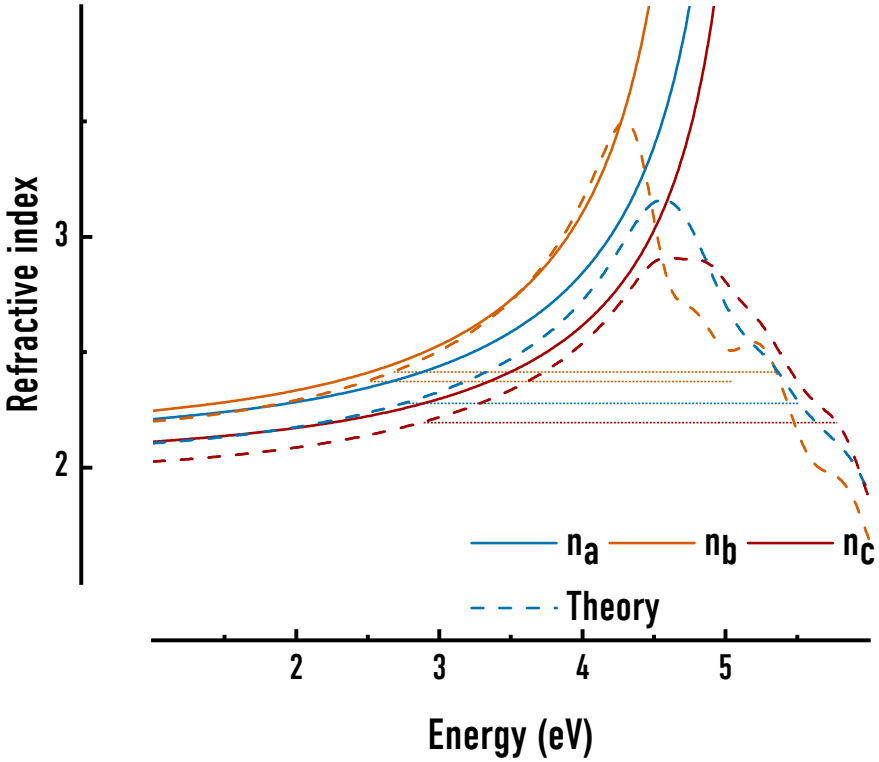

Figure 10.4: Refractive indices for $KNbO_3$ in the Sellmeier approximation (solid lines) and from DFT calculations (dashed lines). Dotted lines indicate the phase matching positions for the theoretical curve.

around 4 eV (dashed lines in Fig. 10.4). Consequently, the phase matching efficiency is easily deduced by calculating $|n_{2\omega} - n_{\omega}|^{-1}$. The calculation leads to a three different phase matching energies: 2.68 eV (b axis), 2.76 eV (a axis) and 2.89 eV (c axis).

Comparison with the measured data for the zzz and zyy directions yields quite good agreement (Fig. 10.5). The results from the calculation are plotted at half their photon energy to compare them to the measured SHG data. This clearly reveals that phase matching of cascaded SHG has a huge effect on the emitted SHG output power. However, it is not quite clear why the strong phase matching at ~1.3 eV is not observed in the measurement, whereas the slight side peak is pronounced in the experiment. This deviation could either be due to discrepancy of the density functional theory calculations to the actual values. The actual position is quite critical, since it depends on various parameters, e.g., the width and position of the resonance. The comparision with literature values clearly shows that the DFT calculation does not reproduce the resonance widths exactly. Further, the influence of the Fe doping is not contained in the current calculations. Generally, Fe doping red-shifts the absorption and resonances. Accordingly, it is possible that the actual resonance is measured, due to the red-shift in the zzz direction.

Nevertheless, it is clear that the theoretical and literature values of the absolute second-order nonlinear coefficient can be determined well. Moreover, the measurements provide evidence for higher mixing processes, yet significant open questions remain:

- Why is the interaction of SHG and cascaded SHG so strong?

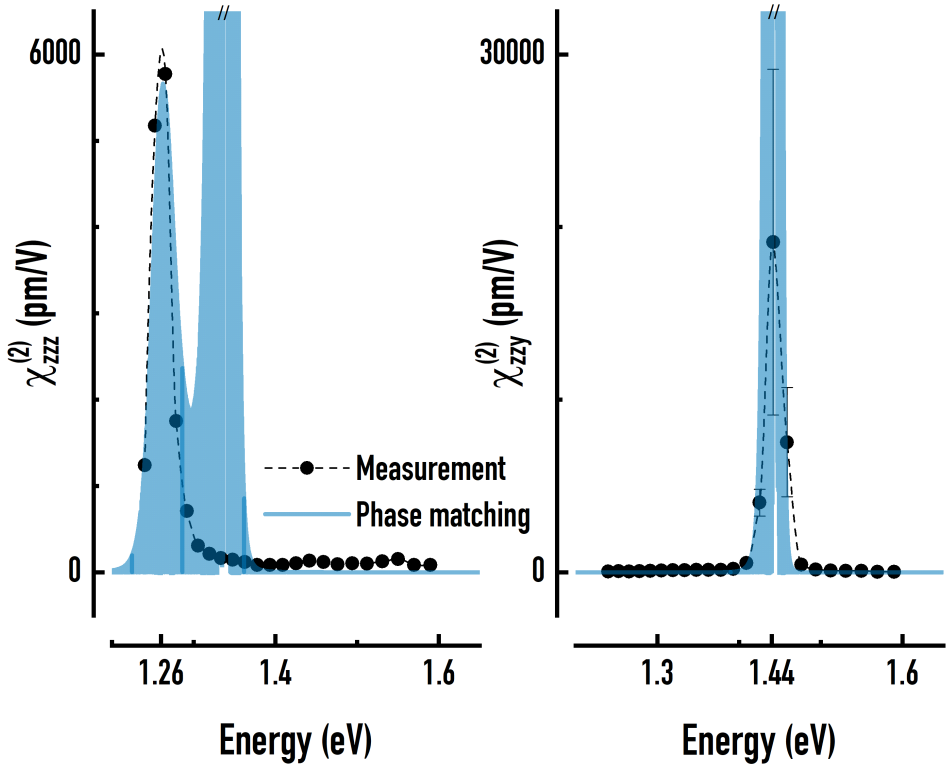

Figure 10.5: SHG intensity of the $\chi^{(2)}_{zzz}$ and $\chi^{(2)}_{zzy}$ coefficients of $KNbO_3$. The phase matching intensity for the respective axis are shown in blue.

- What is the actual influence of Fe doping on the nonlinear process?
- Are there domain walls inside the crystal and how do they affect SHG and cascaded SHG generation and back-conversion?

These open questions can not be answered by means of measurement carried out within the restraints of this work, alone. Rather, they are further paths in the research on potassium niobate and similar nonlinear materials. There are multiple techniques able to tackle those questions, e.g., SHG microscopy for further insight into internal domains and interfaces of the material, the study of a Fe doped series can shed light onto the actual influence of doping concentration. Further, an increase of photon energy bandwidth can give further insight in the resonant region. Here, other nonlinear materials can be used to double or triple the Ti:sapphire frequency up to 5 eV.

10.2 White-light Generation in Organotin Sulfide Clusters

The properties of white-light generation in $[(PhSn)_4S_6]$ clusters with one aromatic ligand replaced by a coinage metal complex are investigated. As the compounds crystallize the goal of the substitution is to determine whether the samples show non-linear properties solely from the molecular asymmetry. Therefore, the emission under pulsed and cw

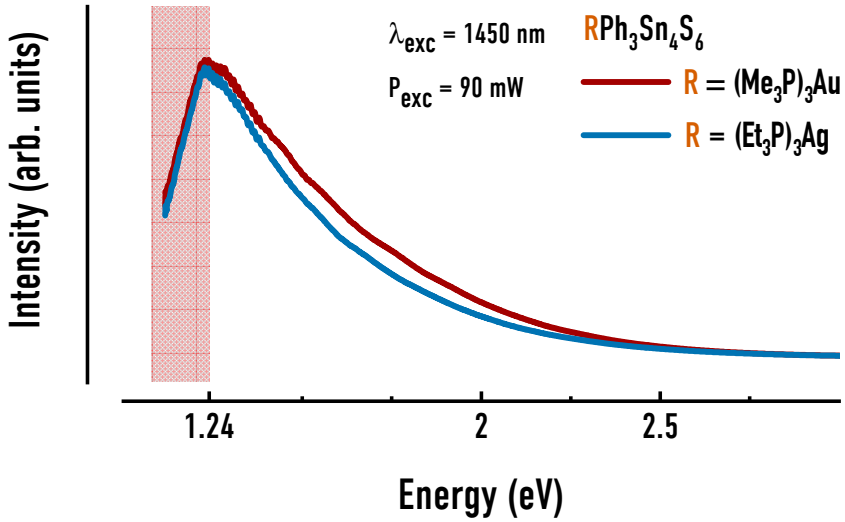

Figure 10.6: White-light emission from the Ag (blue) and Au (red) substituted compounds. The spectra where response corrected with a halogen lamp. The red area in the low-energy part marks the loss of intensity due to the vanishing of quantum efficiency in the detection system.

infra-red laser radiation is measured and it is found, that two of the samples show strong white-light emission. The complex in which one of the ligands was replaced by a copper complex doesn't show any emission, neither white-light nor SHG. Figure 10.6 depicts the spectra for both of the compounds showing white-light emission under irradiation with 1450 nm cw laser light. The red area in the graph shows the depletion of quantum efficiency of the detection system. Hence, the intensity in this regime is not reliable, since the response correction is not able to correct the system in this regime due to the general low intensity. However, as these findings point in the direction that the molecular asymmetry gives rise to the non-linear emission process, studies of the materials habit shows that the samples undergo amorphization under irradiation[181]. This stresses the importance of disorder of the compound as a necessity of white-light emission.

Additionally, PL measurements are performed on the compounds. To reach the high HOMO-LUMO gap of the samples pulsed blue light with a wavelength of 266 nm is used. The Au and Ag substituted compounds show a very similar PL with a peak at 2.84 eV (Fig. 10.7), corresponding to their HOMO-LUMO gap. Moreover, is the emission very similar to the emitted PL from the $[(PhSn)_4S_6]$ compound[23]. Hence, the replacement with Au and Ag molecule ligands does not change the general optical properties of the material, regarding linear and non-linear emission. In contrast the sample with the Cu replacement does show a rather strongly altered PL. The compound shows two peaks at 1.45 eV and 2.34 eV, which are strong red-shifted with respect to the other two compounds. This red-shift leads to a reabsorption if white-light is generation takes place, thus the emission is completely suppressed. Especially the lower energy resonance hinders the white-light process completely in this regime, with its typical on-set around 2 eV to 2.5 eV.

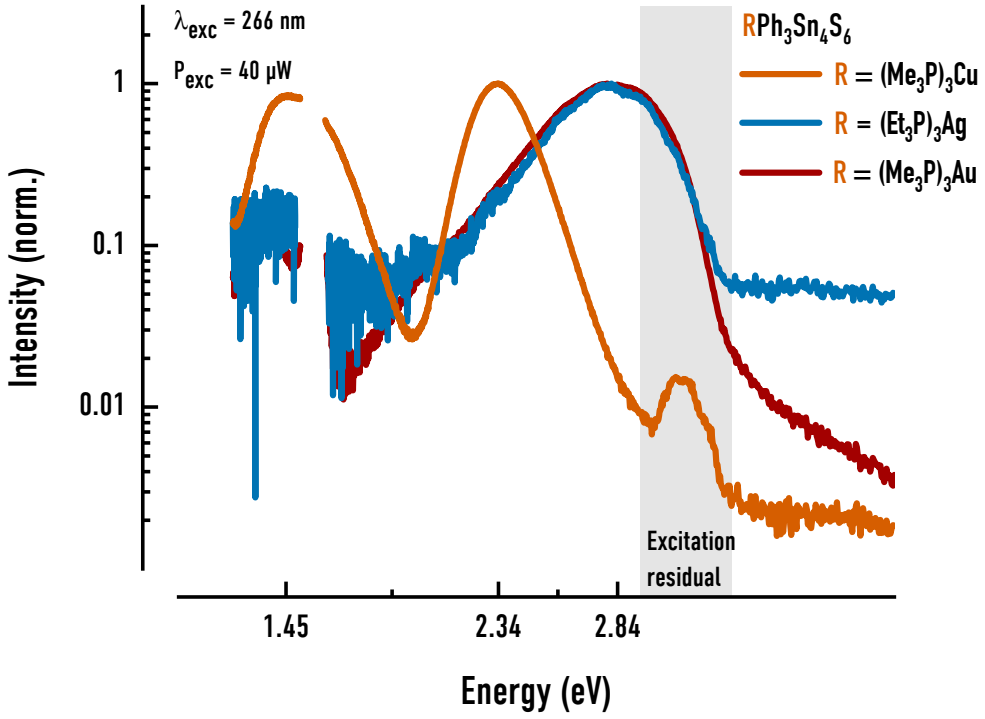

Figure 10.7: PL of all of the three compounds under irradiation with pulsed 266 nm light, a photon energy above the optical gap of all three materials. A part of the spectrum at 1.55 eV is not shown due to the residual laser fundamental in this regime. The small peak at 4.66 eV corresponds to the residual frequency doubled excitation light.

11 | Conclusion and Outlook

The functionalization of semiconductors is a powerful tool to enhance, e.g., accessible emission wavelengths. Ga(N,As,P) multilayer structures are excellent examples for the interplay between wavelength tuning by means of band gap engineering and lattice matching towards lasing structures monolithically integrated on silicon substrate, ready for CMOS implementation. Another approach for emitters at new wavelengths is the conversion of incident laser light by means of non-linear optical processes. Either, by SHG or by broadening of the incident laser in such a way, that white-light emission occurs. The white-light emission is a complex interplay of several non-linear processes. The spectroscopic experiments presented in this thesis are useful tools to characterize the optical and electronic properties of such structures. For example, the band offsets in a Ga(N,As,P) multilayer structure are determined. Additionally, the absolute SHG effect of potassium niobate and the white-light emission characteristics of novel SnS-cluster molecules have been measured.

In the following, I will give a summary and discussion of the core findings and outlooks to further investigations on the topics.

The first part investigated the Ga(N,As,P)/(B,Ga)(As,P)/GaP VB offsets. The combination of PLE measurements and the characteristics of the changing confinement energy yields a VB GaP-Ga(N,As,P) offset of 100 meV. However, the model to deduce the VB offset considers many assumptions due to multiple corrections applied to the measured transition energies. Therefore, XPS measurements are carried out to deduce the energy of the VB levels directly. With this technique, it is not only possible to measure the offset of the direct material, but of all the intermediate layers, too. The VB offset between Ga(N,As,P) and GaP is very small, on the order of $\pm$10 meV, probably rendering the structure of slight type-II character. These observations do not support the findings from the PLE measurements, which yield a significantly larger offset value. However, several experimental uncertainties have to be considered: first, the X-ray excitation source is not perfectly suited for the measurement at the VB edge. The X-ray bandwidth is rather broad and the X-ray absorption cross-sections of the materials are low. This results in low resolution and intensity around the VB edge, rendering the measurements rather inaccurate for small VB offsets of only several tens of meV. Furthermore, the depth information of the sample layers and interfaces is accessible only by Ar^+ sputtering yields. Here, preferential sputtering or contributions from a thin amorphous cover-layer distort the experiments. The optical measurements, on the other hand, suffer from different uncertainties: first, the extrapolation of material parameters by VCA is not robust against differing physical behavior or special cases, which the nitrogen incorporation demand due to its small covalent radius. Second, the PL is very defect-sensitive, especially in the detection regime of the PLE signal. Thus, contributions from local defect states effecting the actual transition energy may systematically change the measurements. Furthermore, quantum confinement as the backbone of the calculation is in question if there is no confinement of holes at all, as the XPS measurements indicate. Moreover, the system was microscopically simulated, suggesting a VB offset as large as 400 meV, in conflict with both experimental results. Therefore, the influence of nitrogen and strain mandate

further research on this topic, raising the question of their impact on the band offset between the materials and maybe shedding light on microscopic behavior of interfacial nitrogen states.

Additionally, the XPS measurements yield two other offsets in the heterostructure. The (B,Ga)(As,P) to GaP offset is found to be effectively zero, thus all of the offset between the two materials occur in the conduction band. Finally, the measurements yield a VB offset of 220 meV between GaP and Si. Hence, the materials align in a type II configuration. These findings contradict values from the literature, which unanimously report a type I alignment of this offset. However, the literature values cover vast ranges from −2.26 eV to −0.25 eV, suggesting that the microscopic structure of the interface may have a strong influence on the VB offset. Since nucleation of the GaP layer in the sample's suppresses a polar interface and APBs, the VB offset may deviate strongly from the previous literature values. The role of interface functionalization appears to be an interesting topic for future investigations.

Additionally, the valence-band offset should be determined by UPS as this technique provides better energy resolutions. Ideally, structures with ultra-thin cap layers should be used in order to avoid the destructive sputtering of the different layers and gaining depth information by tilting the sample. This would lead to a greatly enhanced accuracy of the spectrum and thus, of more exact offset values. Another property in the PLE spectrum revealed unexpected resonances in the energy region between the active layer contributions and GaP resonances. The underlying process of these features is not yet clear, but they may arising from VB mixing, thus influencing the VB structure and position strongly. A future conjunction of UPS and PLE measurements in combination with DFT simulations may offer a unique opportunity to find out more about the nature of the resonances and the understanding of the structure as a whole.

The second topic involves the characterization of the absolute SHG efficiencies in potassium niobate. The experimental findings reproduce the DFT results in a broad frequency range, rendering the material a very strong and promising second harmonic emitter in the measured regime. Furthermore, the material generates the fourth harmonic by cascaded second generation, i.e., resonances of the SHG at twice the incident photon energy appear in the measured SHG intensity. This may arise from Fe mediated ferroelectric domains inside the material, because they may offer a permanent polarization in the material. The complete microscopic nature of the process is still not fully clear, but the measurements indicate a very strong conjunction of SHG and its cascade. This would render potassium niobate a rare material exhibiting this behavior and calls for further research on the topic. A first approach could be to investigate the internal domain structures with SHG microscopy in order to create 3D mapping and simulation of the structures internal interfacial SHG emission, since any of the interfaces would give rise to a cascaded emission of SHG.

The last part of the thesis deals with white-light emission of amorphous cluster molecules. Here, PL and WLG experiments characterize newly synthetized materials with replaced aromatic ligands with a coinage metal molecular complex. The Ag and Au substituted clusters show strong white-light emission and a similar PL to the prototypical [$(PhSn)_4S_6$]. In contrast, the copper substituted cluster does not show any conversion process: neither white-light nor SHG. The PL reveals that the copper leads to a strong emission in the green and infrared region of the spectrum, suppressing non-linear effects effectively. Therefore, the copper complex either generates electronic levels, which suppress the effect on each molecule. Alternatively, the copper alters

the arrangement of neighboring molecules, such that the intermediate inter-molecular mixing states suppress the light emission. Further experiments reveal an amorphization of the structures under laser irradiation, thus no investigation of effects between crystalline and amorphous states is possible. However, the experiments corroborate the prior assumption that solely the π-ligand system and the macroscopic habit influence the generation of white-light and that even a slight molecular substitution can hinder the process completely.

In conclusion, the presented thesis attempts to answer certain questions regarding the material systems under study. Also, further interesting research questions opend up in the course of this thesis. Hence, this thesis provides a first step towards the understanding of the underlying physics of the discussed phenomena.

List of Figures

Bibliography

[1] J. Bardeen and W. H. Brattain, "The Transistor, A Semi-Conductor Triode", Phys. Rev. **74**, 230–231 (1948).

[2] *The Chip that Jack Built*, `http://www.ti.com/corp/docs/kilbyctr/jackbuilt.shtml#`, Date accessed: 21.06.2019.

[3] J. Kilby, "Invention of the integrated circuit", IEEE Transactions on Electron Devices **23**, 648–654 (1976).

[4] J. S. Kilby, *Miniaturized electronic circuits*, Feb. 1959.

[5] Y. Kolic et al., "Electron powder ribbon polycrystalline silicon plates used for porous layer fabrication", Thin Solid Films **255**, 159–162 (1995).

[6] S. Mizushima, M. Ueki, and K. Fujii, "Mass measurement of 1 kg silicon spheres to establish a density standard", Metrologia **41**, S68–S74 (2004).

[7] T. Monz et al., "Realization of a scalable Shor algorithm.", Science (New York, N.Y.) **351**, 1068–70 (2016).

[8] T. C. Berners-Lee and R. Cailliau, *Proposal for a HyperText Project*, tech. rep. (CERN, 1990).

[9] T. H. Maiman, "Stimulated Optical Radiation in Ruby", Nature **187**, 493–494 (1960).

[10] R. N. Hall et al., "Coherent Light Emission From GaAs Junctions", Phys. Rev. Lett. **9**, 366–368 (1962).

[11] H. J. Round, "A note on carborundum", Electrical World **19**, 309 (1907).

[12] N. Zheludev, "The life and times of the LED — a 100-year history", Nature Photonics **1**, 189–192 (2007).

[13] N. Holonyak and S. F. Bevacqua, "Coherent (Visible) Light Emission from Ga($As_{1-x}P_x$) Junctions", Appl. Phys. Lett. **1**, 82–83 (1962).

[14] M. Iwamoto and A. Kasami, "Observation of dark line defects in GaP green LED's under an external uniaxial stress", Appl. Phys. Lett. **28**, 591–592 (1976).

[15] S. Nakamura, T. Mukai, and M. Senoh, "High-Power GaN P-N Junction Blue-Light-Emitting Diodes", Jap. J. Appl. Phys **30**, L1998–L2001 (1991).

[16] G. Harbers et al., *Integrated LED based illumination device*, Sept. 2013.

[17] The Commision of th European Communities, "Commission Regulation (EC) No 244/2009 of 18 March 2009", Official Journal of the European Union **L 76/3** (2009).

[18] L. Pavesi, S. Gaponenko, and L. Negro, eds., *Towards the First Silicon Laser* (Springer Netherlands, Dordrecht, 2003).

[19] F. Idachaba, D. U. Ike, and O. Hope, "Future Trends in Fiber Optics Communication", in Proceedings of the world congress on engineering 2014 vol i (2014).

[20] B. Kunert et al., "Direct-band-gap Ga(NAsP)-material system pseudomorphically grown on GaP substrate", Appl. Phys. Lett. **88**, 182108 (2006).

[21]B. Kunert et al., "Correlation between hetero-interface properties and photoluminescence efficiency of Ga(NAsP)/(BGa)P multi-quantum well structures on (0 0 1) Si substrate", J. Crys. Growth **315**, 28–31 (2011).

[22]S. Liebich et al., "Laser operation of Ga(NAsP) lattice-matched to (001) silicon substrate", Appl. Phys. Lett. **99**, 071109 (2011).

[23]N. W. Rosemann et al., "A highly efficient directional molecular white-light emitter driven by a continuous-wave laser diode", Science **352**, 1301–1304 (2016).

[24]A. M. Zheltikov, "Let there be white light: supercontinuum generation by ultrashort laser pulses", Phys.-Usp. **49**, 605 (2006).

[25]N. W. Rosemann et al., "Organotetrel Chalcogenide Clusters: Between Strong Second-Harmonic and White-Light Continuum Generation", Journal of the American Chemical Society **138**, 16224–16227 (2016).

[26]C. F. Klingshirn, *Semiconductor optics*, Vol. 53, 9 (2012).

[27]C. Schneider et al., "An electrically pumped polariton laser", Nature **497**, 348–352 (2013).

[28]A. Imamog¯lu et al., "Nonequilibrium condensates and lasers without inversion: Exciton-polariton lasers", Phys. Rev. A **53**, 4250–4253 (1996).

[29]Z. Chen et al., "Radiative cooling to deep sub-freezing temperatures through a 24-h day-night cycle", Nature Communications **7**, 1–5 (2016).

[30]A. Amo et al., "Exciton–polariton spin switches", Nature Photonics **4**, 361–366 (2010).

[31]P. G. Savvidis et al., "Angle-Resonant Stimulated Polariton Amplifier", Phys. Rev. Lett. **84**, 1547–1550 (2000).

[32]A. Chernikov et al., "Exciton binding energy and nonhydrogenic Rydberg series in monolayer WS_2", Phys. Rev. Lett. **113**, 1–5 (2014).

[33]J. Voigt, F. Spiegelberg, and M. Senoner, "Band parameters of CdS and CdSe single crystals determined from optical exciton spectra", Physica Status Solidi (b) **91**, 189–199 (1979).

[34]S. B. Nam et al., "Free-exciton energy spectrum in GaAs", Phys. Rev. B **13**, 761 (1976).

[35]F. Bloch, "Bemerkung zur Elektronentheorie des Ferromagnetismus und der elektrischen Leitfähigkeit", Zeitschrift für Physik **57**, 545–555 (1929).

[36]A. Sommerfeld, "Zur Elektronentheorie der Metalle auf Grund der Fermischen Statistik", Zeitschrift für Physik **47**, 1–32 (1928).

[37]M. Grundmann, *The Physics of Semiconductors*, 3. edition (Springer International Publishing, Leipzig, Germany, 2016).

[38]R. Kronig and W. G. Penney, "Quantum Mechanics of Electrons in Crystal Lattices", Proceedings of the Royal Society A: Mathematical, Physical and Engineering Sciences **130**, 499–513 (1931).

[39]K. Seeger, *Semiconductor physics*, edited by H. K. V. Lotsch, 3. edition (Springer-Verlag, Heidelberg, 1989).

[40]N. N. Anua et al., "DFT investigations of structural and electronic properties of gallium arsenide (GaAs)", in Aip conference proceedings, Vol. 1482, 1 (Sept. 2012), pp. 64–68.

[41]L. C. Bannow et al., "An ab initio based approach to optical properties of semiconductor heterostructures", Modelling and Simulation in Materials Science and Engineering **25**, 065001 (2017).

[42]Y. Varshni, "Temperature dependence of the energy gap in semiconductors", Physica **34**, 149–154 (1967).

[43]R. Pässler, "Parameter Sets Due to Fittings of the Temperature Dependencies of Fundamental Bandgaps in Semiconductors", physica status solidi (b) **216**, 975–1007 (1999).

[44]G. H. Wannier, "The Structure of Electronic Excitation Levels in Insulating Crystals", Phys. Rev. **52**, 191–197 (1937).

[45]J. Frenkel, "On the Transformation of light into Heat in Solids", Phys. Rev. **37**, 17–44 (1931).

[46]M. Kira and S. Koch, "Many-body correlations and excitonic effects in semiconductor spectroscopy", Progress in Quantum Electronics **30**, 155–296 (2006).

[47]S. W. K. Koch and M. Kira, "Excitons in Semiconductor", in *Optics of semiconductors and their nanostructure*, edited by H. Kalt and M. Hetterich (Springer-Verlag, Berlin Heidelberg, 2004) Chap. Excitons i, p. 1.

[48]H. Haug and S. W. K. Koch, *Quantum theory of the optical and electronic properties of semiconductors* (World Scientific Publishing, Singapore, 2004).

[49]R. J. Elliott, "No Title", in *Polarons and excitons*, edited by C. Kuper, O. Whitefield, and Boyd (1963), p. 269.

[50]P. D. Dapkus et al., "Kinetics of recombination in nitrogendoped GaP", J. Appl. Phys. **45**, 4920–4930 (1974).

[51]P. R. C. Kent, L. Bellaiche, and A. Zunger, "Pseudopotential theory of dilute III-V nitrides", Semicond. Sci. Technol. **17**, 851 (2002).

[52]J. Wu, W. Shan, and W. Walukiewicz, "Related content Band anticrossing in highly mismatched III-V semiconductor alloys", Semicond. Sci. Technol **17**, 860–869 (2002).

[53]C. Skierbiszewski, "Experimental studies of the conduction-band structure of GaInNAs alloys", Semicond. Sci. Technol. **17**, 803–814 (2002).

[54]K. Alberi et al., "Valence-band anticrossing in mismatched III-V semiconductor alloys", Phys. Rev. B **75**, 045203 (2007).

[55]D. E. Aspnes and M. Cardona, "Strain dependence of effective masses in tetrahedral semiconductors", Phys. Rev. B **17**, 726 (1978).

[56]P. Auger, "Sur les rayons β secondaires produits dans un gaz par des rayons X", C.R.A.S. **177**, 169 (1923).

[57]L. Meitner, "Über die Entstehung der Beta-Strahl-Spektren radioaktiver Substanzen", Zeitschrift für Physik **9**, 131–144 (1922).

[58]M. Takeshima, "Phonon-assisted Auger recombination in a quasi-two-dimensional structure semiconductor", Phys. Rev. B **30**, 3302 (1984).

[59]I. BarJoseph et al., "Quantumconfined Stark effect in InGaAs/InP quantum wells grown by organometallic vapor phase epitaxy", Appl. Phys. Lett. **50**, 1010–1012 (1987).

[60] D. L. Wood and J. Tauc, "Weak Absorption Tails in Amorphous Semiconductors", Phys. Rev. B **5**, 3144–3151 (1972).

[61] E. Kurtz et al., "Suppression of lateral fluctuations in CdSe-based quantum wells", Appl. Phys. Lett. **79**, 1118–1120 (2001).

[62] O. Rubel et al., "Quantitative description of disorder parameters in (GaIn)(NAs) quantum wells from the temperature-dependent photoluminescence spectroscopy", J. Appl. Phys. **98**, 063518 (2005).

[63] S. D. Baranovskii, R. Eichmann, and P. Thomas, "Temperature-dependent exciton luminescence in quantum wells by computer simulation", Phys. Rev. B **58**, 13081–13087 (1998).

[64] P. A. Franken et al., "Generation of Optical Harmonics", Phys. Rev. Lett. **7**, 118–119 (1961).

[65] D. A. Kleinman, "Nonlinear Dielectric Polarization in Optical Media", Phys. Rev. **126**, 1977–1979 (1962).

[66] R. C. Miller, "Optical Second Harmonic Generation in Piezoelectric Crystals", Appl. Phys. Lett. **5**, 17–19 (1964).

[67] G. R. Crane and J. G. Bergman, "Violations of Kleinman symmetry in nonlinear optics: The forbidden coefficient of αquartz", The Journal of Chemical Physics **64**, 27–29 (1976).

[68] G. Ghosh, "Sellmeier coefficients and dispersion of thermo-optic coefficients for some optical glasses", Applied Optics **36**, 1540 (1997).

[69] R. W. Boyd, *Nonlinear optics* (Elsevier Science & Technology, 2003).

[70] R. Danielius et al., "Matching of group velocities by spatial walk-off in collinear three-wave interaction with tilted pulses", Optics Letters **21**, 973 (1996).

[71] J. D. Zook, D. Chen, and G. N. Otto, "Temperature Dependence and Model of the Electro-Optic Effect in $LiNbO_3$", Appl. Phys. Lett. **11**, 159–161 (1967).

[72] R. C. Miller and A. Savage, "Temperature Dependence of the Optical Properties of Ferroelectric $LiNbO_3$ and $LiTaO_3$", Appl. Phys. Lett. **9**, 169–171 (1966).

[73] J. E. Midwinter and J. Warner, "The effects of phase matching method and of crystal symmetry on the polar dependence of third-order non-linear optical polarization", British Journal of Applied Physics **16**, 1667–1674 (1965).

[74] J. E. Midwinter and J. Warner, "The effects of phase matching method and of uniaxial crystal symmetry on the polar distribution of second-order non-linear optical polarization", British Journal of Applied Physics **16**, 1135–1142 (1965).

[75] J. A. Armstrong et al., "Interactions between Light Waves in a Nonlinear Dielectric", Phys. Rev. **127**, 1918 (1962).

[76] M. Yamada et al., "Firstorder quasiphase matched LiNbO 3 waveguide periodically poled by applying an external field for efficient blue secondharmonic generation", Appl. Phys. Lett. **62**, 435–436 (1993).

[77] R. L. Byer, "Quasi-Phasematched Nonlinear Interactions and Devices", Journal of Nonlinear Optical Physics & Materials **06**, 549–592 (1997).

[78] P. D. Maker et al., "Effects of Dispersion and Focusing on the Production of Optical Harmonics", Phys. Rev. Lett. **8**, 21 (1962).

[79] J. Manley and H. Rowe, "Some General Properties of Nonlinear Elements-Part I. General Energy Relations", Proceedings of the IRE **44**, 904–913 (1956).

[80] H. Rowe, "Some General Properties of Nonlinear Elements. II. Small Signal Theory", Proceedings of the IRE **46**, 850–860 (1958).

[81] C. R. Gouy, "No Title", Acad. Sci. Paris **110**, 1251 (1890).

[82] G. D. Boyd and D. A. Kleinman, "Parametric Interaction of Focused Gaussian Light Beams", J. Appl. Phys. **39**, 3597–3639 (1968).

[83] D. A. Kleinman, A. Ashkin, and G. D. Boyd, "Second-Harmonic Generation of Light by Focused Laser Beams", Phys. Rev. **145**, 338–379 (1966).

[84] N. Bloembergen and P. S. Pershan, "Light Waves at the Boundary of Nonlinear Media", Phys. Rev. **128**, 606–622 (1962).

[85] J. C. Knight et al., "All-silica single-mode optical fiber with photonic crystal cladding", Optics Letters **21**, 1547 (1996).

[86] J. Kerr, "A new relation between electricity and light: Dielectrified media birefringent", The London, Edinburgh, and Dublin Philosophical Magazine and Journal of Science **50**, 337–348 (1875).

[87] P. F. Moulton, "Ti-doped sapphire: tunable solid-state laser", Optics News **8**, 9 (1982).

[88] A. Stingl et al., "Sub-10-fs mirror-dispersion-controlled Ti:sapphire laser", Optics Letters **20**, 602 (1995).

[89] R. R. Alfano and S. L. Shapiro, "Observation of Self-Phase Modulation and Small-Scale Filaments in Crystals and Glasses", Phys. Rev. Lett. **24**, 592–594 (1970).

[90] R. R. Alfano and S. L. Shapiro, "Emission in the Region 4000 to 7000 Å Via Four-Photon Coupling in Glass", Phys. Rev. Lett. **24**, 584–587 (1970).

[91] M. Segev et al., "Spatial solitons in photorefractive media", Phys. Rev. Lett. **68**, 923–926 (1992).

[92] P. N. Ghosh, "Davydov splitting and multipole interactions", Solid State Comm. **19**, 639–642 (1976).

[93] E. Hückel, "Quantentheoretische Beiträge zum Benzolproblem", Zeitschrift für Physik **70**, 204–286 (1931).

[94] M. Knupfer, "Exciton binding energies in organic semiconductors", Appl. Phys. A **77**, 623–626 (2003).

[95] J. Franck and E. G. Dymond, "Elementary processes of photochemical reactions", Transactions of the Faraday Society **21**, 536 (1926).

[96] E. Condon, "A Theory of Intensity Distribution in Band Systems", Phys. Rev. **28**, 1182–1201 (1926).

[97] D. E. Aspnes, "Bond models in linear and nonlinear optics", physica status solidi (b) **247**, 1873–1880 (2010).

[98] B. F. Levine, "Bond-Charge Calculation of Nonlinear Optical Susceptibilities for Various Crystal Structures", Phys. Rev. B **7**, 2600–2626 (1973).

[99] D. J. Griffiths, *Introduction to Quantum Mechanics*, 2. ed. (Pearson Prentice-Hall, Upper Saddle River, NJ, 2005), p. 62.

[100] Frank and van de Merwe, "One-dimensional dislocations - III. Influence of the second harmonic term in the potential representation, on the properties of the model", Proceedings of the Royal Society of London. Series A. Mathematical and Physical Sciences **200**, 125–134 (1949).

[101] M. Volmer and A. Weber, "Keimbildung in übersättigten Gebilden", Z. Phys. Chem. **119**, 227 (1926).

[102] I. N. Stranski and L. Krastanow, "Zur Theorie der orientierten Ausscheidung von Ionenkristallen aufeinander", Sitzungsberichte d. Akad. d. Wissenschaften in Wien **146**, 797 (1938).

[103] B. Daudin et al., "Stranski-Krastanov growth mode during the molecular beam epitaxy of highly strained GaN", Phys. Rev. B **56**, R7069 (1997).

[104] K. Volz et al., "GaP-nucleation on exact Si (0 0 1) substrates for III/V device integration", J. Crys. Growth **315**, 37–47 (2011).

[105] S. Nakamura et al., "InGaN-Based Multi-Quantum-Well-Structure Laser Diodes", Jap. J. Appl. Phys **35**, L74–L76 (1996).

[106] C. G. Van De Walle and J. Neugebauer, "Universal alignment of hydrogen levels in semiconductors, insulators and solutions", Nature **423**, 626 (2003).

[107] J.-Y. Yeh et al., "Characteristics of InGaAsN-GaAsSb type-II "W" quantum wells", J. Crys. Growth **287**, 615–619 (2006).

[108] J. Hu et al., "Type II photoluminescence and conduction band offsets of GaAsSb/InGaAs and GaAsSb/InP heterostructures grown by metalorganic vapor phase epitaxy", Appl. Phys. Lett. **73**, 2799–2801 (1998).

[109] J. R. Meyer et al., "TypeII quantumwell lasers for the midwavelength infrared", Appl. Phys. Lett. **67**, 757–759 (1995).

[110] J. Faist et al., "Quantum Cascade Laser", Science **264**, 553 (1994).

[111] F. Stern and S. Das Sarma, "Electron energy levels in GaAs-$Ga_{1-x}Al_xAs$ heterojunctions", Phys. Rev. B **30**, 840–848 (1984).

[112] A. Sommerfeld, "Über die Beugung und Bremsung der Elektronen", Annalen der Physik **403**, 257–330 (1931).

[113] R. P. Leavitt and J. W. Little, "Simple method for calculating exciton binding energies in quantum-confined semiconductor structures", Phys. Rev. B **42**, 11774 (1990).

[114] D. B. T. Thoai et al., "Image charges in semiconductor quantum wells: Effect on exciton binding energy", Phys. Rev. B **42**, 5906 (1990).

[115] M. J. L. S. Haines et al., "Exciton-binding-energy maximum in $Ga_{1-x}In_xAs$/GaAs quantum wells", Phys. Rev. **43**, 11944 (1991).

[116] R. C. Miller et al., "Extrinsic photoluminescence from GaAs quantum wells", Phys. Rev. B **25**, 3871 (1982).

[117] W. T. Masselink, Y.-C. Chang, and H. Morkoç, "Binding energies of acceptors in GaAs-Al"Gal "As quantum wells", Phys. Rev. B **28**, 7373 (1983).

[118] A. Einstein, "Über einen die Erzeugung und Verwandlung des Lichtes betreffenden heuristischen Gesichtspunkt", Annalen der Physik **322**, 132–148 (1905).

[119] P. J. Feibelman and D. E. Eastman, "Photoemission spectroscopy—Correspondence between quantum theory and experimental phenomenology", Phys. Rev. B **10**, 4932–4947 (1974).

[120] T. Koopmans, "Über die Zuordnung von Wellenfunktionen und Eigenwerten zu den Einzelnen Elektronen Eines Atoms", Physica **1**, 104–113 (1934).

[121] S. Suga and A. Sekiyama, *Photoelectron Spectroscopy*, Vol. 176, Springer Series in Optical Sciences (Springer Berlin Heidelberg, Berlin, Heidelberg, 2014).

[122] E. Saloman, J. Hubbell, and J. Scofield, "X-ray attenuation cross sections for energies 100 eV to 100 keV and elements Z = 1 to Z = 92", Atomic Data and Nuclear Data Tables **38**, 1–196 (1988).

[123] R. F. Reilman, A. Msezane, and S. T. Manson, "Relative intensities in photoelectron spectroscopy of atoms and molecules", Journal of Electron Spectroscopy and Related Phenomena **8**, 389–394 (1976).

[124] I. C. Secretary, *Surface chemical analysis – X-ray photoelectron spectrometers – Calibration of energy scales*, tech. rep. (International Organization for Standardization, Geneva, CH, 2010).

[125] J. F. Moulder et al., *Handbook of X-ray Photoelectron Spectroscopy*, edited by J. Chastain and R. C. King (Physical Electronics, Inc., Eden Prairie, Minnesota, USA, 1995).

[126] H. S. Hansen and S. Tougaard, "Separation of spectral components and depth profiling through inelastic background analysis of XPS spectra with overlapping peaks", Surface and Interface Analysis **17**, 593–607 (1991).

[127] D. A. Shirley, "High-Resolution X-Ray Photoemission Spectrum of the Valence Bands of Gold", Phys. Rev. B **5**, 4709–4714 (1972).

[128] S. Tougaard, "Accuracy of the Non-destructive Surface Nanostructure Quantification Technique Based on Analysis of the XPS or AES Peak Shape", Surface and Interface Analysis **26**, 249–269 (1998).

[129] D. W. Marquardt, "An Algorithm for Least-Squares Estimation of Nonlinear Parameters", Journal of the Society for Industrial and Applied Mathematics **11**, 431–441 (1963).

[130] S. G. Lieb, "Simplex Method of Nonlinear Least-Squares - A Logical Complementary Method to Linear Least-Square Analysis of Data", J. Chem. Education **74**, 1008 (1997).

[131] T. Löher et al., "Partial Density of States in the $CuInSe_2$ Valence Vands", J. Appl. Phys. **81**, 7806–7809 (1997).

[132] J. Yeh and I. Lindau, "Atomic subshell photoionization cross sections and asymmetry parameters: 1 Z 103", Atomic Data and Nuclear Data Tables **32**, 1–155 (1985).

[133] F. Capasso, "Band-Gap Engineering: From Physics and Materials to New Semiconductor Devices", Science **235**, 172 (1987).

[134] F. M. Ryan and R. C. Miller, "The Effect of Uniaxial Strain on the Threshold Current and Output of GaAs Lasers", Appl. Phys. Lett. **3**, 162–163 (1963).

[135] P. J. Klar et al., "From N isoelectric impurities to N-induced bands in the GaN_xAs_{1-x} alloy", Appl. Phys. Lett. **76**, 3439 (2000).

[136] N. Sommer et al., "Growth of (BGa)As, (BGa)P, (BGa)(AsP) and (BGaIn)P by MOVPE", J. Crys. Growth **370**, 191–196 (2013).

[137]B. Paulus, P. Fulde, and H. Stoll, "Cohesive energies of cubic III-V semiconductors", Phys. Rev. B **54**, 2556 (1996).

[138]Y. Cai et al., "Infrared reflectance spectrum of BN calculated from first principles", Solid State Communications **141**, 262–266 (2007).

[139]B. Kunert et al., "Annealing experiments of the GaP based dilute nitride Ga(NAsP)", Physica status solidi (a) **205**, 114–119 (2008).

[140]H. Kroemer, "Polar-on-nonpolar Epitaxy", J. Crys. Growth **81**, 193–204 (1987).

[141]P. Ludewig et al., "MOVPE growth studies of Ga(NASP)/(BGA)(ASP) multi quantum well heterostructures (MQWH) for the monolithic integration of laser structures on (001) Si-substrates", J. Crys. Growth **438**, 63–69 (2016).

[142]T. Wegele et al., "Interface morphology and composition of Ga(NAsP) quantum well structures for monolithically integrated LASERs on silicon substrates", Journal of Physics D: Applied Physics **49**, 075108 (2016).

[143]K. Jandieri et al., "Compositional dependence of the band gap in Ga(NAsP) quantum well heterostructures", J. Appl. Phys. **118** (2015).

[144]S. Borck et al., "Lasing in optically pumped Ga(NAsP)/GaP heterostructures", Appl. Phys. Lett. **89**, 031102 (2006).

[145]M. Hofmann et al., "Emission dynamics and optical gain of 1.3-μm (GaIn)(NAs)/GaAs lasers", IEEE Journal of Quantum Electronics **38**, 213–221 (2002).

[146]Beer, "Bestimmung der Absorption des rothen Lichts in farbigen Flüssigkeiten", Annalen der Physik und Chemie **162**, 78–88 (1852).

[147]M. P. Seah and W. A. Dench, "Quantitative electron spectroscopy of surfaces: A standard data base for electron inelastic mean free paths in solids", Surface and Interface Analysis **1**, 2–11 (1979).

[148]G. Padeletti and G. M. Ingo, "Factors determining preferential sputtering in InGaAs system: angle-resolved small-area XPS investigation", Surf. Inter. Analysis **34**, 266–270 (2002).

[149]N. Sanada et al., "Extremely low sputtering degradation of polytetrafluoroethylene by C60 ion beam applied in XPS analysis", Surf. Inter. Analysis **36**, 280–282 (2004).

[150]A. Zalar, "Improved depth resolution by sample rotation during Auger electron spectroscopy depth profiling", Thin Solid Films **124**, 223–230 (1985).

[151]M. Kawabe et al., "Effects of ion etching on the properties of GaAs", Applied Optics **17**, 2556 (1978).

[152]J. Tauc, R. Grigorovici, and A. Vancu, "Optical Properties and Electronic Structure of Amorphous Germanium", Physica Status Solidi (B) **15**, 627–637 (1966).

[153]E. A. Kraut et al., "Semiconductor core-level to valence-band maximum binding-energy differences: Precise determination by x-ray photoelectron spectroscopy", Phys. Rev. B **28**, 1965–1977 (1983).

[154]J. R. Chelikowsky and M. L. Cohen, "Nonlocal pseudopotential calculations for the electronic structure of eleven diamond and zinc-blende semiconductors", Phys. Rev. B **14**, 556 (1976).

[155]E. Kraut et al., "Precise Determination of the Valence-Band Edge in X-Ray Photoemission Spectra: Application to Measurement of Semiconductor Interface Potentials", Phys. Rev. Lett. **44**, 1620–1623 (1980).

[156]M. Shakfa et al., "Carrier dynamics in Ga(NAsP)/Si multi-quantum well heterostructures with varying well thickness", Superlattices and Microstructures **93**, 67–72 (2016).

[157]Y. Zhang et al., "Valence-band splitting and shear deformation potential of dilute $GaAs_{1-x}N_x$ alloys", Phys. Rev. B **61**, 4433 (2000).

[158]S.-H. Wei, S. B. Zhang, and A. Zunger, "First-principles calculation of band offsets, optical bowings, and defects in CdS, CdSe, CdTe, and their alloys", J. Appl. Phys. **87**, 1304 (2000).

[159]J. O. Oelerich et al., "Ab-initio Calculation of Band Alignments for Opto-Electronic Simulations", AIP Advances **9**, 055328 (2019).

[160]D. A. Papaconstantopoulos, "Free-Electron-Like Metals of Groups III and IV", in *Handbook of the band structure of elemental solids* (Springer US, Boston, MA, 2015), pp. 305–336.

[161]N. J. Shevchik, J. Tejeda, and M. Cardona, "Densities of valence states of amorphous and crystalline III-V and II-VI semiconductors", Phys. Rev. B **9**, 2627–2648 (1974).

[162]E. T. Yu et al., "Measurement of the valenceband offset in strained Si/Ge (100) heterojunctions by xray photoelectron spectroscopy", Appl. Phys. Lett. **56**, 569–571 (1990).

[163]S. Adachi, "III-V Ternary and Quaternary Compounds", in *Springer handbook of electronic and photonic materials* (2017), p. 725.

[164]W. D. Grobman and D. E. Eastman, "Photoemission Valence-Band Densities of States for Si, Ge, and GaAs Using Synchrotron Radiation", Phys. Rev. Lett. **29**, 1508–1512 (1972).

[165]L. Ostheim, "Effekt der von Bor und Stickstoff induzierten isovalenten Störstellen auf den Leitungsbandtransport in III-V-Halbleitern", PhD thesis (Justus-Liebig University, Gießen, 2018).

[166]I. Sakata and H. Kawanami, "Band Discontinuities in Gallium Phosphide/Crystalline Silicon Heterojunctions Studied by Internal Photoemission", Appl. Phys. Exp. **1**, 091201 (2008).

[167]P. Perfetti et al., "Experimental study of the GaP-Si interface", Phys. Rev. B **30**, 4533–4539 (1984).

[168]D. F. Nelson, *Nonlinear Dielectric Susceptibilities*, edited by D. F. Nelson, Vol. 30b, Landolt-Börnstein - Group III Condensed Matter (Springer-Verlag, Berlin/Heidelberg, 2000).

[169]S. De Zhong, "Recent developments in the growth and nonlinear optical applications of $KNbO_3$ crystals", Progress in Crystal Growth and Characterization of Materials **20**, 161–174 (1990).

[170]Y. Uematsu, "Nonlinear Optical Properties of KNbO3 Single Crystal in the Orthorhombic Phase", Jap. J. Appl. Phys **13**, 1362 (1974).

[171]Z. Lu and M. Xiao, "Observation of localized domain reversal of iron-doped potassium niobate (Fe: $KNbO_3$) single crystal", J. Appl. Phys. **76**, 4451 (1994).

[172] N. W. Rosemann et al., "White-Light Generation through Nonlinear Optical versus Crystalline States", Adv. Opt. Mat. **1701162**, 1–4 (2018).

[173] J. Jerphagnon and S. K. Kurtz, "Maker fringes: A detailed comparison of theory and experiment for isotropic and uniaxial crystals", J. Appl. Phys. **41**, 1667–1681 (1970).

[174] G. Ghosh, "Dispersion-equation coefficients for the refractive index and birefringence of calcite and quartz crystals", Optics Communications **163**, 95–102 (1999).

[175] B. Zysset, I. Biaggio, and P. Gunter, "Refractive indices of orthorhombic $KNbO_3$. I. Dispersion and temperature dependence", Journal of the Optical Society of America B **9**, 380–386 (1992).

[176] F. Schmidt et al., "Quasiparticle and excitonic effects in the optical response of $KNbO_3$", Phys. Rev. Materials **3**, 054401–1 (2019).

[177] P. Gunter and F. Micheron, "Photorefractive effects and photocurrents in $KNbO_3$:Fe", Ferroelectrics **18**, 27–38 (1978).

[178] E. V. Melik-Gaykazyan et al., "Third-harmonic generation from Mie-type resonances of isolated all-dielectric nanoparticles Subject Areas : Author for correspondence :" Phil. Trans. R. Soc. A **375**, 20160281 (2017).

[179] G. D'Aguanno et al., "Enhancement of χ^2 cascading processes in one-dimensional photonic bandgap structures", Optics Letters **24**, 1663 (1999).

[180] Sellmeier, "Zur Erklärung der abnormen Farbenfolge im Spectrum einiger Substanzen", Annalen der Physik und Chemie **219**, 272–282 (1871).

[181] E. Dornsiepen et al., "WhiteLight Generation Upon InSitu Amorphization of Single Crystals of [$(Me_3P)_3$ $AuSn(PhSn)_3S_6$] and [$(Et_3P)_3AgSn(PhSn)_3S_6$]", Adv. Opt. Mat., 1801793 (2019).

A | Appendix

Continuity relation for the electric and magnetic field at an interface

The continuity relations for the electric and magnetic field at the interface are

$$R_x E_R = f_x A_f + b_x E_{\mathrm{NL}} \tag{A.1}$$
$$R_y k_{Rz} E_R = f_y k_{fz} A_f + b_y k_{bz} E_{\mathrm{NL}} \tag{A.2}$$
$$R_y E_R = f_y k_{fz} A_f + p_y k_{bz} E_{\mathrm{NL}} \tag{A.3}$$
$$(R_x k_{Rz} - R_z k_{Rx}) E_R = (f_x k_{fz} - f_z k_{fx})\, A_f + (p_x k_{bz} - p_z k_{bx})\, E_{\mathrm{NL}}. \tag{A.4}$$

With the relation $f_i = \mathbf{e}_i \cdot \mathbf{e}_f$ and similar for $\mathbf{e}_b$, $\mathbf{e}_p$ and $\mathbf{e}_R$, where $\mathbf{e}_i$ represents an unit vector along a coordinate axis ($i = x, y, z$). In general it is necessary to separately calculate the parallel or perpendicular nonlinear polarization with respect to the plane of incidence. However, for normal incidence of the fundamental beam the two solutions are equal. Therefore only one case will be calculated here (for complete discussion see Bloembergen and Pershan[84]). In the calculation the angle dependence will be kept and the angles will be set to zero in the final formula.

$$E_{2\omega} \exp\left(\mathrm{i}\mathbf{k}_f \cdot \mathbf{e}_z L\right) \tag{A.5}$$
$$+\frac{\omega^2 P_{\mathrm{NLS}}}{\epsilon_0 c^2 (n_{2\omega}^2 - n_\omega^2)} \exp\left(\mathrm{i}\mathbf{k}_b \cdot \mathbf{e}_z L\right) \tag{A.6}$$
$$+E_{2\omega}^R \exp\left(-\mathrm{i}\mathbf{k}_f \cdot \mathbf{e}_z L\right) \tag{A.7}$$
$$=E_{2\omega}^{\mathrm{out}} \exp\left(2\mathrm{i}\mathbf{k}_\omega \cdot \mathbf{e}_z L\right) \tag{A.8}$$

The light intensity of the light through a slab of thickness L is then

$$8 n_{2\omega} \cos\theta_{2\omega} P_{\mathrm{NLS}} \frac{(n_\omega \cos\theta_\omega + n_{2\omega} \cos\theta_{2\omega})(\cos\theta_{2\omega}^R + n_\omega \cos\theta_\omega)}{c^2(\cos\theta + n_{2\omega}\cos\theta_{2\omega})^3} \cdot \frac{\sin^2\left[\pi L/(2l_c)\right]}{(n_{2\omega}^2 - n_\omega^2)^2}. \tag{A.9}$$

Correction terms for the SBEs

$$\frac{\partial}{\partial t} P_{\mathbf{k}}(t) = -\Gamma_{\mathbf{k}}(t) P_{\mathbf{k}}(t) + \sum_{\mathbf{k}'} \Gamma_{\mathbf{k},\mathbf{k}'}(t) P_{\mathbf{k}'}(t) \tag{A.10}$$

$$\frac{\partial}{\partial t} f_{\mathbf{k}}^a(t) = -\Sigma_{\mathbf{k}}^{out,a}(t) f_{\mathbf{k}}^a(t) + \Sigma_{\mathbf{k}}^{in,a}(t)\left[1 - f_{\mathbf{k}}^a(t)\right] + \Sigma_{\mathbf{k}}^{pol,a}(t) \tag{A.11}$$

Table A.1: Low temperature material parameters

Parameter	GaAs	GaP	GaN
a_0 (Å)	5.6424	5.4423	4.4867[1]
E_Γ (eV)	1.519	2.886	-[2]
E_X (eV)	-	2.35	-
E_N (eV)	1.65	2.18	-
Δ_0 (eV)	0.34	0.08	-
α_Γ (eV)	-7.17	-8.2	-
α_v (eV)	-1.16	-1.7	-
α_N (meV/GPa)	40.0	1.0	-
B (eV)	-2.0	-1.6	-
C_{11} (GPa)	122.1	140.5	-
C_{12} (GPa)	56.6	62.0	-
γ_1 (arb. u.)	6.98	4.05	-
γ_2 (arb. u.)	2.06	0.98	-

Table A.2: Valence band offsets between Ga(NAsP) and GaP for different core orbitals.

Orbital	$\Delta E_{VB,DOS}$	$\Delta E_{VB,erf}$
Ga $2p_{3/2}$	$(0.00 \pm 0.02)\,eV$	$(-0.03 \pm 0.15)\,eV$
Ga $2_{1/2}$	$(0.00 \pm 0.03)\,eV$	$(-0.03 \pm 0.15)\,eV$
Ga $3_{1/2}$	$(0.02 \pm 0.02)\,eV$	$(-0.01 \pm 0.15)\,eV$
Ga $3_{1/2}$	$(0.04 \pm 0.03)\,eV$	$(0.02 \pm 0.15)\,eV$
P 2p	$(0.01 \pm 0.04)\,eV$	$(-0.01 \pm 0.15)\,eV$
P 2s	$(-0.04 \pm 0.03)\,eV$	$(-0.06 \pm 0.15)\,eV$
As 3d	$(0.08 \pm 0.05)\,eV$	$(0.06 \pm 0.15)\,eV$
Weighted average	$(0.01 \pm 0.02)\,eV$	$(-0.01 \pm 0.02)\,eV$

B | Statement of Authorship

I declare that I have completed this dissertation single-handedly without the unauthorized help of a second party and only with the assistance acknowledged therein. I have appropriately acknowledged and cited all text passages that are derived verbatim from or are based on the content of published work of others, and all information relating to verbal communications. I consent to the use of an anti-plagiarism software to check my thesis. I have abided by the principles of good scientific conduct laid down in the charter of the Justus Liebig University Giessen "Satzung der Justus-Liebig-Universität Gießen zur Sicherung guter wissenschaftlicher Praxis" in carrying out the investigations described in the dissertation.

Place, Date

Florian Dobener

C | Acknowledgements (in German)

An dieser Stelle möchte ich nochmal allen Menschen danken, die mich während meiner Promotionszeit unterstützt haben und diese Arbeit in dieser Form überhaupt erst ermöglicht haben.

An erster Stelle geht mein Dank an Sangam Chatterjee, für die Betreuung meiner Arbeit, seine Hilfe und unermüdlichen Ideen für jedes Laborproblem. Darüber hinaus geht mein Dank an die gesamte AG Spektroskopie und Optik in Marburg und Gießen. Allen voran zu nennen sind hier Robin Döring, Andre Rinn und Nils Rosemann, von denen ich wahnsinnig viel über Spektroskopie und die allgemeine Herangehensweise an wissenschaftliche, wie technische Probleme lernen konnte. Sie waren für mich ein Vorbild, wie durch Engagement und Durchhaltevermögen ein großes Wissen über ein Feld und darüber hinaus aufgebaut werden kann.

Auch meine Zeit in Gießen wurde durch viele Menschen bereichert. Ich bin dankbar für die gute Aufnahme am Institut und das freundliche Miteinander, sowie die offenen Türen bei jedwedem Problem, die ich hier kennen lernen durfte. Insbesondere möchte ich dem Gießener Teil der Arbeitsgruppe danken, denn wir haben es gemeinsam geschafft aus dem Chaos eines Arbeitsgruppenumzugs wieder eine gut funktionierende Arbeitsumgebung zu schaffen. Vor allem möchte ich Julian Veletas danken, der mir immer ein guter Büronachbar und Ansprechpartner war und immer ein offenes Ohr und Ideen für die AG und andere Probleme hatte. Weiterhin danke ich Philip Klement, der stets hilfreich dabei war sich in der neuen Gießener Umgebung zurecht zu finden und darüber hinaus wertvolles Feedback für verschiedenste Probleme lieferte. Bei allen anderen Mitgliedern der AG möchte ich mich für das gute Miteinander, die gute Zeit und angenehme Atmosphäre bedanken. Dadurch fühle ich mich jeden Tag aufs Neue wohl an meinem Arbeitsplatz.

Diese Arbeit wäre nicht möglich gewesen ohne die Kompetenz der Werkstätten, die für jedes elektrische oder mechanische Problem immer schnelle Hilfe leisten konnten. Insbesondere geht mein Dank an die elektrische und mechanische Werkstatt in Marburg, die nicht nur gute Arbeit leistete, sondern immer mir auch unermüdlich die besten Lösungen und Verbesserungsvorschläge für verschiedenste Laborprobleme lieferten.

Ein ganz besonderer Dank geht auch an die Wachser und Hersteller der Proben, ohne die ich nur Luft hätte spektroskopieren können. Für das Wachstum der MOVPE Mehrschichtsysteme danke ich Peter Ludewig und Marcel Kröner. Die Synthetisierung der adamantanartigen Clusterverbindungen wurde von Eike Dornsiepen durchgeführt. Vielen Dank dafür.

Ich danke außerdem allen Korrekturlesern für die Anmerkungen und Ideen für Verbesserungen meiner Arbeit. Ein großer Dank gilt auch Wolfram Heimbrodt, für seine Bereitschaft als Zweitgutachter dieser Dissertation zu fungieren. Der deutschen Forschungsgemeinschaft möchte ich danken für die finanzielle Unterstützung im Rahmen des GRK1782.

Meinen Eltern danke ich dafür, dass sie mir das Studium ermöglicht haben und mich darüber hinaus immer unterstützt haben.

Zuletzt geht man Dank an die Menschen, die mich abseits der Uni unterstützt haben und denen ich jederzeit mit Physik Diskussionen auf den Geist gehen konnte. Vor allem meine ich damit meine WG in der ich eine wahnsinnig angenehme Zeit hier in Gießen verbringen konnte. Darüber hinaus konnte ich immer jedes Problem mit nach Hause bringen und auch beim Schreiben wart ihr eine große Hilfe. Danke Martin. Danke Prof. Dr. Hasenbrink.

Mein größter Dank geht an Asja. Sie hat nicht nur meine sprunghafte Laune, falls mal wieder etwas nicht klappte, meine teilweise langen Arbeitsstunden und verschwiegenen Stunden in denen ich über irgendein Problem gegrübelt habe, ertragen, sondern ist und war auch immer für mich da um mich unermüdlich aufzupäppeln oder mir einen neuen Blick zu geben. Egal in welcher Situation konnte ich auf dich zählen und du warst immer für mich da, selbst wenn ich selbst unfair oder selbstsüchtig war. Ich danke dir in einem Maß, dass ich nicht in Worte fassen kann.

D | Abstract (in German)

In der vorliegenden Arbeit wurden drei verschiedene Themen behandelt, die dazu dienen die Lichtemission vorhandener Lasersystemen auf bisher unerreichte Wellenlängenbereiche zu erweitern. In der Laserspektroskpie ist man intrinsisch limitiert auf vorhandene Lasersysteme mit festen Wellenlängenbereichen und die Erschließung von weiteren Wellenlängen ist besonders im nahinfraroten und kurzwelligen sichtbaren bis UV Bereich interessant.

Insbesondere die Telekom Wellenlängen, d.h. der Bereich in dem Telekomunikationsfasern ihr Transmissionsminimum besitzen ist interessant für eine weitere Erschließung. Bisher kommen in diesen System Ga(In,As) Laser auf InP Substrat zum Einsatz. Dafür müssen aufwendige elektronische Koppler gebaut werden, die die Lasersysteme an vorhandene Siliziumtechnologie anbinden. Entsprechend ist es wünschenswert Lasersysteme direkt auf Silizium Substrat zu fertigen. Das in dieser Arbeit untersuchte Material Ga(N,As,P) bietet die Möglichkeit des pseudomorphen Wachstums auf Silizum. Der hier behandelte Forschungsgegenstand war die Charakterisierung der Band-Offsets der verschiedenen Materialien in einer Ga(N,As,P) Heterostruktur. Diese Band-Offsets sind sowohl für elektronische als auch optische Eigenschaften dieser Struktur wichtig. In dieser Arbeit wurde die relevanten Offsets zwischen Ga(N,As,P) und dessen Barrierenschichten GaP und (B,Ga)(As,P) mit zwei unterschiedlichen Methoden bestimmt. Die erste Methode, Photolumineszenzanregungsspektroskopie, ermöglicht die Bestimmung von höheren Zuständen im Quantenfilm. Eine eigens dafür erstellte Serie mit variierte Ga(N,As,P) Quantenfilm Dicke ermöglicht aus der Photolumineszenzanregungungsspektroskopie die Band Offsets aus den verspannungsbedingten Verschiebungen der Bänder zu bestimmen. Allerdings ist ein relativ hoher Aufwand an theoretischer Vorüberlegung nötig um die entsprechenden Übergangsenergien auf die Band Offsets zu bestimmen. Daher wurde der Offset außerdem direkt mit Röntgen Photoelektronenspektroskopie bestimmt. Dieser Ansatz liefert nicht nur die Offsets des optisch leuchtenden Materials, sondern außerdem auch die Offsets aller an der Struktur beteiligten Schichten. Ein Vergleich mit der Photolumineszenzanregungspektroskpie liefert hier ein abgerundetes Bild über die Bandanordnungen der Strukturen. Es konnte gezeigt werden, dass der Valenzbandoffset der Strukturen sehr gering ist. Diese Untersuchungen liefern damit einen Beitrag zur weiteren Optimierung der Strukturen, hin zu Lasersystemen auf Siliziumbasis.

Ein zweiter Ansatz die vorhandenen Wellenlängenregimes zu erweitern ist durch nichtlineare optische Effekte. Durch hohe Feldstärken, wie von heutigen Lasern bereitgestellt, findet in nicht zentrosymmetrischen Materialien eine Frequenzkonversion des Lichtes statt. Dadurch ist es möglich Wellenlängenbereiche zu erschließen für die kein Lasersystem existiert. Besonders im blauen und UV Bereich des Lichtspektrums werden diese Effekte verwendet. Der zweite Teil dieser Arbeit beschäftigt sich mit der Untersuchung solcher nichtlinearen optischen Effekte. Dies untergliedert sich in die Bestimmung der absoluten Effizienz der zweiten harmonischen Frequenzerzeugung im Material $KNbO_3$ und die Untersuchung neuartiger adamantanartiger Cluster zur Erzeugung von Weißlicht im sichtbaren und nahinfraroten Spektrum.